UNIVERSITAT DE BARCELONA

Dynamics of Isotopically Pure He Droplets Doped with Atomic Impurities

Antonio Jesús Leal Martín

Dynamics of Isotopically Pure He Droplets Doped with Atomic Impurities

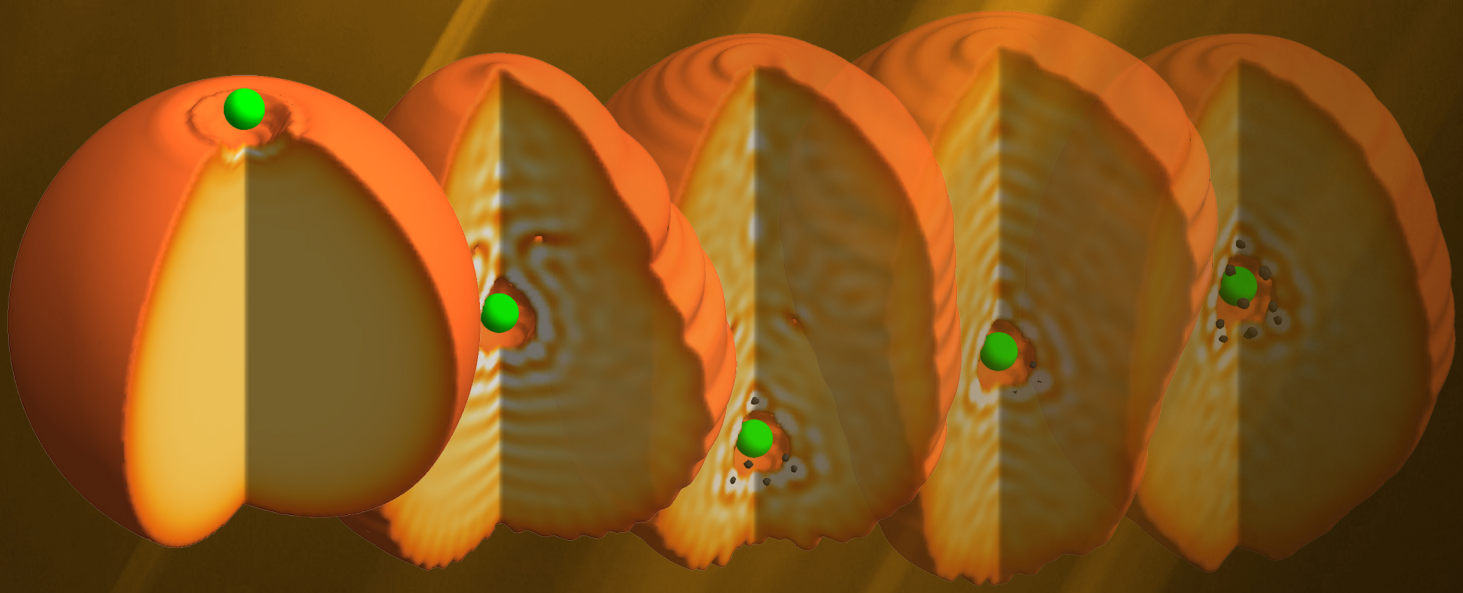

Antonio Jesús Leal Martín

UNIVERSITAT DE BARCELONA

Dynamics of isotopically pure He droplets doped with atomic impurities

by

Antonio Jesús Leal Martín

Directores: Martí Pi Pericay, Manuel Barranco Gómez

Tutor: Martí Pi Pericay

Thesis submitted for the Degree of Doctor of Philosophy under the Physics PhD program at the University of Barcelona.
April 2016

Tesis presentada para la obtención del grado de Doctor en el programa de doctorado de Física de la Universidad de Barcelona.
Abril 2016

Agradecimientos (Spanish)

Aunque es un ingrediente necesario, normalmente no basta con el trabajo personal para conseguir aquellos retos que uno se propone. Por eso no podía dejar pasar la oportunidad de dedicar al menos un pequeño espacio de esta tesis a agradecer su apoyo a todas aquellas personas que han estado a mi lado durante estos años y me han dado pequeños empujoncitos cuando más lo necesitaba.

En primer lugar a mis tutores, Manuel Barranco y Martí Pi, así como al resto de los coautores de los trabajos aquí presentados. Ya que sin vuestra ayuda este trabajo no hubiese sido posible. También quiero agradecer al resto de profesores y compañeros de la UB con los que he tenido trato, por el cariño y apoyo que me han transmitido.

A mis padres, Rafael y Antonia; mis hermanos Laura y Rafael y mis cuñados Lourdes y Fernando. Porque sin vosotros no sería la persona que soy hoy en día y porque siempre habéis estado ahí cuando lo he necesitado. Estar lejos de vosotros se hace complicado, pero siempre tendréis un hueco enorme en mi cabeza y mi corazón.

A mis amigos de Córdoba, los de siempre. Ya que pese a la distancia y los años sé que puedo seguir contando con vosotros de la misma manera que vosotros podéis contar conmigo. Os echo de menos.

A mis amigos de Barcelona. Porque habéis conseguido que estuviera en esta ciudad como si estuviese en mi propia casa y me habéis dado muy buenos momentos. Espero que siga siendo así por mucho tiempo.

Y por último a la persona más importante, mi pareja Clara. Porque has sido mi pilar fundamental en este último esprint final, porque siempre has confiado en mí y porque siempre has estado animándome para continuar adelante. Espero haber estado a la altura y que tú hayas recibido de mi parte el mismo apoyo. Te quiero.

A todos vosotros, ¡Muchísimas gracias!

Resumen (Spanish)

Contexto

El helio es el segundo elemento más ligero de la naturaleza y cuenta con una estructura atómica muy simple: dos electrones en torno a un núcleo con dos protones y dos neutrones —en el caso del ^{4}He— o en dos protones y un solo neutrón —para el ^{3}He—. Si se observan los diagramas de fase de ambos isótopos puede verse que cuentan además con la peculiaridad de permanecer en estado líquido en el cero absoluto de temperatura, gracias a una energía de punto cero lo suficientemente alta —debido a que es un elemento muy ligero y que cuenta con una estructura electrónica de capa cerrada que hace que la interacción entre átomos de He sea débil— como para evitar la solidificación. En estas condiciones —por debajo de 2.17 K para el ^{4}He y 2.7 mK para el ^{3}He— el helio es un superfluído, es decir, su viscosidad es prácticamente nula y puede fluir libremente, sin fricción.

Las nanogotas de helio han sido objeto de estudio de la física de *clusters* y de la química-física durante más de 20 años, ya que otra de las propiedades más útiles de las gotas de He es su habilidad para capturar átomos y moléculas con las que colisionan. Esto, junto la débil interacción del helio superfluído con su entorno, hace que hoy las gotas de helio se usen comúnmente como matrices a escala nanométrica para el estudio espectroscópico de moléculas y otros complejos. Las impurezas, también llamadas dopantes, una vez capturadas se hunden hacia el interior de la gota o, en algunos casos, quedan adheridas a la superficie de la misma. Por lo general, la mayoría de los átomos y moléculas en su estado fundamental experimentan una interacción atractiva débil con el He, por lo que suelen estar localizadas en el interior de las gotas, y muy débil para los átomos alcalinos que los hace situarse sobre la superficie de las mismas. Sin embargo,

cuando la impureza está en un estado excitado, su interacción con el He suele ser muy repulsiva. Esto conlleva que los dopantes excitados experimenten una aceleración hacia la superficie de la gota y que puedan ser eyectados.

Resultados

Esta tesis está compuesta de una colección de cinco de los artículos publicados desde 2013 a 2016, abarcados todos ellos en el campo de la física de bajas temperaturas y fluidos cuánticos. Cada uno de ellos constituye un paso adelante en la descripción teórica de los sistemas de helio en el marco de la teoría del funcional de la densidad.

Los dos primeros artículos están relacionados con estudios dinámicos de impurezas de Ba en nanogotas compuestas por 1000 átomos de helio. Se conoce experimentalmente, a partir del análisis del espectro de absorción de las impurezas, que los átomos de todos los elementos alcalinos y de todos los alcalinotérreos más pesados que el magnesio —como es el caso del bario— al ser capturados por las gotas de helio tienen un estado de equilibrio en la superficie de estas [1, 2].

En el primero de los artículos —sección 2.1— estudiamos dinámicamente la ionización de un átomo de Ba desde este punto de equilibrio haciendo uso de la teoría del funcional de la densidad. Los estudios espectroscópicos llevados a cabo por el grupo encabezado por el Prof. Drabbels (*EPFL, Lausana, Suiza*) indican que la impureza se hunde en el interior de la gota de helio tras la ionización, ya que el espectro de absorción del catión de Ba en gotas de helio coincide con el obtenido para la misma impureza en el helio líquido. Así lo corroboramos con nuestros estudios teóricos, en los que se observa cómo la impureza se desplaza hacia el interior de la gota tras ser ionizada. Durante este hundimiento, pudimos observar diferentes fenómenos como la formación de una estructura de alta densidad en torno a la impureza —conocida como *snowball*— o la nucleación de vórtices anulares cuantizados, de los cuales se estima su energía y velocidad.

El otro artículo dedicado al Ba^+ —sección 2.2— continúa el estudio del mismo sistema. En este caso tomamos como punto de partida la impureza ionizada en un punto de retroceso de la oscilación correspondiente al proceso de hundimiento y la excitamos a estados *6p*. Los resultados experimentales muestran un mecanismo eficiente de expulsión de la impureza de la gota, tanto en forma de catión Ba^+,

como en forma de *exciplex* Ba^+-He_n, siendo mayoritariamente $n = 1, 2$. Sin embargo, nuestras simulaciones no muestran dicha desolvatación, permaneciendo en el interior de la gota en todos los casos en los que excitamos a los estados *6p*. Además, debido a que para el Ba^+ el multiplete *5d* es menos energético que el *6p*, exploramos la posibilidad de que la impureza pudiese abandonar la gota tras una desexcitación $5d \leftarrow 6p$ así como una desexcitación al estado fundamental, pero en ninguno de los casos el resultado fue el deseado.

A pesar del desacuerdo entre teoría y experimento, del estudio se desprenden conocimientos útiles acerca de los procesos dinámicos de impurezas excitadas electrónicamente en gotas de helio.

El siguiente bloque está compuesto por dos artículos dedicados a las dinámicas de alcalinos en nanogotas de ^{4}He, en concreto rubidio y cesio, que comparten con el bario que su configuración de equilibrio en el estado fundamental está en la superficie de la gota.

En el primero de ellos —sección 3.1— estudiamos dinámicamente la eyección de átomos alcalinos desde la superficie de nanogotas de helio, excitando para ello a los estados $6s$ —para el rubidio— y $7s$ —para el cesio—. La relación entre la energía cinética y la energía de excitación de los átomos expulsados mediante este proceso coincide notablemente con la relación obtenida experimentalmente. Al analizar estos sistemas hemos encontrado, además, deformaciones locales de las nanogotas, así como tres tipos diferentes de ondas de densidad que se propagan a través de ellas a diferentes velocidades supersónicas.

Por otro lado, en el segundo artículo de este bloque —sección 3.2— hemos realizado para impurezas de Rb^+ y Cs^+ un estudio equivalente al que mostramos en la sección 2.1 para el Ba^+, analizando dinámicamente la evolución de estas impurezas al ser ionizadas en su posición de equilibrio sobre la superficie de una nanogota de helio. Observamos cómo el rubidio permanece en la superficie de la gota durante unos instantes tras ser ionizado para finalmente desplazarse al interior de la misma —nucleando vórtices en el proceso gracias a las perturbaciones de densidad en la superficie de la gota— mientras que el cesio escapa de la superficie llevándose consigo algunas decenas de átomos de helio. Asimismo pudimos comprobar que estas diferencias en el comportamiento de los cationes —entre sí y comparados con el Ba^+— se debían al tamaño finito de la gota, ya que para sistemas de mayor tamaño sí se reproducía el comportamiento observado en el

caso del bario. Por tanto, puede concluirse que al ser los potenciales Rb^+-He y Cs^+-He notablemente atractivos, se termina produciendo el hundimiento de las impurezas hacia el interior de las gotas si el tamaño de estas lo permite.

El bloque que cierra esta tesis está compuesto por un único artículo que trata las colisiones de impurezas heliofóbicas —en este caso átomos de cesio— contra nanogotas de helio. Hemos estudiado estas colisiones cuando se utilizan diferentes velocidades para la impureza, así como distintos parámetros de impacto —incluyendo las colisiones frontales con parámetro de impacto igual a cero—. Al modificar dichos parámetros hemos observado diferentes fenómenos que van desde la captura de la impureza por parte de la gota, permaneciendo en la superficie de la misma, hasta la "transparencia" de la gota para velocidades más altas —la impureza penetra en la gota traspasándola de un extremo a otro—. En el caso de las colisiones con parámetro de impacto distinto de cero, que depositan una cierta cantidad de momento angular en las gotas, mediante el estudio de las corrientes de densidad hemos podido observar que la gota no gira como un cuerpo rígido, apreciándose un esquema de corrientes que corresponde al de un superfluido.

Contents

Chapter 1

Introduction

Helium is the second lightest element and the second most abundant element in the universe. It is named for the Greek god of the sun, Helios, and it was first discovered by French astronomer Jules Janssen as an unknown yellow spectral line in sunlight during a solar eclipse in 1868.

Helium has a very simple atomic structure: two electrons around a nucleus formed of two protons and two neutrons (the case of ^{4}He) or two protons and a single neutron (for ^{3}He). Looking at the corresponding phase diagrams of both isotopes, it can be seen that they both have the unique property of maintaining the liquid phase down to $T = 0$ K, thanks to their zero point energy, which is large enough to avoid solidification (due to their low mass and the weak He-He interaction). The zero point energy is the lowest possible energy that a quantum mechanical physical system may have; it is the energy of its ground state. The existence of this energy is a prediction of Quantum Mechanics with no classical equivalent, and plays the role of a kinetic energy present even when there is no "motion" in the classical sense. The first liquefaction of helium was achieved in 1908, by Dutch physicist Heike Kamerlingh Onnes. Furthermore, under certain temperature conditions (below 2.17 K for ^{4}He and 2.7 mK for ^{3}He) helium becomes superfluid, that is, its viscosity is almost zero and it can flow without any friction. This remarkable feature was first discovered by Pyotr Kapitsa, John F. Allen, and Don Misener in 1937 [3, 4].

Helium nanodroplets have been extensively studied in cluster physics and physical chemistry for more than 20 years, as they have the ability to capture atoms and molecules they collide with. This property, along with the weak interaction of superfluid ^{4}He with atoms and molecules, makes them ideal nanometric

scale matrices for spectroscopic studies of molecules and other structures [5–11]. Once captured, the impurities (also known as dopants) may solvate inside the droplet or, in some cases, remain in a dimple on the surface.

The five papers presented in this thesis are organized in three different sections: Chapter 2 addresses the dynamic study of Ba^+ impurities at $^4He_{1000}$ nanodroplets by two publications. The first paper focuses on the dynamic study of Ba^+ upon ionization of Ba in a dimple on the surface of a droplet and the second paper studies the evolution of Ba^+ in the bulk portion of the droplet when it is excited to ^2P or ^2D states.

Chapter 3 presents the dynamic study of alkali impurities (Rb and Cs) at the same droplets. This chapter is also represented by two papers, where the first one addresses the ejection of these impurities from the surface of ^4He nanodroplets upon excitation to the $6s$ state (for rubidium) or $7s$ state (in the case of cesium), and the second paper studies the dynamic evolution of Rb^+ and Cs^+ after the corresponding neutral atom is ionized on the surface of a droplet.

Lastly, Chapter 4 presents an article that focuses on the capture of Cs atoms by $^4He_{1000}$ nanodroplets. We have studied this process by making cesium atoms collide with He droplets using different projectile velocities and impact parameters.

1.1 Theoretical study of helium systems

There are two main classes of methods commonly used to study these systems, depending on whether bare or effective atom-atom interactions are employed. For simplicity, we shall refer to the former as microscopic theories. They aim at solving, as accurately as possible, the manybody Schrödinger equation, employing the best helium-helium interaction available. Alternatively, some selected experimental properties of the homogeneous system can be used to construct an effective interaction, which afterwards is used in particular to describe inhomogeneous systems. As the effective interaction is He density-dependent, these type of methods fall into the general framework of density functional theories (DFT). Both kinds of methods are complementary.

The next subsection focuses on a brief presentation of DFT of ^4He, as all the publications presented in this thesis make a theoretical approach to the study of

^{4}He nanodroplets within that framework, trying to reproduce several experimental results.

1.1.1 Density Functional Theory

Density functional theory is based on rigorous formulation of nonrelativistic quantum many-body physics in which the energy of a system is expressed as a functional of the one-body density rather than the complete N-body wavefunction. The theoretical support of DFT is the Hohenberg-Kohn theorem [12], which establishes that the ground state energy of a many-body system is a unique functional of its density. Moreover, the Kohn-Sham (KS) method [13] allows to obtain from this functional not only the ground state energy but also the elementary excitation spectrum.

Nevertheless, this does not supply us with the functional itself, and it has to be written by taking into account both physical insight and phenomenological approaches. Several energy functionals for a system of interacting helium atoms have been developed over the years. The most commonly used functional for inhomogeneous ^{4}He settings is a finite-range functional known as "Orsay-Trento" presented in 1995 by F. Dalfovo *et al.* [14]. However, this functional can't deal with very structured helium configurations (high density peaks) that usually form around impurities (X) when the X-He potential is very attractive (*e.g.* for ionized impurities), which is our case. To solve this problem, we have used a modified version of this functional, presented by F. Ancilotto et al. [15] which introduces a "penalty" term to the functional. This term has the following form

$$E_p\left[\rho\right] = C \int \rho\left(\mathbf{r}\right) f\left[\rho\left(\mathbf{r}\right)\right] d\mathbf{r}, \tag{1.1}$$

where $f\left[\rho\left(\mathbf{r}\right)\right]$ is a "switch" function which becomes appreciably different from zero only when the density ρ is larger than a threshold value ρ_m. Such function can be written as

$$f\left[\rho\left(\mathbf{r}\right)\right] = 1 + \tanh\left\{\beta\left[\rho\left(\mathbf{r}\right) - \rho_m\right]\right\} \tag{1.2}$$

where C, β and ρ_m are DF parameters. $E_p\left[\rho\right]$ adds to the effective potential a term which acts as a repulsive barrier, forbidding extra pile-up of the density.

Once the density functional has been chosen, we can start the theoretical study of the system. In most cases, before starting the dynamics, we need to find the equilibrium configuration of the system that corresponds to the starting

point for dynamic calculations. This was achieved by performing a static DFT calculation where the impurity is treated as an external potential and the ground state energy of the system is written as a functional of the helium density (ρ) and the impurity-helium pair potential V_{X-He}:

$$E\left[\rho\right]=\int d\mathbf{r}\left\{\frac{\hbar^{2}}{2m_{He}}|\nabla\sqrt{\rho(\mathbf{r})}|^{2}+\varepsilon\left[\rho\left(\mathbf{r}\right)\right]+\rho\left(\mathbf{r}\right)V_{X-He}\left(|\mathbf{r}-\mathbf{r}_{X}|\right)\right\} \tag{1.3}$$

From this point forward, DFT can be easily extended to time-dependent DFT (TDDFT). In the dynamic calculations, the superfluid is described by a complex effective wavefunction $\Psi_{He}\left(\mathbf{r,t}\right)$ such that $\rho\left(\mathbf{r},t\right)=|\Psi_{He}\left(\mathbf{r,t}\right)|^{2}$ and the dopants, due to their large mass (compared to helium), are treated as classical particles. To obtain the dynamical evolution of the system (impurity @ $^{4}\mathrm{He}_{N}$), the following coupled 3D time-dependent equations have been solved

$$i\hbar\frac{\partial}{\partial t}\Psi_{He}=\left[-\frac{\hbar^{2}}{2m_{He}}\nabla^{2}+\frac{\delta\varepsilon_{He}}{\delta\rho\left(\mathbf{r}\right)}+V_{X-He}\left(|\mathbf{r}-\mathbf{r}_{X}|\right)\right]\Psi_{He}, \tag{1.4}$$

$$m_{X}\ddot{r}_{X}=-\nabla_{r_{X}}\left[\int d\mathbf{r}\rho\left(\rho\right)V_{X-He}\left(|\mathbf{r}-\mathbf{r}_{X}|\right)\right]. \tag{1.5}$$

The first equation is the TDDFT equation describing the helium nanodroplet and the second one is the classical evolution equation for the impurity motion. Usually, the problem is more involved as the X-He interaction depends on the electronic state of the impurity and it has to be taken into account [16].

Chapter 2

Ba^+ dynamics

2.1 Nucleation of quantized vortex rings in ^{4}He nanodroplets

Resumen (Spanish)

Pese a que la mayoría de los fenómenos asociados con la superfluidez ya han sido observados en sistemas de helio de tamaño finito, la percepción de la nucleación de vórtices cuantizados resulta esquiva. En este trabajo mostramos mediante simulaciones en el marco de la Teoría del Funcional de la Densidad que la solvatación de un ion de Ba creado por fotoionización del átomo de Ba neutro sobre la superficie de una nanogota de ^{4}He conduce a la nucleación de un vórtice anular cuantizado [17].

Este fenómeno de nucleación tiene lugar en una escala de unos 10 ps y se produce en torno al ecuador de una estructura de solvatación de tipo sólida que se genera alrededor del catión. Los resultados presentados en esta sección indican que los vórtices anulares cuantizados se crean de manera eficiente en gotas de helio por la solvatación de impurezas de Ba^+. De los cálculos se desprende que la nucleación del vórtice es un proceso local, siendo los grandes cambios estructurales en el líquido próximo a la impureza los responsables de la alta eficiencia del proceso.

En vista del caracter local de la nucleación de estos vórtices cuantizados, es altamente probable que el proceso de nucleación también se produzca en gotas de

helio debido a la captura de átomos o moléculas que cuenten con una interacción con el helio fuertemente atractiva.

Se puede concluir que, pese a que sean difíciles de detectar, la existencia de vórtices cuantizados en gotas dopadas puede ser un fenómeno más común de lo habitualmente supuesto.

THE JOURNAL OF CHEMICAL PHYSICS **140**, 131101 (2014)

Communication: Nucleation of quantized vortex rings in ^{4}He nanodroplets

David Mateo,[1] Antonio Leal,[1] Alberto Hernando,[2] Manuel Barranco,[1] Martí Pi,[1] Fausto Cargnoni,[3] Massimo Mella,[4] Xiaohang Zhang,[5] and Marcel Drabbels[5]
[1]*Departament ECM, Facultat de Física, and IN^{2}UB, Universitat de Barcelona, Diagonal 645, 08028 Barcelona, Spain*
[2]*Laboratory of Theoretical Physical Chemistry, Institut des Sciences et Ingénierie Chimiques, Swiss Federal Institute of Technology Lausanne (EPFL), CH-1015 Lausanne, Switzerland*
[3]*Istituto di Scienze e Tecnologie Molecolari (ISTM), Consiglio Nazionale delle Ricerche, via Golgi 19, 20133 Milano, Italy*
[4]*Dipartimento di Scienza ed Alta Tecnologia, Università degli Studi dell'Insubria, via Valleggio 11, 22100 Como, Italy*
[5]*Laboratoire de Chimie Physique Moléculaire, Swiss Federal Institute of Technology Lausanne (EPFL), CH-1015 Lausanne, Switzerland*

(Received 27 February 2014; accepted 21 March 2014; published online 3 April 2014)

Whereas most of the phenomena associated with superfluidity have been observed in finite-size helium systems, the nucleation of quantized vortices has proven elusive. Here we show using time-dependent density functional simulations that the solvation of a Ba^+ ion created by photoionization of neutral Ba at the surface of a ^{4}He nanodroplet leads to the nucleation of a quantized ring vortex. The vortex is nucleated on a 10 ps timescale at the equator of a solid-like solvation structure that forms around the Ba^+ ion. The process is expected to be quite general and very efficient under standard experimental conditions. © *2014 AIP Publishing LLC*. [http://dx.doi.org/10.1063/1.4870245]

Helium clusters are paradigms of finite-size quantum systems.[1] These nanodroplets attain a temperature of 0.37 K,[2,3] clearly below the superfluid transition temperature of liquid ^{4}He, $T_\lambda = 2.17$ K. Quantum Monte Carlo calculations have revealed that even very small droplets containing less than 100 helium atoms display features pertaining to the superfluid state of bulk liquid helium.[4–6] Although such small systems are expected to be superfluid, it is not obvious whether phenomena generally associated with superfluidity in bulk helium will be manifested in these nanosystems. First indications of a vanishing viscocity were provided by spectroscopic experiments on helium droplets doped with carbonyl sulfide (OCS). The IR spectrum of OCS revealed a well resolved rovibrational structure, which has been taken as evidence that the OCS molecule can freely rotate inside the ^{4}He droplet.[7] The minimum number of ^{4}He atoms required to produce the effect was about 60, in good agreement with the calculations.[4] However, recent experiments indicate that the system is more complex than initially anticipated as the temporal evolution of rotational wave packets cannot be explained with the free rotation of the embedded molecule.[8] Another subtle manifestation of superfluidity is the frictionless displacement of impurities inside helium if they move at velocities below the so-called Landau velocity. Recent experiments in which impurities were accelerated out of helium droplets by means of electronic excitation have revealed that a critical Landau velocity exists even for droplets consisting of less than one thousand helium atoms.[9,10]

In the quest for manifestations of superfluidity in nanoscale helium droplets, the nucleation of quantized vortices has proven elusive for years. Only recently indications have been found for the presence of vortices in large helium droplets.[11] These droplets consisting of $10^7 - 10^{10}$ atoms were produced by fragmentation of a cryogenic fluid. Such large droplets are true mesoscopic pieces of superfluid helium, having radii in the range of 50 − 500 nm. It is thus somewhat expected that they may host vortex lines, either preexisting in the fluid or created in the fragmentation process. The main question is whether vortices may also be nucleated in much smaller droplets consisting of only a few hundreds or thousands of helium atoms. These droplets are expected to carry enough energy and angular momentum to create a vortex which is especially robust due to the lack of decay channels that conserve both energy and angular momentum.[12] Moreover, in experiments with doped droplets, the pickup of impurities might lead to vortex nucleation. Once nucleated, they are stabilized by pinning to the impurity inside the droplet.[13] One limitation of all these theoretical studies is that they take for granted that vortices have been nucleated.

Vortex ring nucleation around electron bubbles in superfluid helium has recently been addressed using density functional (DF) simulations of different complexity.[14–16] The nucleation of vortices by cations or neutral impurities, which have very different helium solvation structures than electrons, has not been addressed by realistic methods, only by approximate methods that model these impurities as repulsive rigid spheres.[17] A full dynamical description of the process for these systems is thus still lacking.[18,19] In the present work, we show using a time-dependent DF approach that the dynamics following the photoionization of neutral Ba atoms located on the surface of helium nanodroplets leads to vortex nucleation.

At variance with other possible methods for vortex nucleation, the current process is initiated using a well-defined, experimentally reproducible condition, i.e., the equilibrium configuration of Ba atom located at a surface dimple. Hence,

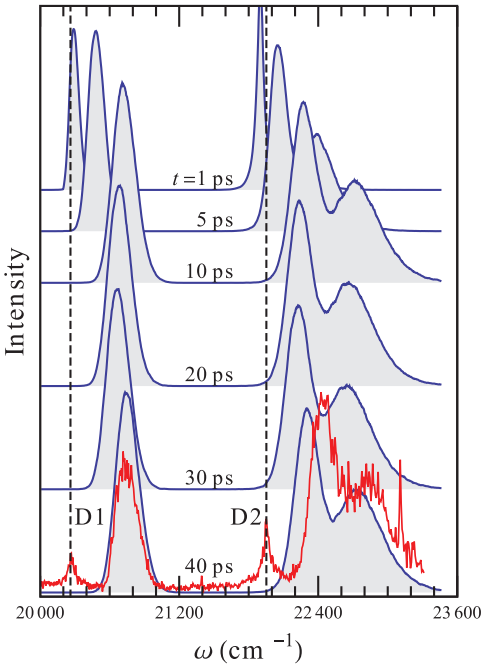

FIG. 1. Time-resolved absorption spectrum of Ba^+ in a $^4He_{1000}$ droplet. The experimental spectrum for helium droplets consisting on average of 2700 atoms is shown in red. The vertical lines indicate the D1 and D2 transitions of the free Ba^+ cation.

vortex nucleation is expected to be highly efficient in these types of experiments.

Recent experiments on the solvation dynamics of Ba^+ created at the surface of small helium nanodroplets serve as reference for the present calculations.[20] The 6p ← 6s transition of Ba^+ shown in Fig. 1 was found to coincide with that of Ba^+ in bulk superfluid helium, indicating that the Ba^+ ion becomes fully solvated by the helium on the nanosecond timescale of the experiment.

We describe the solvation process of the Ba^+ ion by a three dimensional time-dependent DF approach in which the superfluid is described by a complex effective wavefunction $\Psi_{He}(\mathbf{r}, t)$ such that $\rho(\mathbf{r}, t) = |\Psi_{He}(\mathbf{r}, t)|^2$ and the Ba^+ impurity, due to its large mass, is treated as a classical particle with position $\mathbf{r}_{Ba^+}(t)$.[10] To obtain the dynamical evolution of the $Ba^+@^4He_{1000}$ system, the following coupled 3D time-dependent equations have been solved:

$$i\hbar\frac{\partial}{\partial t}\Psi_{He} = \left[-\frac{\hbar^2}{2m_{He}}\nabla^2 + \frac{\delta\mathcal{E}_{He}}{\delta\rho(\mathbf{r})} + V_{6s}^+(\mathbf{r}-\mathbf{r}_{Ba^+})\right]\Psi_{He} \quad (1)$$

$$m_{Ba^+}\ddot{\mathbf{r}}_{Ba^+} = -\nabla_{\mathbf{r}_{Ba^+}}\left[\int d\mathbf{r}\rho(\mathbf{r})V_{6s}^+(\mathbf{r}-\mathbf{r}_{Ba^+})\right],$$

where $\mathcal{E}_{He}$ is the DF potential energy density per unit volume and $V_{6s}^+(\mathbf{r}-\mathbf{r}_{Ba^+})$ is the ground state Ba^+-He pair potential. To avoid reflections at the boundaries of the calculation cell, an absorption potential has been added to the Hamiltonian.[21] The DF used in the present work[22] is a modified version of

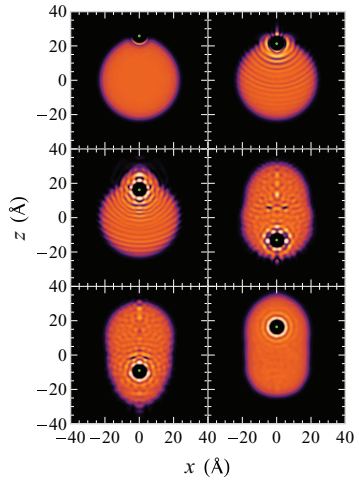

FIG. 2. Snapshots of the temporal evolution of the $Ba@^+He_{1000}$ system after photoionization of the neutral Ba atom located at the droplet surface. Panels 1 to 6 correspond to the helium densities at times t = 0, 8, 14, 47, 60, and 220 ps. (Multimedia view) [URL: http://dx.doi.org/10.1063/1.4870245.1]

the Orsay-Trento DF[23] able to handle very structured helium configurations as those expected to appear around very attractive impurities such as cations. This functional has been found to accurately reproduce the helium configurations calculated by Quantum Monte Carlo methods.[24,25] Details of how the above equations have been solved can be found in Refs. 10, 21, and 26. The modelling of the solvation process critically depends on the quality of the ingredients entering the calculation. In the absence of accurate He-Ba^+ pair potentials, these have been computed in this study at the CCSD(T) level of theory. The 46 core electrons of Ba^+ are described by the Def2 pseudopotential,[27] while for the outermost 9 electrons the QZVP quadruple-z set is used.[28] The He atom has been assigned the aug-cc-pV5Z basis,[29] and a 3s3p2d set of bond functions has been located at midway between the two nuclei.[30]

The initial conditions for solving the equations correspond to those at the time of ionization, i.e., the equilibrium configuration of the neutral $Ba@4He_{1000}$ complex. DF calculations find this configuration to have the Ba atom residing in a dimple at the surface of the droplet,[31] in agreement with experiments.[32,33] Snapshots of the dynamical evolution of the $Ba^+@^4He_{1000}$ system are presented in Fig. 2 (Multimedia view). During the initial phase of the solvation process, supersonic density waves are emitted into the droplet. Similar density waves have been observed when alkali atoms located at the surface of the droplets are excited and have been analyzed in detail.[34] Due to the attractive interaction of the Ba^+ with the helium, the ion moves towards the center of the droplet. After approximately 8 ps, the barium ion is fully surrounded by the helium and a few picoseconds later a solid-like solvation layer with localized helium atoms dubbed "snowball" forms. As the Ba^+ is accelerated further towards the center of the droplet, it interacts with the helium density waves reflected from the droplet surface, leading to fast

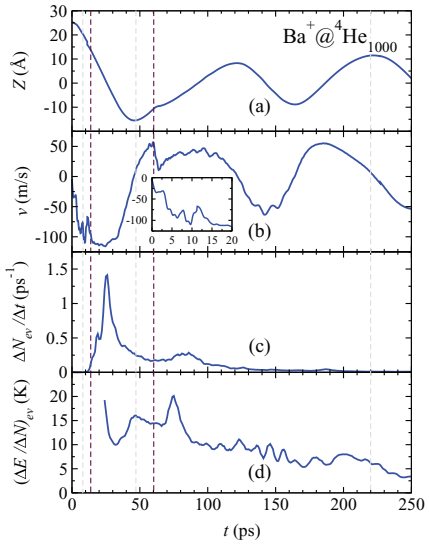

FIG. 3. Position (a) and velocity (b) of the Ba^+ ion with respect to the helium droplet center-of-mass. The inset shows the velocity of Ba^+ during the first 20 ps. Number of evaporated helium atoms per unit time (ps^{-1}) (c) and energy (K) removed from the helium droplet per evaporated helium atom (d). The vertical dashed lines indicate the times corresponding to the snapshots 2 to 6 shown in Fig. 2, where the dark lines correspond to times just after vortex nucleation and just before vortex annihilation.

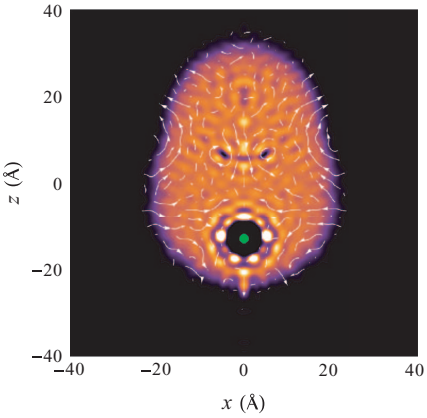

FIG. 4. Snapshot of the helium density at 45 ps showing the snowball and a quantized vortex ring. The circulation lines are represented in white.

structural changes in the solvation structure, see Fig. 2 (Multimedia view). After passing the center of the droplet at $t \approx 20$ ps, the ion is decelerated and subsequently reflected at the droplet surface at $t \approx 40$ ps. Figure 3 shows the motion of the Ba^+ ion with respect of the $^4He_{1000}$ center of mass in terms of position and velocity as a function of time. The Ba^+ continues oscillating back and forth in the droplet with a period of ~100 ps up to the end of the simulation, i.e., 350 ps. During this period, the helium density waves damp out and the fluctuating solvation structure surrounding the ion becomes homogenous, see Fig. 2 (Multimedia view), in agreement with the calculated equilibrium structure of the $Ba^+@^4He_{1000}$ system. After the first oscillation, during which the velocity of the Ba^+ changes erratically due to interaction with the helium density waves, the velocity of the Ba^+ remains at all times below the critical Landau velocity, which has been found to be 96 m/s for the DF used in this work.[22] Consequently, the Ba^+ is expected to keep oscillating for much longer times than the 350 ps simulation, as translational energy can only be removed by the interaction with droplet surface oscillations and deformations.

The solvation of the ion is reflected in the $6p \leftarrow 6s$ absorption spectrum of Ba^+. The time resolved spectrum has been obtained by the DF sampling method described in Ref. 35. The 6p excited state He-Ba^+ pair potentials required for the calculations have been computed using the CI method including single and double excitations (CISD), and using the same pseudopotential and basis sets adopted for the ground state. The spectrum shown in Fig. 1 reveals an obvious evolution with time that could be quantitatively checked by time-resolved absorption experiments. At $t = 1$ ps, the spectrum is red-shifted with respect to the corresponding gas phase transitions, reflecting the non-equilibrium helium density distribution surrounding the Ba^+ at the start of the evolution. During the first 10 ps, as the helium rearranges to solvate the Ba^+ ion, the spectrum shifts towards the blue, and a good agreement with the experimental spectrum is observed. From 10 ps onwards, the spectrum displays a small variation with time reflecting the change in the helium environment as the Ba^+ traverses the droplet.

The solvation of the Ba^+ releases energy into the helium droplet as a result of which helium atoms desorb from the droplet during the evolution of the system. By monitoring the number of atoms leaving the simulation box we find that most of the atoms desorb from the droplet during the first 100 ps at well-defined times, see Fig. 3. The atoms desorbing after 20 ps result from the formation of the solvation layer around the Ba^+ and leave the droplet in the backward direction, defined as the direction opposite to the initial acceleration of the Ba^+. The peak at 80 ps is related to the reflection of the Ba^+ at the droplet surface which leads to a large deformation of the droplet and the desorption of helium atoms in the forward direction. Since the desorption of these atoms is governed by dynamical processes, the amount of energy removed from the droplet by an atom, ≈20 K, is substantially larger than its binding energy of ≈6 K. At longer times the energy appears to be dissipated by an evaporative-like process.

Besides the dynamic formation of the Ba^+ snowball and the time-resolved absorption spectrum of this cation, the most interesting outcome of the calculations is the formation of a vortex ring at the equator of the Ba^+ solvation structure after about 13 ps, see Fig. 2 (Multimedia view). This vortex ring slips around the ion and eventually detaches from it at 24 ps. The cross section of this vortex ring is readily recognized as the two dark spots behind the ion bubble in the helium density at $t = 45$ ps presented in Fig. 4. Superimposed on the helium density displayed in this figures are the circulation lines. These clearly reveal a circular flow field around the vortex. Calculation of the circulation around the core yields

a value of unity in units of h/m_{He}, indicating that this vortex ring is quantized. The nucleation of the vortex is reflected in the translational motion of the Ba^+. As can be seen in Fig. 3, the nucleation of the vortex temporarily decelerates the ion bubble, that then accelerates anew when the vortex detaches. Using this velocity change, the vortex energy can be estimated to be on the order of 60 K. This value can be compared to the vortex energy, E_{ring}, calculated using the expression:[19,36]

$$E_{ring} = \frac{2\pi^2\hbar^2}{m_{He}}\rho_0 R\left(\ln\frac{8R}{a} - 1.615\right), \quad (2)$$

with a the vortex core size, R the vortex radius and ρ_0 the helium number density at large distance. Taking the values for the present system, $a = 0.7$ Å, $R = 4.2$ Å, and $\rho_0 = 0.0218\,\text{Å}^{-3}$ corresponding to the number density of a pure helium droplet, we obtain an energy of ∼46 K. This compares fairly well with the value determined from the velocity change of the Ba^+, considering that Eq. (2) is only valid in the limit of $R \gg a$. After detachment, the vortex ring moves with a nearly constant speed of 50 m/s as determined from the displacement of the vortex core in the time interval $t = 30 - 50$ ps. This value is slightly less than the self-induced speed of $v_{ring} = 61$ m/s for a vortex with the aforementioned characteristics, as calculated from:[19,36]

$$v_{ring} = \frac{\hbar}{2\,m_{He}R}\left(\ln\frac{8R}{a} - 0.615\right). \quad (3)$$

The vortex ring is eventually annihilated at 61 ps when it collides with the Ba^+ that has been reflected at the droplet surface. The annihilation of the vortex ring leads to a strong reduction of the Ba^+ speed, as is clearly visible in Fig. 3. At the same time helium density waves emerge from the solvation structure surrounding the Ba^+ ion. These waves carry away most of the energy released by the annihilation of the vortex.

The present results indicate that quantized vortex rings are efficiently created in helium droplets by the solvation of a Ba^+ ion. From the calculations it becomes clear that vortex nucleation is a local process, see Fig. 2 (Multimedia view). Most likely the large structural changes in the liquid close to the attractive impurity are responsible for the high efficiency of the process. We therefore expect vortex nucleation to be largely independent of droplet size and impurity. As alkali atoms, like the heavy alkaline-earth atoms, are located at the droplet surface and have strongly attractive ion-helium interaction potentials they should behave very similar to barium. In particular, Na and Rb located at the surface of ^{4}He droplets are known to become solvated after ionization.[37,38] In view of the local character of the process, it is quite likely that ring vortices are also nucleated in helium droplets by the pickup of atoms or molecules having strong attractive interactions with the helium. We therefore conclude that, irrespective of their detection, the formation of vortex rings in doped droplets could be a much more common phenomenon than expected.

This work has been performed under Grant Nos. FIS2011-28617-C02-01 from DGI, Spain (FEDER), 2009SGR1289 from Generalitat de Catalunya, and 200021-146598 from the Swiss National Science Foundation. A.L. has been supported by the ME (Spain) FPI program, Grant No. BES-2012-057439.

[1]J. P. Toennies and A. F. Vilesov, Angew. Chem., Int. Ed. **43**, 2622 (2004).
[2]D. M. Brink and S. Stringari, Z. Phys. D **15**, 257 (1990).
[3]M. Hartmann, R. E. Miller, J. P. Toennies, and A. Vilesov, Phys. Rev. Lett. **75**, 1566 (1995).
[4]P. Sindzingre, M. L. Klein, and D. M. Ceperley, Phys. Rev. Lett. **63**, 1601 (1989).
[5]M. V. Rama Krishna and K. B. Whaley, Phys. Rev. Lett. **64**, 1126 (1990).
[6]S. A. Chin and E. Krotscheck, Phys. Rev. B **45**, 852 (1992).
[7]S. Grebenev, J. P. Toennies, and A. Vilesov, Science **279**, 2083 (1998).
[8]D. Pentlehner, J. H. Nielsen, A. Slenczka, K. Molmer, and H. Stapelfeldt, Phys. Rev. Lett. **110**, 093002 (2013).
[9]N. B. Brauer, S. Smolarek, E. Loginov, D. Mateo, A. Hernando, M. Pi, M. Barranco, W. J. Buma, and M. Drabbels, Phys. Rev. Lett. **111**, 153002 (2013).
[10]D. Mateo, A. Hernando, M. Barranco, E. Loginov, M. Drabbels, and M. Pi, Phys. Chem. Chem. Phys. **15**, 18388 (2013).
[11]L. F. Gomez, E. Loginov, and A. Vilesov, Phys. Rev. Lett. **108**, 155302 (2012).
[12]K. K. Lehmann and R. Schmied, Phys. Rev. B **68**, 224520 (2003).
[13]F. Dalfovo, R. Mayol, M. Pi, and M. Barranco, Phys. Rev. Lett. **85**, 1028 (2000).
[14]D. Jin and H. J. Maris, J. Low Temp. Phys. **158**, 317 (2010).
[15]D. F. Jin and W. Guo, Phys. Rev. B: Condens. Matter **82**, 094524 (2010).
[16]F. Ancilotto, M. Barranco, and M. Pi, Phys. Rev. B: Condens. Matter **82**, 014517 (2010).
[17]N. G. Berloff, Phys. Lett. A **277**, 240 (2000).
[18]C. M. Muirhead, W. F. Vinen, and R. J. Donnelly, Philos. Trans. R. Soc. London, Ser. A **311**, 433 (1984).
[19]R. J. Donnelly, *Quantized Vortices in Helium II*, Cambridge Studies in Low Temperature Physics (Cambridge University Press, Cambridge, 1991), Vol. 3.
[20]X. Zhang and M. Drabbels, J. Chem. Phys. **137**, 051102 (2012).
[21]D. Mateo, D. Jin, M. Barranco, and M. Pi, J. Chem. Phys. **134**, 044507 (2011).
[22]F. Ancilotto, M. Barranco, F. Caupin, R. Mayol, and M. Pi, Phys. Rev. B **72**, 214522 (2005).
[23]F. Dalfovo, A. Lastri, L. Pricaupenko, S. Stringari, and J. Treiner, Phys. Rev. B **52**, 1193 (1995).
[24]F. Ancilotto, M. Pi, R. Mayol, M. Barranco, and K. K. Lehmann, J. Phys. Chem. A **111**, 12695 (2007).
[25]S. L. Fiedler, D. Mateo, T. Aleksanyan, and J. Eloranta, Phys. Rev. B **86**, 144522 (2012).
[26]A. Hernando, M. Barranco, R. Mayol, M. Pi, and M. Krośnicki, Phys. Rev. B **77**, 024513 (2008).
[27]M. Kaupp, P. V. Schleyer, H. Stoll, and H. Preuss, J. Chem. Phys. **94**, 1360 (1991).
[28]F. Weigend and A. Baldes, J. Chem. Phys. **133**, 174102 (2010).
[29]D. E. Woon and T. H. Dunning, Jr., J. Chem. Phys. **100**, 2975 (1994).
[30]F.-M. Tao, Z. Li, and Y.-K. Pan, Chem. Phys. Lett. **255**, 179 (1996).
[31]A. Hernando, R. Mayol, M. Pi, M. Barranco, F. Ancilotto, O. Bünermann, and F. Stienkemeier, J. Phys. Chem. A **111**, 7303 (2007).
[32]F. Stienkemeier, F. Meier, and H. O. Lutz, Eur. Phys. J. D **9**, 313 (1999).
[33]E. Loginov and M. Drabbels, J. Chem. Phys. **136**, 154302 (2012).
[34]A. Hernando, M. Barranco, M. Pi, E. Loginov, M. Langlet, and M. Drabbels, Phys. Chem. Chem. Phys. **14**, 3996 (2012).
[35]D. Mateo, A. Hernando, M. Barranco, R. Mayol, and M. Pi, Phys. Rev. B **83**, 174505 (2011).
[36]P. H. Roberts and J. Grant, J. Phys. A **4**, 55 (1971).
[37]E. Loginov and M. Drabbels, Phys. Rev. Lett. **106**, 083401 (2011).
[38]M. Theisen, F. Lackner, and W. E. Ernst, Phys. Chem. Chem. Phys. **12**, 14861 (2010).

2.2 Dynamics of photoexcited Ba^+ cations in ^{4}He nanodroplets

Resumen (Spanish)

Presentamos un estudio conjunto, experimental y teórico, sobre la emisión de cationes de Ba en nanogotas de ^{4}He excitados a través de la transición 6p $\leftarrow$ 6s. Los experimentos revelan un eficiente mecanismo de emisión que produce principalmente cationes de Ba y exciplexes Ba^+He_n con varios átomos de helio, siendo mayoritariamente $n = 1$ y 2. Las distribuciones de velocidad de los cationes quedan bien descritas por la distribución de Maxwell-Boltzman con temperaturas entre 60 y 178 K dependiendo de la frecuencia de excitación y del tamaño del exciplex.

Estos resultados han sido analizados mediante cálculos basados en una descripción de la gota de He en el marco de la Teoría del Funcional de la Densidad Dependiente del Tiempo. Mientras que la formación dinámica de exciplexes queda descrita con precisión a través de la TDDFT, aportando una útil visión microscópica de la estructura local de He en torno al catión excitado, la eyección de la impureza no se ha producido en las simulaciones.

A pesar del desacuerdo entre teoría y experimento, en este estudio se proporcionan útiles conocimientos acerca de los complejos procesos dinámicos que se producen tras la excitación electrónica de impurezas en nanogotas de ^{4}He.

THE JOURNAL OF CHEMICAL PHYSICS **144**, 094302 (2016)

Dynamics of photoexcited Ba^+ cations in ^4He nanodroplets

Antonio Leal,[1] Xiaohang Zhang,[2] Manuel Barranco,[1,3] Fausto Cargnoni,[4] Alberto Hernando,[5] David Mateo,[6] Massimo Mella,[7] Marcel Drabbels,[2] and Martí Pi[1]
[1]*Departament ECM, Facultat de Física, and IN²UB, Universitat de Barcelona, Diagonal 645, 08028 Barcelona, Spain*
[2]*Laboratoire de Chimie Physique Moléculaire, Swiss Federal Institute of Technology Lausanne (EPFL), CH-1015 Lausanne, Switzerland*
[3]*Laboratoire des Collisions, Agrégats, Réactivité, IRSAMC, UMR 5589, CNRS et Université Paul Sabatier-Toulouse 3, 118 route de Narbonne, F-31062 Toulouse Cedex 09, France*
[4]*Istituto di Scienze e Tecnologie Molecolari (ISTM), Consiglio Nazionale delle Ricerche, via Golgi 19, 20133 Milano, Italy*
[5]*Social Thermodynamics Applied Research (SThAR), EPFL Innovation Park, Bâtiment C, CH-1015 Lausanne, Switzerland*
[6]*Department of Chemistry and Biochemistry, California State University at Northridge, Northridge, California 91330, USA*
[7]*Dipartimento di Scienza ed Alta Tecnologia, Università degli Studi dell'Insubria, via Valleggio 11, 22100 Como, Italy*

(Received 18 December 2015; accepted 26 January 2016; published online 4 March 2016)

We present a joint experimental and theoretical study on the desolvation of Ba^+ cations in ^4He nanodroplets excited via the 6p ← 6s transition. The experiments reveal an efficient desolvation process yielding mainly bare Ba^+ cations and Ba^+He_n exciplexes with $n = 1$ and 2. The speed distributions of the ions are well described by Maxwell-Boltzmann distributions with temperatures ranging from 60 to 178 K depending on the excitation frequency and Ba^+ He_n exciplex size. These results have been analyzed by calculations based on a time-dependent density functional description for the helium droplet combined with classical dynamics for the Ba^+. In agreement with experiment, the calculations reveal the dynamical formation of exciplexes following excitation of the Ba^+ cation. In contrast to experimental observation, the calculations do not reveal desolvation of excited Ba^+ cations or exciplexes, even when relaxation pathways to lower lying states are included. © *2016 AIP Publishing LLC.* [http://dx.doi.org/10.1063/1.4942850]

I. INTRODUCTION

Ever since the first ion drift experiments in liquid helium by Williams in 1957,[1] ions have played a crucial role in elucidating the properties of superfluid ^4He. One of the highlights is undoubtedly the experimental determination of the critical Landau velocity.[2] The helium solvation structure surrounding ions depends strongly on their charge. Due to the Pauli repulsion an electron is located in a region void of helium with a radius of typically 17 Å,[3,4] giving this structure a large effective hydrodynamic mass.[5] The structure around positive ions is very different as electrostriction leads to the formation of high density helium shells ("snowballs") around cations.[6,7] Details about these solvation structures can be inferred from ion mobility experiments.[8] In this context, alkali earth cations are of special interest since their structure is determined by the balance between electrostriction due to the charge and the Pauli repulsion experienced by the unpaired electron. Additional insight in the solvation structure can be obtained from the spectroscopic investigation of the solvated species, as spectra are strongly affected by the interaction of the solute with helium. While most experiments have focussed on the neutral species,[9] also spectra of cations have been recorded, most notably Ba^+.[10] The excitation spectrum corresponding to the 6p ← 6s transition of Ba^+ is found to be substantially broadened and blue-shifted with respect to the gas phase. In agreement with the ion mobility solvation structure determination, the characteristics of the spectrum could be largely reproduced by a bubble model.[11]

Compared to bulk helium, the solvation of atoms and molecules is much less challenging when using helium nanodroplets.[12] As a result, most spectroscopic studies on solutes in helium are performed using helium droplets, see, for example, Refs. 13–15. From these experiments, the temperature of the ^4He droplets could be established to be 0.38 K.[16] The electronic and vibrational spectra of glyoxal and OCS, respectively, provided strong indications that these finite size helium droplets are superfluid at this temperature.[17,18] Recent drift experiments in helium droplets where neutral atoms and molecules have been accelerated out of droplets by electronic excitation have revealed the existence of a critical Landau velocity in these droplets.[19]

In contrast to the large body of literature on the spectroscopy of neutral species in helium droplets, that involving ions is rather limited due to the technical challenges associated with the production of ion containing droplets.[20–22] Initial spectroscopic studies on ions in helium droplets have revealed that the effect of the helium on the spectra of charged species is similar as for neutral species. Similar to neutrals, electronic spectra are characterized by sharp

zero-phonon lines and broad phonon wings,[23] while vibrational spectra are characterized by narrow transitions and small helium induced matrix shifts.[24–26] Whereas the spectroscopy for neutral and charged species is very similar, their dynamics appear to be different. Vibrational excitation of a neutral is followed by a fast transfer of the photon energy from the molecule to the helium leading to the shrinking of the helium droplet by evaporation of atoms from its surface.[27] In contrast, vibrational excitation of ions in helium droplets is found to lead to a nonthermal desolvation process in which the ions are ejected from the droplets.[24,28,29] To disentangle the role of vibrational and electronic excitation, the desolvation of excited of Ba^+ cations embedded in helium droplets has recently been investigated.[30] Here, in an attempt to elucidate the desolvation process of ions, we report more elaborate experiments on this system accompanied with a theoretical modeling of the dynamics. The calculations are based on a time-dependent density functional description of the helium combined with classical dynamics for the excited Ba^+ cation. Helium density functional calculations have been very successful in the past in describing static properties of doped helium droplets, see, e.g., Ref. 31 and references therein. Recently the time-dependent version has been successfully applied to describe various dynamical processes, like the capture of atoms by helium droplets,[32] the solvation of ions,[33,34] and the desorption of atoms from helium droplets.[35–37] Here we apply this method to investigate the dynamics of excited Ba^+ ions in helium nanodroplets.

II. EXPERIMENTAL

A. Setup

Details of the experiment and the experimental setup have been reported before.[30,38,39] Helium droplets are formed by expanding He gas at stagnation pressure of 30 bars into vacuum through a cryogenically cooled 5 μm orifice. The size distribution of these droplets can be systematically varied by changing the source temperature.[40] The helium droplets on average pick up less than one Ba atom as they pass through a heated oven containing barium dendritic crust. Via a differential pumping stage the doped droplets enter a velocity map imaging setup where the droplet beam is crossed at right angles by two counter-propagating laser beams. The barium-doped helium droplets are ionized by one-photon absorption of a 42 283 cm^{-1} photon from a frequency-doubled Nd:YAG pumped dye laser. After a time delay of 185 ns, the barium ions are excited via the 6p ← 6s transition by visible radiation in the wavelength range of 430-500 nm provided by another Nd:YAG pumped dye laser. The ions are accelerated towards a position sensitive detector consisting of a set of microchannel plates and a phosphor screen. A high-resolution CCD camera takes snapshots of the phosphor screen at each laser shot. The individual images are analyzed online and the centroids of the ion impacts are determined. The velocity distributions of the ions are determined by performing an inverse Abel transform on the images constructed from the accumulated centroids. Ion images can be recorded at a specific mass or masses by gating the front of the detector at the arrival time of the ions of interest. By feeding the electrical signal from the phosphor screen into a multichannel scaler, time-of-flight mass spectra can be recorded.

B. Results

As previously reported, upon ionization of the Ba atoms the created Ba^+ ions become solvated by the helium on a picosecond time scale.[30,34] Excitation of the solvated ions via the 6p ← 6s transitions subsequently leads their desolvation. The corresponding spectrum, recorded by monitoring the yield of desolvated ions as a function of excitation frequency can be found in Fig. 1 of Ref. 30. The D1 and D2 lines, corresponding to the $^2P_{1/2} \leftarrow {}^2S_{1/2}$ and $^2P_{3/2} \leftarrow {}^2S_{1/2}$ transition, respectively, are broadened and blue-shifted by approximately 500 cm^{-1} compared to the gas phase. The D2 line shows an additional splitting of ~400 cm^{-1}. The product distribution of the desolvated ions has been determined by time-of-flight mass spectrometry at three excitation frequencies, 20 714, 22 425, and 22 845 cm^{-1}, corresponding to the D1 and the two D2 absorption maxima, respectively. Analysis of the mass spectra reveals that approximately half of all ions are fully desolvated, while the other half carries along one or more helium atoms, see Fig. 1 which reports the relative Ba^+He_n product yield. The Ba^+He_n product distributions depend weakly on the spin-orbit state and are found to extend up to $n = 25$. Excitation via the D1 transition yields the smallest amount of bare Ba^+ ions and a nearly similar amount of Ba^+He. Excitation of the D2 transition at low frequency yields the maximum amount of bare Ba^+ ions. Interestingly, excitation at the high frequency part of the D2 transitions yields a slightly different product distribution with a relatively large amount of Ba^+He_n exciplexes with $4 \le n \le 8$.

In order to gain insight into the desolvation mechanism of the excited ions their speed distributions have been determined by velocity map imaging. A typical image is shown in the inset of Fig. 2. It has been recorded following excitation via the D1 transition of Ba^+ ions solvated in droplets consisting on average of 4000 helium atoms before pickup of Ba. The image is characterized by an isotropic angular and a smooth radial distribution. The speed distribution derived

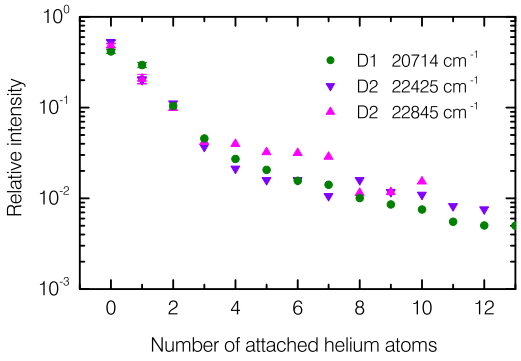

FIG. 1. Relative yield of Ba^+He_n exciplexes at selected excitation frequencies determined from time-of-flight mass spectra recorded for Ba^+ in droplets containing an average of 4000 helium atoms before pickup of Ba.

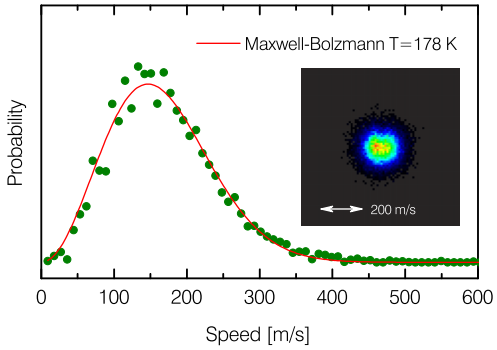

FIG. 2. Velocity map image (inset) and derived speed distribution recorded following excitation via the D1 transition at 20 714 cm^{-1} of Ba^+ embedded in droplets containing on average 4000 helium atoms. The solid line is a fit to a Maxwell-Boltzmann distribution corresponding to a translational temperature of 178 K.

from this image is shown in Fig. 2 and follows a Maxwell-Boltzmann distribution. A fit of the data yields a translational temperature for these ions of 178 ± 4 K. The resulting temperature is found to be independent of the size of the droplets and laser intensity. Excitation via the D2 transition yields also an isotropic angular and a Maxwell-Boltzmann speed distribution. Although the photon energy in this case is larger, the translational temperature is significantly lower, i.e., 96 ± 4 K. This temperature is found to be independent of droplet size, laser intensity, and excitation frequency within the D2 band. In addition to the velocity distributions of bare Ba^+ ions, those of the Ba^+He_n exciplexes have been determined. These too can be accurately described by Maxwell-Boltzmann distributions. The resulting translational temperatures are presented in Fig. 3. For excitation via the D1 transition one observes a rapid decay of the translational temperature with increasing number of helium atoms. For the larger exciplexes the temperature gradually levels off to a value of ~60 K. Excitation via the D2 transitions yields a clearly different temperature variation with the number of helium atoms. After a decay of the translational temperature for Ba^+He, it increases again for larger exciplexes before leveling

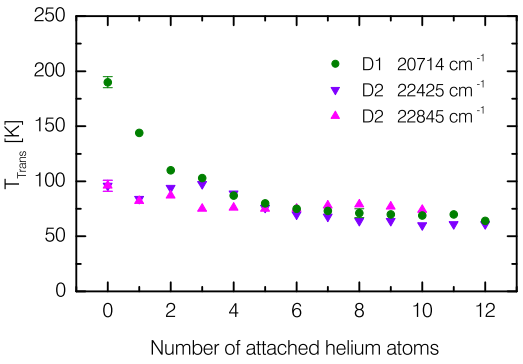

FIG. 3. Translational temperature of desolvated Ba^+ and Ba^+He_n exciplexes determined from speed distributions recorded following excitation of Ba^+ at selected frequencies.

off at approximately 60 K for the largest exciplexes. The temperatures of all species are significantly larger than the effective temperature corresponding to Ba^+ moving with the critical Landau velocity of 58 m/s, i.e., 28 K, indicating that the desolvation mechanism differs from that of Ag.[19]

The difference between the Ba^+He_n exciplex distributions and the translational temperatures of the exciplexes for D1 and D2 excitation clearly indicates that the dynamics induced by the excitation of the ions depends on the excited state. Spectroscopic studies of Ba^+ in bulk have revealed that 6p $^2P_{3/2}$ population relaxes quickly to the 6p $^2P_{1/2}$ state.[10] Consequently, one has to conclude that the overall dynamics is significantly affected by the 6p $^2P_{3/2} \rightarrow$ 6p $^2P_{1/2}$ relaxation process. Unfortunately, it is not possible to deduce any further details on the dynamics from the experimental data. To gain insight we have therefore performed dynamical simulations of excited $Ba^+@He_{1000}$ where we combine a classical treatment of the Ba^+ ion with a time-dependent DFT (TDDFT) description of the helium.

III. THEORETICAL APPROACH

A. He–Ba^+ pair potentials

One of the key ingredients for the dynamical simulations presented in this study are the potential energy curves (PECs) of the ground ^2S and the excited ^2P and ^2D states of the Ba^+–He dimer. Accurate PECs for this system have recently been computed by some of the present authors.[34,41] This section describes their salient features as well as additional calculations providing further support to their accuracy.

The available ground state potential[34] has been determined at the CCSD(T) level of theory using a high quality basis set both for Ba^+ and He, plus a set of bond functions placed midway between the two nuclei. As a test of the reliability of this PEC, we have conducted additional computations using the same level of theory, basis set for He, and set of bond functions, but a different pseudopotential for the core electrons of Ba^+ (Ref. 42) and a larger basis set for its valence electrons (QZVP).[43] The latter consists of 7s6p4d2f1g gaussian functions instead of 7s5p3d1f. The position of the minimum interaction energy and of the PEC turning point (i.e., the internuclear distance where the interaction potential becomes repulsive) shift towards shorter distances by less than 0.05 Å, and the attractive well becomes more attractive by roughly 2%. Such variations are not expected to play any relevant role in the dynamics of Ba^+–He_N aggregates when Ba^+ is in the electronic ground state, and hence in this study we adopted the interatomic potential presented in Ref. 34.

The Ba^+–He excited states relevant to the present investigation (the lowest ^2D and ^2P states) have already been determined using two variational approaches, i.e., Configurations Interaction including single and double excitations (CISD), and Multi-Reference Configurations Interaction (MRCI) containing up to triple excitations.[41] The two sets of potentials are quantitatively very similar, suggesting that the interaction energy is determined essentially by the induction component, the electron dispersion energy, and the Pauli repulsion at short internuclear distances.

Indeed, these terms are well described by single and double excitations, with minor contributions coming from higher order excitations, as already observed in the interaction between neutral coinage metal atoms and He.[44] As a possible alternative, we have tested a perturbative approach at second order, Multi-Configuration Quasi-Degenerate Perturbation Theory (MCQDPT) as implemented in the GAMESS-US computational code,[45] adopting the same pseudopotential and basis sets of the MRCI potentials.[41]

The ^{2}P excited state splits into a $^2\Sigma$ and two degenerate $^2\Pi$ states in Ba^+–He (spin-orbit effects are not considered at this stage). The $^2\Sigma$ state is highly repulsive, as the Ba^+ outermost electron occupies a *p* orbital pointing towards the helium atom. CISD, MRCI, and MCQDPT computations for this state yield very similar results, with differences in interaction energy measuring just a few percent along the entire range of internuclear distances considered. The PEC of the $^2\Pi$ state exhibits an attractive well due to the Ba^+ outermost electron occupying a *p* orbital perpendicular to the Ba^+–He internuclear axis, which allows the He to interact with the unscreened Ba^+ core. The attractive well predicted by the perturbative computations (516 cm^{-1} at the MCQDPT level) is more attractive by about 6% compared to variational data (485 cm^{-1} at the MRCI level of theory), and the turning point of the potential is shifted by few hundredths of an Å towards shorter distances.

The lower lying ^{2}D state splits into a single $^2\Sigma$ and two sets of doubly degenerate $^2\Pi$ and $^2\Delta$ states. The $^2\Sigma$ is highly repulsive, as the outermost electron of Ba^+ occupies the *d* orbital directed towards the He atom. We found no relevant differences among the CISD, MRCI, and MCQDPT potentials. The $^2\Pi$ and $^2\Delta$ states have quite large well depths of 373 cm^{-1} and 220 cm^{-1}, respectively, at the MRCI level. Perturbative computations predict the attractive well to be deeper by about 15% compared to the MRCI data, and the PEC to shift to shorter distances by about 0.10 Å.

Analogously to the ground state, the differences among the available potentials and the MCQDPT data are not expected to play a relevant role in the simulations of the dynamics of Ba^+–He_N aggregates following excitation. In the present investigation we adopt the MRCI potentials[41] for the description of ^{2}P and ^{2}D states. To aid the discussion of the results, we present in Fig. 4 the PEC corresponding to the ^{2}S, ^{2}P, and ^{2}D states with the spin-orbit interaction included as discussed in Refs. 41 and 46. The ^{2}S ground state PEC has already been used in the past to address the solvation of Ba^+ in helium nanodroplets.[33,34]

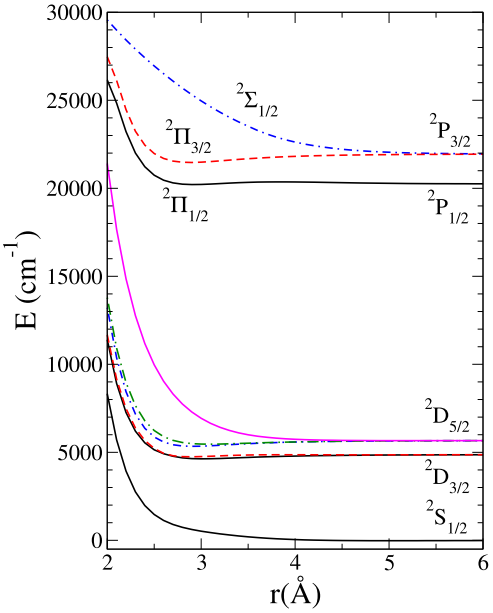

FIG. 4. ^{2}S, ^{2}P, and ^{2}D Ba^+–He pair potentials. The splitting introduced by the spin-orbit interaction has been included.

B. Static density functional theory (DFT)

Before starting dynamical calculations we first consider the energetics of the system using static DFT calculations. Barium atoms captured by helium droplets are known to reside in a dimple at the surface of the droplet,[47,48] an experimental fact well reproduced by DFT calculations.[49] If the Ba atom is subsequently photoionized, the resulting cation becomes solvated by the helium by sinking into the droplet.[30,34]

The energy available for this process is determined by the energy difference between the equilibrium configuration, corresponding to Ba^+ at the center of the droplet, and that corresponding to Ba^+ residing at the surface dimple. Both of these can be obtained by static DFT calculations. We have considered a droplet made of $N = 1000$ helium atoms and have first obtained the structure of the neutral Ba-droplet complex in the ground state. In view of the large mass of barium compared to that of helium, we describe the Ba atom and its cation as classical particles in the dynamics while their effect on the statics is incorporated as an external field acting upon the droplet.[36,50] Accordingly, the energy of the system is written as

$$E[\rho] = \int d\mathbf{r} \left\{ \frac{\hbar^2}{2m_{\mathrm{He}}} |\nabla \sqrt{\rho(\mathbf{r})}|^2 + \mathcal{E}_{\mathrm{He}}[\rho(\mathbf{r})] \right\} + \int d\mathbf{r}\, \rho(\mathbf{r})\, V_X(|\mathbf{r}_{\mathrm{Ba}} - \mathbf{r}|), \quad (1)$$

where $\mathcal{E}_{\mathrm{He}}$ is the potential energy density per unit volume, $\rho(\mathbf{r})$ is the He atom density at point $\mathbf{r}$, and $\mathbf{r}_{\mathrm{Ba}}$ is the impurity location.

The Ba^+–He and Ba–He ground state pair potentials V_X have been taken from Refs. 34 and 51, respectively. The density functional (DF) used in the present work is a modified version of the Orsay-Trento functional[52] able to handle very structured helium configurations as those expected to appear around fairly attractive impurities such as cations.[53]

Upon variation of Eq. (1) one obtains the Euler-Lagrange equation. The equilibrium helium density $\rho_0(\mathbf{r})$ and the location of the dopant atom $\mathbf{r}_{\mathrm{Ba}_0}$ can be determined from

$$\left\{ -\frac{\hbar^2}{2m_{\mathrm{He}}} \nabla^2 + \frac{\delta}{\delta \rho} \mathcal{E}_{\mathrm{He}} + V_X(|\mathbf{r}_{\mathrm{Ba}} - \mathbf{r}|) \right\} \Psi_0(\mathbf{r}) = \mu\, \Psi_0(\mathbf{r}), \quad (2)$$

where μ is the chemical potential of the He droplet and $\Psi_0(\mathbf{r}) \equiv \sqrt{\rho_0(\mathbf{r})}$. Eq. (2) has been solved in Cartesian coordinates using a spatial grid of 0.4 Å. The derivatives have been calculated with 13-point formulas. Extensive use of fast-Fourier techniques[54] has been made to efficiently calculate the energy density and mean field potential.

A two-dimensional view of the dimple state configuration of the neutral Ba atom can be seen in Fig. 2 of Ref. 34. The Ba atom is located 22.6 Å away from the center of the $^4He_{1000}$ droplet. Upon photoionization, the energy of the cation sitting at this position is obtained from Eq. (1) using the non-relaxed helium density and the Ba^+–He ground state pair potential. This yields an energy of −5622 K for the $Ba^+@^4He_{1000}$ system (the DFT energy of the pure $^4He_{1000}$ droplet is −5401 K). The helium density profile of $Ba^+@^4He_{1000}$ corresponding to the equilibrium position at the center of the droplet can be seen in Fig. 3 of Ref. 33. It has an energy of −6461 K. If we assume that the outgoing electron created in the ionization process does not transfer energy to the helium, an assumption justified by the corresponding photoelectron spectrum,[48] the energy deposited into the droplet by the photoionization process is calculated to be 839 K. In the course of the dynamics, part of this energy will be taken away by ejected helium atoms[34] and part will remain in the system shared between kinetic energy of the impurity and excited droplet modes.

Quasi-static Ba^+-droplet configurations in which the cation resides at a fixed distance from the center-of-mass (COM) of the helium moiety can be obtained by a constrained energy minimization.[55] Fig. 5 shows the energy of these quasi-static configurations, which we will refer to as "stretched configurations," as a function of the distance between the cation and the center-of-mass of the helium moiety, $\mathcal{Z}_0$. The energies are referenced to the equilibrium energy corresponding to $\mathcal{Z}_0 = 0$. The distance corresponding to the equilibrium position of the neutral Ba atom is indicated by an arrow. At this distance the energy of the stretched configuration is smaller than the energy deposited into the droplet upon ionization of the neutral Ba. This difference is because the stretched helium configuration has been obtained by minimization of the constrained energy whereas this is not the case for the dimple configuration, as discussed above.

If the system is stretched far enough, the droplet-Ba^+ complex breaks into a "charged minicluster" containing some 170 helium atoms tightly bound to the Ba^+ cation plus a neutral droplet with the remaining helium. Fig. 5 shows that the charged minicluster configuration is energetically favorable for $\mathcal{Z}_0 \gtrsim 38$ Å. Before the breaking, the stretched configurations display a preformed charged minicluster connected to the rest of the droplet by a "neck." Fig. 5 also shows the existence of metastable configurations of either kind before and after the crossing point. Also shown are the densities of a stretched and a minicluster configuration corresponding to $\mathcal{Z}_0 = 37.6$ Å whose energies only differ by 6.5 K. It is worth nothing that the system has to be significantly stretched to reach the scission point where the charged minicluster configuration appears, i.e., some 15 Å away from the original location of the neutral Ba atom on the droplet surface, whose radius is 22.2 Å for $N = 1000$. Such stretched

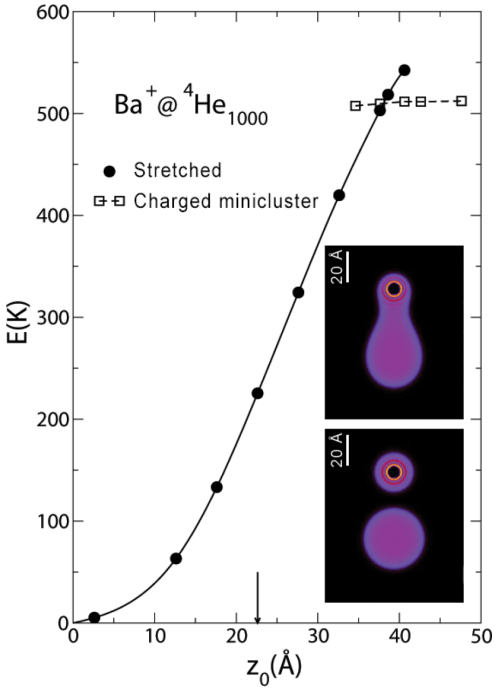

FIG. 5. Energy of the stretched configuration (solid line) as a function of the distance to the COM of the helium moiety. The dashed line represents the energy of the charged minicluster configuration. Both energies are referred to that of the equilibrium configuration of Ba^+ at the center of the droplet (−6461 K). Indicated by an arrow is the distance of the neutral Ba at the dimple surface to the center of the helium droplet before photoionization. Also shown are stretched and charged minicluster configurations, the latter containing about 170 He atoms, corresponding to $\mathcal{Z}_0 = 37.6$ Å.

scission configurations have been found in the past for the fission of ^3He droplets.[56]

This analysis indicates that the energy deposited into the droplet by the photoionization of the neutral Ba at the dimple (839 K) is in principle large enough to allow the appearance of stretched configurations leading to charged minicluster formation (509.5 K). However, actual dynamic calculations[36] indicate that this is rather unrealistic. We therefore conclude that the desolvation of excited Ba^+ cations as observed experimentally is not related to charged miniclusters formed upon ionization of the system.

To address the dynamics of the excited Ba^+ ion one has to resort to a time-dependent description. The more ambitious strategy consists of modeling the experiment, starting from the photoionization of the neutral Ba atom at the surface dimple and followed by the photoexcitation of the Ba^+ cation some time after its creation. The first part of this process has been reported in Ref. 34 where the dynamics of the cation in the ground state was followed for more than 200 ps. This is a long time period for the calculations but short compared to the experimental time scale. In the experiments the time delay between ionization and excitation is 185 ns using laser pulses having a duration of 5 ns. A less ambitious strategy assumes that during its dynamic evolution the ground state

Ba^+ cation has been taken to a stretched configuration from which it is then photoexcited to the ^2P manifold. In either approach, one might expect that excitation can lead to the desolvation of the cation either because the interaction of the droplet with the excited cation is repulsive—as in the case for the silver atom[36]—or because the helium supersonic density waves launched in the excitation process break the "neck" of the stretched configuration and simultaneously remove a sizable number of helium atoms initially located around the excited cation.

C. Time-dependent DFT

The dynamics presented in this work haven been obtained within the TDDFT approach.[57,58] We refer the reader to Refs. 32–37 for a thorough discussion of the approach and how it has been implemented in some applications. For the sake of completeness and to aid the discussion, we briefly discuss the method of Ref. 36. The basic ingredients are the Born-Oppenheimer approximation that allows to factorize the electronic and nuclear wave functions, the Franck-Condon approximation which assumes that the atomic nuclei do not change their positions or momenta during the electronic transition,[59] and the use of the diatomics-in-molecule approximation[60] that combined with DFT to describe the droplet-impurity complex allows factorizing the impurity and He nuclear components.

We introduce a complex effective wave function $\Psi_{\rm He}(\mathbf{r},t)$ representing the helium moiety that is evolved following the TDDFT prescription. The displacement of the cation position $\mathbf{r}_{\rm Ba^+}(t)$ is treated classically. The spin-orbit (SO) interaction is included as indicated in Ref. 61, by writing the electron angular momentum in Cartesian coordinates $i = x, y, z$ and the spin state as $s = \uparrow (m_s = 1/2), \downarrow (m_s = -1/2)$. The magnitude of the SO interaction is fixed to reproduce the spin-orbit splitting of bare Ba^+ in the 6p ^2P states being 1690.84 cm^{-1}.[62]

The evolution of the electronic excited state of Ba^+ is described by introducing an additional degree of freedom, a six-component vector $|\lambda\rangle$ written in terms of same basis for spin and angular momentum used for the SO interaction

$$|\lambda\rangle = \sum_{is} \lambda_{is} |i,s\rangle. \tag{3}$$

The vector is normalized $|\langle\lambda|\lambda\rangle|^2 = 1$. Notice that states as, e.g., $|x\uparrow\rangle$ are referred to in the literature as $p_x\uparrow$.[59] The complete set of dynamical variables characterizing the system thus consists of a complex effective wavefunction for helium $\Psi_{\rm He}(\mathbf{r},t)$ such that $\rho(\mathbf{r},t) = |\Psi_{\rm He}(\mathbf{r},t)|^2$, a vector position for the impurity, $\mathbf{r}_{\rm Ba^+}(t)$, and a 6-dimensional complex vector for its electronic state $|\lambda(t)\rangle$. The total energy of the $Ba^+@^4He_{1000}$ complex suddenly excited to the ^2P manifold is written as

$$\begin{aligned} E[\Psi,\mathbf{r}_{\rm Ba^+},\lambda] = &\int d\mathbf{r}\, \frac{\hbar^2}{2m_{He}}|\nabla\Psi|^2 + \frac{p^2_{\rm Ba^+}}{2m_{\rm Ba^+}} \\ &+ \int d\mathbf{r}\, \mathcal{E}_{\rm He}[\rho] + \langle\lambda|V_{SO}|\lambda\rangle \\ &+ \int d\mathbf{r}\, \rho(\mathbf{r})\, V_\lambda(\mathbf{r}-\mathbf{r}_{\rm Ba^+}). \end{aligned} \tag{4}$$

We have followed the prescription of Ref. 61 to write the pair potential as a direction-dependent combination of Π and Σ potentials determined in Ref. 41,

$$V_\lambda(\mathbf{r}) = \langle\lambda|\mathcal{V}(\mathbf{r})|\lambda\rangle = \sum_{ijss'} \lambda^*_{is}\mathcal{V}^{ijss'}(\mathbf{r})\lambda_{js'}, \tag{5}$$

where the six-dimensional matrix operator $\mathcal{V}$ has components

$$\mathcal{V}^{ijss'}(\mathbf{r}) = \left[V_\Pi(r)\delta_{ij} + (V_\Sigma(r) - V_\Pi(r))\frac{r_i r_j}{r^2}\right]\delta_{ss'}. \tag{6}$$

The following coupled 3D time-dependent system, resulting from the variation of the action, has to be solved to obtain the dynamical evolution of the system

$$\begin{aligned} i\hbar\frac{\partial}{\partial t}\Psi_{\rm He} &= \left[-\frac{\hbar^2}{2m_{\rm He}}\nabla^2 + \frac{\delta\mathcal{E}_{\rm He}}{\delta\rho(\mathbf{r})} + V_\lambda(\mathbf{r}-\mathbf{r}_{\rm Ba^+})\right]\Psi_{\rm He} \\ i\hbar\frac{\partial}{\partial t}|\lambda\rangle &= \mathcal{H}\ |\lambda\rangle, \\ m_{\rm Ba^+}\ddot{\mathbf{r}}_{\rm Ba^+} &= -\nabla_{\mathbf{r}_{\rm Ba^+}}\left[\int d\mathbf{r}\rho(\mathbf{r})V_\lambda(\mathbf{r}-\mathbf{r}_{\rm Ba^+})\right] \\ &= -\int d\mathbf{r}\,\nabla\rho(\mathbf{r})V_\lambda(\mathbf{r}-\mathbf{r}_{\rm Ba^+}), \end{aligned} \tag{7}$$

where the t-dependence of the dynamical variables is omitted for clarity. The electronic state Hamiltonian $\mathcal{H}$ is a 6×6 matrix whose elements are given by

$$H^{ijss'} = \int d\mathbf{r}\,\rho(\mathbf{r})\mathcal{V}^{ijss'}(\mathbf{r}-\mathbf{r}_{\rm Ba^+_0}) + V^{ijss'}_{SO}. \tag{8}$$

Equations (7) have been solved within the same box and using the same grid as for the static problem. The time step employed is 0.5 fs. We have used a predictor-modified-corrector method[63] fed by a few time steps obtained by a fourth-order Runge-Kutta-Gill algorithm.[63] When the energy deposited into the helium droplet is high enough as a consequence of the occurring physical process, it may happen that some helium density, representing evaporated helium atoms, leaves the droplet and eventually hits the box boundary. To prevent that these usually few "atoms" bounce back, we have included an absorbing potential.[64] As a result, particle—and thus energy—leaking appears when some helium density arrives near the walls of the calculation box where the absorbing potential acts. This leaking represents helium atoms leaving the droplet and the energy carried away by them.

To solve Eqs. (5)–(8) initial values for the variables are required. As starting configuration we have chosen that corresponding to the turning point reached by the Ba^+ in the ground state 223 ps after the ionization of neutral Ba in the surface dimple state.[34] At this time, the distance between the cation and the COM of the droplet is 11.1 Å. The associated helium density $\rho_0(\mathbf{r})$—or effective wave function $\Psi_0(\mathbf{r})$—and cation position $\mathbf{r}_{\rm Ba^+_0}$ define the initial conditions, as $\dot{\mathbf{r}}_{\rm Ba^+_0} = 0$ at the turning point. This starting configuration is shown in the top left panel of Fig. 6, together with the corresponding V_λ potentials.

There remains to fix the initial $|\lambda\rangle$ state. This has been done by choosing one of the eigenstates resulting from the diagonalization of the Hamiltonian $\mathcal{H}$ at the time of excitation. If the helium density is spherically symmetric

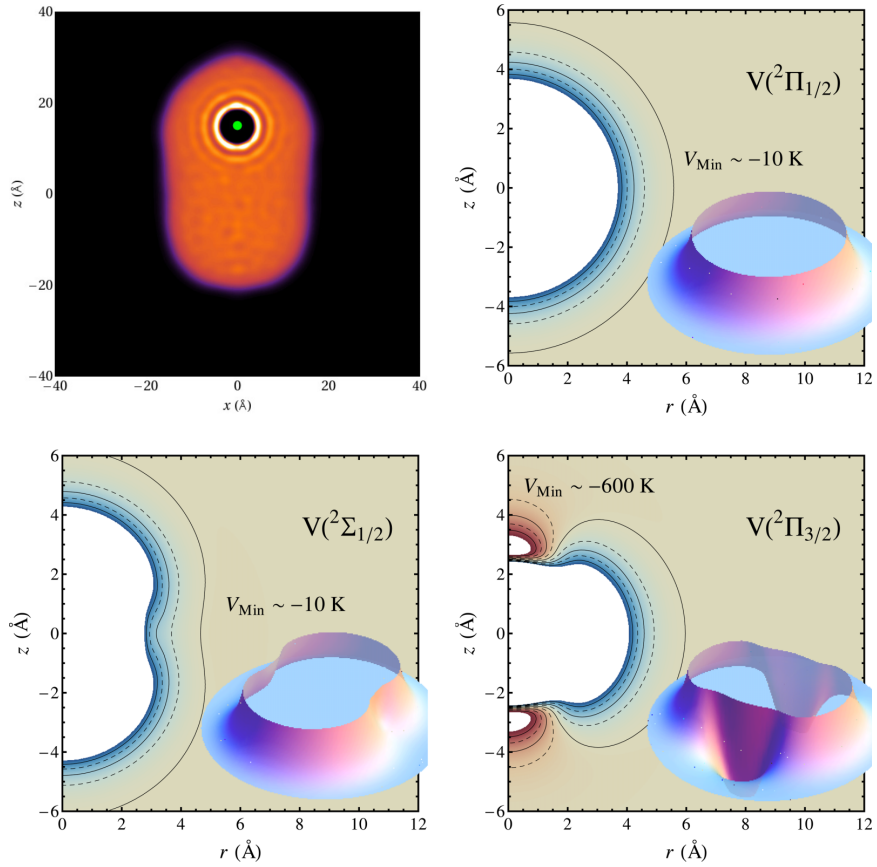

FIG. 6. Top left panel: Turning point of Ba^+ taken as starting configuration for the dynamics. The bright white spots correspond to high density regions. The other panels display the ^2P V_λ Ba^+–He potentials corresponding to this configuration. The isopotential lines are 100 K apart.

around the cation, the first term in the matrix defined by Eq. (8) is proportional to the identity.[61] As a result of the diagonalization one obtains the usual $J = 1/2$ and $J = 3/2$ eigenvectors pertaining to the spin-orbit interaction. However, when the cation is located off center, its environment is only axially symmetric. In this case, two of the V_{SO} eigenstates corresponding to $J = 3/2$ are eigenstates of the Hamiltonian $\mathcal{H}$, as are linear combinations of the other four. For the helium distributions considered here this effect turns out to be a small perturbation. The mixed eigenstates are such that they still have $\langle J\rangle \simeq 1/2$ and $\langle J\rangle \simeq 3/2$. This allows us to label the electronic states that we take as initial condition for the dynamics as $|\lambda\rangle = |\widetilde{3/2}\rangle$ for the pure $J = 3/2$ state, and $|\lambda\rangle = |\widetilde{1/2}\rangle$ and $|\lambda\rangle = |\widetilde{3/2}\rangle$ for the mixed states. In a more conventional notation the $|\widetilde{1/2}\rangle$ configuration is referred to as $^2P_{1/2}$ (D1), while the other two electronic states $|\widetilde{3/2}\rangle$ and $|\widetilde{\widetilde{3/2}}\rangle$ are referred to as the $^2P_{3/2}$ (D2) configuration. There are different possibilities to label the excited states of the Ba^+-droplet complex. In the following we adhere to the Hund's case (a) notation, as discussed, e.g., in Ref. 65. In this scheme the electronic states are labeled as $^{2S+1}\Lambda_\Omega$, S being the spin of the system, Λ being the projection of the orbital angular momentum onto the axis, defined by the cation and the COM of the helium droplet, and Ω being the projection of the total electronic angular momentum onto this axis.

The three V_λ potentials $V(^2\Pi_{1/2})$, $V(^2\Pi_{3/2})$, and $V(^2\Sigma_{1/2})$ corresponding to the eigenvectors $|\widetilde{1/2}\rangle$, $|\widetilde{3/2}\rangle$, and $|\widetilde{\widetilde{3/2}}\rangle$ respectively, are shown in Fig. 6 for the ρ_0 density corresponding to the selected turning point. Because the Σ pair potential is mostly repulsive and the Π pair potential has a deep attractive well, the resulting V_λ potentials, see Eq. (6), have quite different shapes. $V(^2\Pi_{1/2})$ is spherically symmetric and has a minimum of about 10 K at a distance of 6.5 Å and becomes repulsive at a distance of 5.5 Å. $V(^2\Sigma_{1/2})$ is similar but is not spherically symmetric as it has an annular minimum of about 10 K. The $V(^2\Pi_{3/2})$ potential reveals two deep wells with depths of about 600 K that are localized along the symmetry axis of the system. Hence, exciplex formation for this excited Ba^+ state is very likely. Indeed, in cold helium gas efficient exciplex formation has been detected for Ba^+ excited to the $^2P_{3/2}$ state.[66]

The excited state potentials, V_λ, play a crucial role in the dynamical evolution of the system, see Eqs. (7). Their characteristics allows one to infer the outcome of the dynamics without performing actual time-dependent calculations. The depths of the $V(^2\Pi_{1/2})$ and $V(^2\Sigma_{1/2})$ potentials are rather

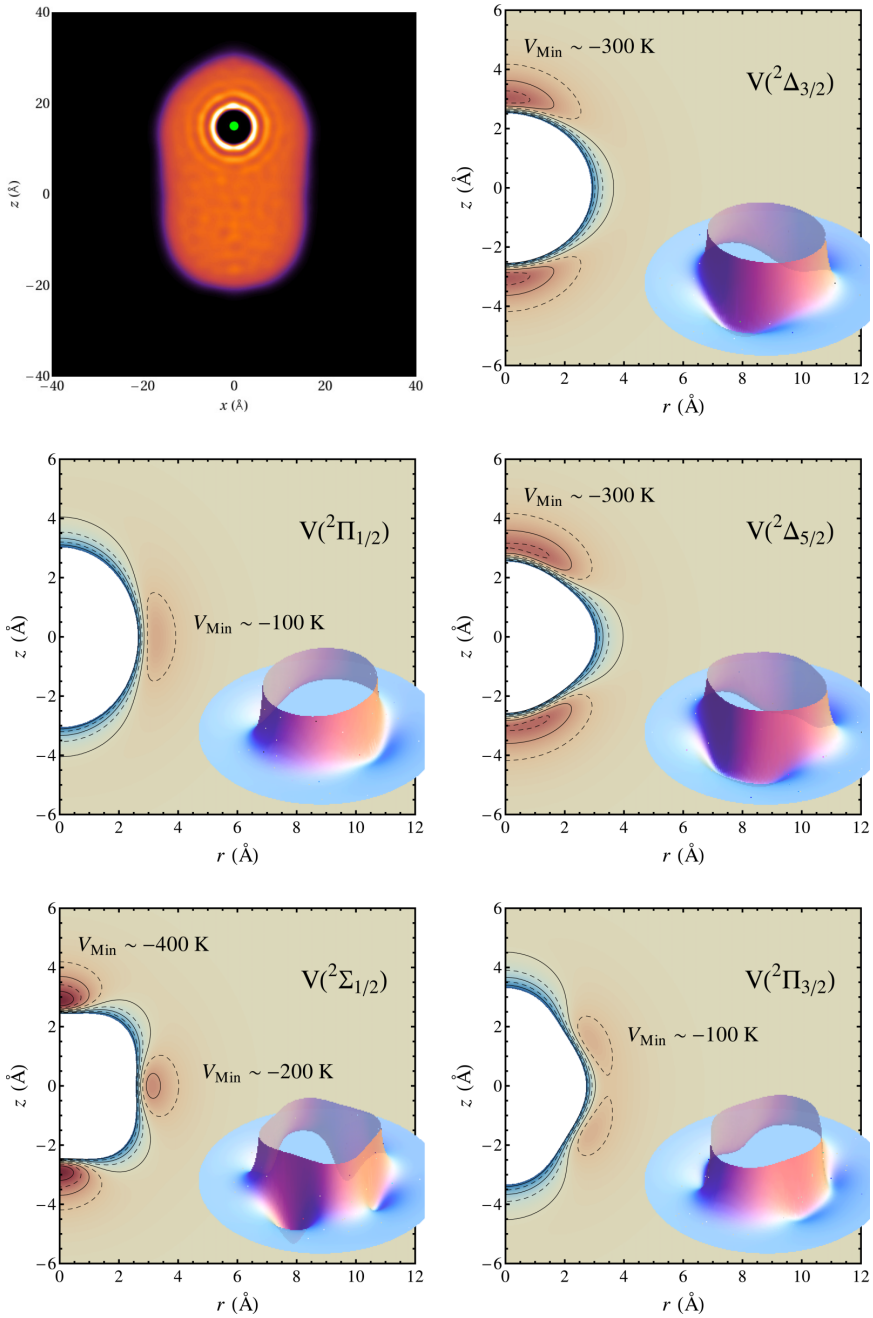

FIG. 7. ^2D V_λ Ba^+–He potentials corresponding to the same turning point configuration of Fig. 6 shown again in the top left panel. The isopotential lines are 100 K apart. The states $^2\Delta_{3/2}$ and $^2\Pi_{1/2}$ correlate with the $^2D_{3/2}$ state, and the states $^2\Delta_{5/2}$, $^2\Sigma_{1/2}$, and $^2\Pi_{3/2}$ with the $^2D_{5/2}$ state.

similar to that of the He-He potential. Consequently, it is questionable whether the Ba^+ cation will be ejected from the droplet if it is excited to any of the corresponding states. In contrast, the corresponding potentials for silver, which has been found to be ejected from the droplets, are much shallower.[36,39] Analogous to silver, the $V(^2\Pi_{3/2})$ potential is very attractive and the excited Ba^+ is expected to remain attached to the droplet. To further assess the possible ejection, let us consider the Ancilotto parameter for these potentials[67] which is defined as $\lambda_A = \rho\,\epsilon\, r_{min}/(2^{1/6}\sigma)$, where ϵ and r_{min} are the depth and position of the He-impurity pair potential well, and ρ and σ are the density and surface tension of liquid

helium. For values of $\lambda_A \gtrsim 1.9$, the impurity will be solvated inside the liquid. The $V(^2\Pi_{1/2})$ and $V(^2\Sigma_{1/2})$ potentials yield $\lambda_A \sim 4.6$, suggesting that a Ba^+ cation excited to these states will not be ejected. For comparison, we find $\lambda_A \sim 0.5$ for Ag. Even if we consider the motion of the Ba^+ cation inside the droplet, ejection is very unlikely since the translational energy for a cation produced by photoexcitation of the neutral atom at the surface has been found to be small.[34] Finally, we would like to point out that the experimentally observed speed distributions of Ba^+ and Ag are quite different. While those of Ag are well described by a Gaussian with a cut off at high speeds, those of Ba^+ can be described by Maxwell-Boltzmann distribution. This seems to suggest that desolvation of both species is governed by different processes.

Having in mind these expectations, we have followed the dynamic evolution of the system for some particular starting configurations after photoexciting the Ba^+ cation. These correspond to turning points and passages through the droplet center as found in the dynamical calculations of the ground state Ba^+ ion; if the starting configuration is not a turning point, the initial velocity of the photoexcited cation, $\dot{\mathbf{r}}_{Ba_0^+}$, is that of the Ba^+ cation at the photoexcitation point. In the case corresponding to the turning point at 223 ps discussed above, we have found that after excitation of the Ba^+ cation to the $|^2\Sigma_{1/2}\rangle$ state, which is most favorable for ejection, the ion bubble first expands to adjust to the larger radius of the excited state, and eventually moves towards the center of the droplet. Similar observations have been made for other starting configurations. In all cases no ejection of the excited Ba^+ was found.

Additional calculations have been performed using as starting configuration the metastable stretched configuration corresponding to $\mathcal{Z}_0 = 44.6$ Å. Since the bubble containing the ion is larger in the excited states, excitation of the ion will cause an outgoing density wave which might lead to the breaking of the neck and lead to the desolvation of the Ba^+ cation. However, the calculations reveal that the density waves are unable to break the neck for this extreme configuration. This leads us to conclude that the excited Ba^+ cation is not ejected from the helium droplet within the present approach.

Analogous to the ^{2}P states, we have calculated the interaction potentials for the ^{2}D states of Ba^+. These states might play a role in the cation dynamics as they might become populated following radiative decay from the $^2P_{1/2}$ state of the cation. We present in the Appendix a generalization of the method of Ref. 36 to describe the dynamics in the ^{2}D manifold. Fig. 7 shows the Ba^+–He V_λ potentials relevant for the dynamics and the calculation of the emission spectrum presented in Sec. IV. These V_λ potentials are all very attractive with wells more than 100 K deep yielding cation bubbles whose radius is smaller than that of the ^{2}P states. Based on these characteristics of the potentials we conclude that it is unlikely that Ba^+ is ejected from the droplets after population of the ^{2}D states by radiative decay from ^{2}P states.

D. Exciplexes

Since the experiments reveal efficient Ba^+He_n exciplex formation, we have explored the formation of exciplexes around Ba^+ $^2P_{1/2}$ and their possible ejection from the droplets. As we will show in Sec. IV, these exciplexes also play an important role in the emission spectrum of the photoexcited cation.

The rationale for this exploration is provided by diffusion Monte Carlo (DMC) calculations that found stable linear $Ba^+(^2\Pi_{1/2})He_2$ complexes with a distance of some 3 Å between the central Ba^+ ion and the two He atoms.[41] This distance is smaller than the radius of the excited cation bubble, as can be seen from Fig. 6. The bubble and linear configurations are separated by an energy barrier that apparently the TDDFT dynamics reported above has not been able to overcome. At variance, the formation of the $Ba^+(^2\Pi_{3/2})He_2$ complex is a barrierless process whose existence has been found in the present TDDFT dynamics. The DMC calculations furthermore reveal the existence of ring-like $Ba^+(^2\Pi_{1/2})He_n$ configurations for $n < 8$.[41]

Interestingly, linear and ring Cs^*He_n exciplexes were also found in solid helium[68–70] and discussed within a model that can be straightforwardly applied to Ba^+. Although being far much simpler than DFT and DMC approaches, the model is realistic enough to allow for a semi-quantitative description of $Ba^+(^2\Pi_{1/2})He_n$ and $Ba^+(^2\Pi_{3/2})He_n$ complexes. Thus, it is worth digressing from DFT and present its the results which will serve as a guide for more involved developments.

Following Refs. 68 and 71, the interaction between the Ba^+ cation and n He atoms is described by Eq. (8), fixing the origin of coordinates at the cation location and replacing the integral over the density by a sum on the He atoms. For the linear $n = 2$ configuration, both He atoms are axially located on opposite sides of the Ba^+ cation at a distance r. For the $n > 2$ ring configurations the He atoms are evenly distributed along a ring of radius r centered at the cation. The total He-He energy is then added to the cation-He interaction as a sum of pair interactions. We have taken for the He-He interaction the screened Lennard-Jones potential that enters the definition of the Orsay-Trento functional and have checked that the results presented below are sensibly the same if one uses the He-He Aziz potential.[72] After adding the spin-orbit interaction, one obtains the total energy of the complex as a function of r.

Diagonalizing the total energy for a given n as a function of r yields the PECs that correlate with the $^2P_{3/2}$ and $^2P_{1/2}$ He-cation potentials at long distances. Fig. 8 displays these PECs for $n = 2$ and 7. Both PEC reveal a minimum at $r \sim 3$ Å, indicating that linear and ring exciplexes can be formed for Ba^+ $^2\Pi_{1/2}$. The exciplex energy, taken as the well depth of the $Ba^+(^2\Pi_{1/2})He_n$ PEC, is displayed in Fig. 9 as a function of n. As for Cs^*He_n and Rb^*He_n exciplexes,[68,71] the exciplex energy increases with increasing n, except between $n = 2$ and $n = 3$. Eventually, for $n > 7$ the distance between neighboring He atoms becomes so small that the He-He repulsion starts to compete with the cation-He attraction. Also shown in this figure is the height of the energy barrier connecting the potential well and the free ion. It shows a dramatic increase going from $n = 2$ to $n = 3$, indicating that the formation of small exciplexes will be most efficient.

The ^{2}D states can also be incorporated in the simplified exciplex model discussed above by using the expressions in

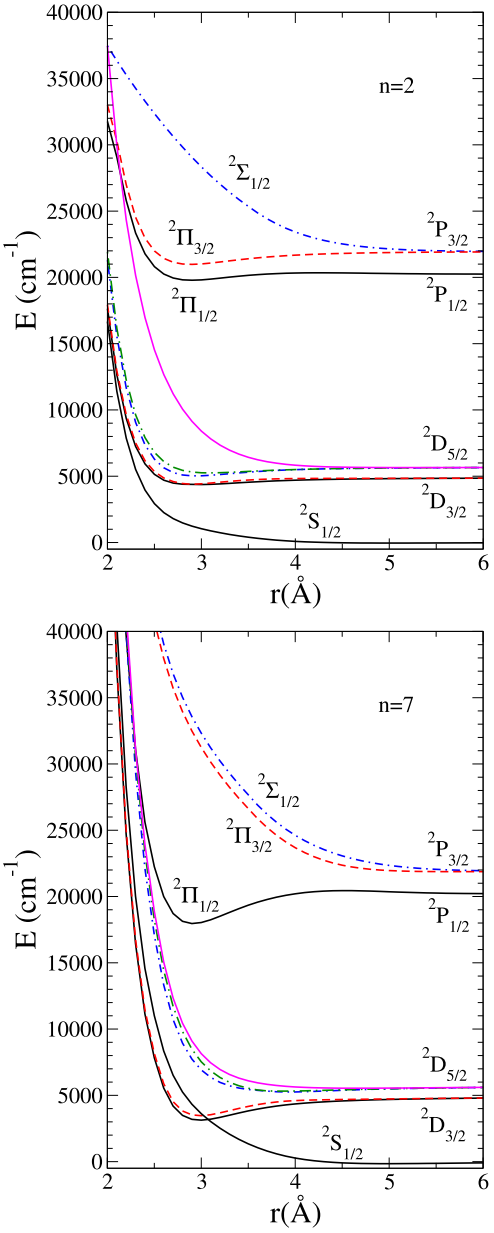

FIG. 8. Top panel: $Ba^+(^2\Pi_{1/2})He_2$ PEC as a function of the distance r between each He atom and the Ba^+ cation. Bottom panel: $Ba^+(^2\Pi_{1/2})He_7$ PEC as a function of the radius r of the ring exciplex. In both cases, for a given r we also display the energy of the ^2S and ^2D PEC obtained for the same linear or ring configuration.

the Appendix. A straightforward calculation similar to that carried out for the ^2P states yields the PECs in Fig. 8 that correlate to the $^2D_{5/2}$ and $^2D_{3/2}$ states of Ba^+ at large r values. For completeness and further reference we also show in the figure the He-Ba^+ PEC correlating to the $^2S_{1/2}$ state of the Ba^+ cation obtained by using the He-Ba^+ ground state pair potential.

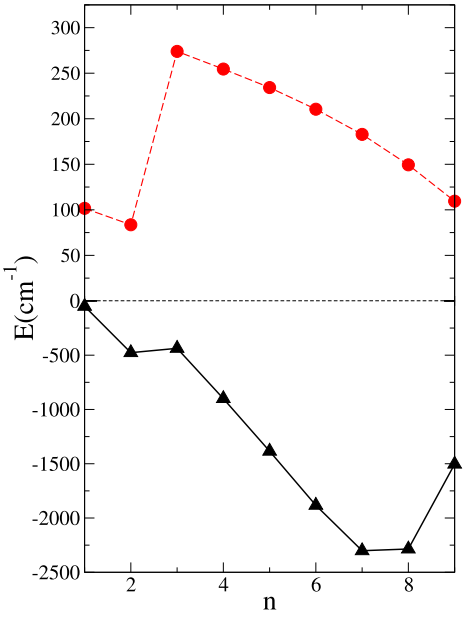

FIG. 9. Exciplex energy (bottom panel) and barrier height (top panel) of $Ba^+(^2\Pi_{1/2})He_n$ configurations as a function of n referred to the energy of the $^2P_{1/2}$ state of the Ba^+ cation.

IV. EMISSION SPECTRUM

As discussed above, $Ba^+(^2\Pi_{1/2})He_n$ exciplex formation might play a role in the dynamics and therefore has been addressed within the DFT approach. Before attempting to model the desolvation we first analyze the emission spectrum of the cation from the ^2P to the ^2S ground and the ^2D excited states. This allows us to verify the method by comparing the calculated emission spectra with those recorded in bulk helium.[10] The experimental emission spectrum was found to be identical for D1 and D2 excitations and to consist of three bands located at 491 nm (20 366 cm^{-1}), 523 nm (19 120 cm^{-1}), and 648 nm (15 432 cm^{-1}). A comparison of the free cation transitions and the experimental spectra indicates that the resonances at 20 366 cm^{-1} and 15 432 cm^{-1} likely correspond to the $^2S_{1/2} \leftarrow {}^2P_{1/2}$ and $^2D_{3/2} \leftarrow {}^2P_{1/2}$ transitions involving the $Ba^+(^2\Pi_{1/2})$ *bubble* configuration.[10,11] No emission lines were experimentally detected that could be associated to transitions from the $^2P_{3/2}$ state. This was interpreted that following excitation via the D2 band the population of the $^2P_{3/2}$ states quickly relaxes to the $^2P_{1/2}$ state.[10] Recently it has been argued[41] that the line observed at 19 120 cm^{-1}, for which no conclusive explanation was offered at the time, might arise from the emission from the $Ba^+(^2\Pi_{1/2})He_2$ exciplex.

To calculate the emission spectrum within DFT, we have to determine the relaxed helium configuration around the $|\lambda\rangle$ ^2P states—defined in Eq. (3)—of a Ba^+ cation located at the center of a $^4He_{1000}$ droplet. The size of this droplet is large enough to allow for a sensible comparison with the emission spectrum in bulk liquid helium. We look for stationary solutions to Eqs. (7) by introducing the usual t-dependence for stationary states

$$\Psi_{\mathrm{He}}(\mathbf{r},t) \rightarrow e^{-\imath\mu t/\hbar}\Psi_{\mathrm{He}}(\mathbf{r}),$$
$$|\lambda(\mathbf{r},t)\rangle \rightarrow e^{-\imath\epsilon_\lambda t/\hbar}|\lambda(\mathbf{r})\rangle, \quad (9)$$

where μ is the helium chemical potential and ϵ_λ is the eigenvalue of the electronic state of the excited Ba^+ in the presence of helium. Placing the impurity at $\mathbf{r}_{Ba^+} = 0$ and keeping it at rest, the relaxed configuration is obtained by solving the coupled equations

$$\left[-\frac{\hbar^2}{2m_{\mathrm{He}}}\nabla^2 + \frac{\delta\mathcal{E}_{\mathrm{He}}}{\delta\rho(\mathbf{r})} + V_\lambda(\mathbf{r})\right]\Psi_{\mathrm{He}} = \mu\,\Psi_{\mathrm{He}},$$
$$\mathcal{H}|\lambda\rangle = \epsilon_\lambda\,|\lambda\rangle, \quad (10)$$

where $V_\lambda(\mathbf{r})$ has been defined in Eq. (5). The procedure to determine the relaxed configuration is as follows:

1. Define a sensible helium density configuration, e.g., corresponding to the ground state Ba^+ cation at the center of the droplet.
2. Determine the internal electronic states corresponding to that helium density by diagonalizing Eq. (8). This yields three two-fold degenerate states $|\lambda\rangle$. Choose one of them and build the potential $V_\lambda(\mathbf{r})$, Eq. (5).
3. Using $V_\lambda(\mathbf{r})$, carry out a relaxation step as indicated by the first Eq. (10) to determine the new $\rho(\mathbf{r})$ and $\mathcal{H}$. Iterate until μ and ϵ_λ converge.

For the calculation of the emission spectrum we focus on the $V(^2\Pi_{1/2})$ potential, since all experimentally observed emission originates form the $^2P_{1/2}$ state. Fig. 10 shows the relaxed $Ba^+(^2\Pi_{1/2})$ bubble state (top left configuration) using the helium density configuration corresponding to the ground state Ba^+ cation as initial guess. Comparison of the helium density profiles reveals an increase of the ion bubble radius with approximately 1.2 Å. Upon convergence, the total energy of the droplet-Ba^+ complex is given by

$$E[\Psi,\mathbf{r},\lambda] = \int d\mathbf{r}\,\frac{\hbar^2}{2m_{He}}|\nabla\Psi|^2 + \int d\mathbf{r}\,\mathcal{E}_{\mathrm{He}}[\rho]$$
$$+\langle\lambda|V_{SO}|\lambda\rangle + \int d\mathbf{r}\,\rho(\mathbf{r})\,V_\lambda(\mathbf{r}). \quad (11)$$

Evaluation of this expression reveals that relaxation of the helium lowers the energy of the system by 575 cm^{-1}, see Fig. 10.

The method outlined above works well provided the electronic state Hamiltonian is dominated by the spin-orbit term, as it is for bubble configurations. At variance, for exciplex configurations the contribution of the helium term to Hamiltonian Eq. (8) has been found to be more sizeable and finding these configurations has required a somewhat different strategy, since the present method always leads to bubble configurations.

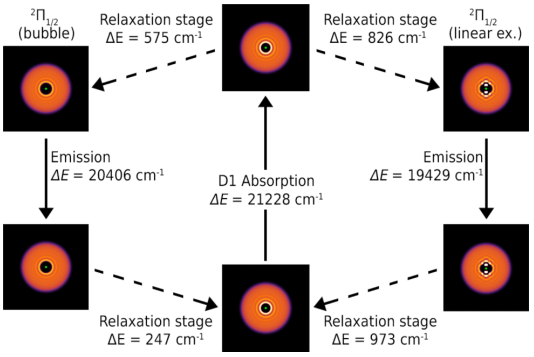

FIG. 10. Cation-helium configurations at different stages of the $^2S \rightarrow {}^2P \rightarrow {}^2S$ absorption-emission cycle. Left-hand cycle: Relaxation around the $Ba^+(^2\Pi_{1/2})$ bubble state. Right-hand cycle: Relaxation around the $Ba^+(^2\Pi_{1/2})$ linear exciplex. The energies of the radiative transitions and of the relaxation stages are indicated.

The $Ba^+(^2\Pi_{1/2})He_n$ exciplex configurations can be readily obtained by starting from a bubble configuration for the helium density supplemented with an electronic state $|\lambda\rangle$ appropriate for the sought-after exciplex. This state is previously determined within the simplified model of Refs. 68 and 71. Upon relaxation of both the helium density and electronic state, the exciplex configuration is obtained. Figure 11 shows two DFT configurations corresponding to a linear and ring exciplex similar to the DMC sampled configurations discussed in Ref. 41. It is worth noticing that the exciplexes persist as isolated entities even in the presence of the other helium atoms making up the droplet. More precisely, we find that both exciplexes are fully contained inside the cation bubble. Calculation of the energy reveals that the linear exciplex configuration is 251 cm^{-1} more stable than the relaxed bubble configuration, see Fig. 10. Based on the energetics one expects that excitation of the Ba^+ cation leads to exciplex formation, as experimentally observed.

Integrating the helium density inside the Ba^+ bubble we find that it corresponds to ^{4}He atoms for the linear structure,

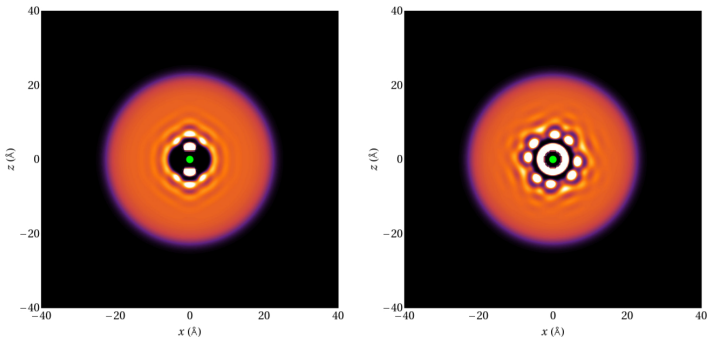

FIG. 11. Left panel: $Ba^+(^2P_{1/2})$ linear exciplex. Right panel: $Ba^+(^2P_{1/2})$ ring exciplex. Both exciplexes induce some replicas (density "blobs") at or near the cation bubble surface.

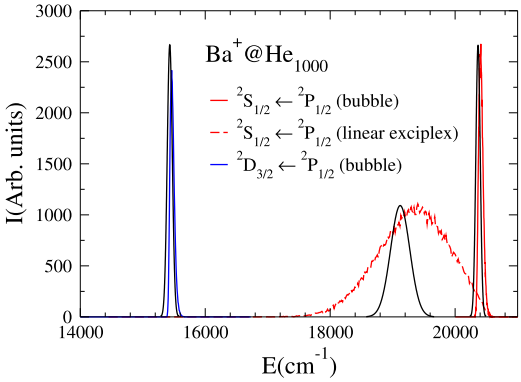

FIG. 12. Emission spectrum obtained from the de-excitation of the relaxed $^2P_{1/2}$ state of the Ba^+ cation. The gaussian lines in black are the experimental results of Ref. 10.

and to 12 atoms for the ring structure. The DFT approach thus has a tendency to overestimate the helium contents by about a factor of two in the regions of space where the fluid is strongly confined by very attractive interaction potentials. Hence, these high density spots should be taken with care if one identifies them with atoms. This drawback can only be cured by going beyond the fluid-like description inherent to DFT and switching to a discrete, atomic-like description, which is beyond the scope of the present work.

Once the relaxed helium configurations have been determined, their energies can be readily calculated. As can be seen in Fig. 10, for the ground state the exciplex is highest in energy. Based on these energy calculations the emission spectrum of the $Ba^+(^2\Pi_{1/2})$ linear exciplex is expected to be red-shifted with respect to that of the $Ba^+(^2\Pi_{1/2})$ bubble state by approximately 1000 cm^{-1}. The actual calculation of the emission spectrum proceeds in a way similar to that of the absorption spectrum as described, e.g., in Ref. 61. More relevant details of the procedure are given in the Appendix. Fig. 12 shows the calculated emission lines from the $Ba^+(^2\Pi_{1/2})$ bubble state to the $^2S_{1/2}$ and $^2D_{3/2}$ states, together with the emission line of the $Ba^+(^2\Pi_{1/2})$ linear exciplex state to the $^2S_{1/2}$ state. For comparison we also show the reconstructed experimental spectrum.[10] The agreement between theory and experiment is rather good, confirming the suggestion that the experimentally observed line at 19 120 cm^{-1} corresponds to emission from the $Ba^+(^2\Pi_{1/2})$ linear exciplex to the ground state.[41] The larger linewidth found in the calculations for this transition is likely related to the overestimation of the number of helium atoms in the linear exciplex, as mentioned before. The transitions of the $Ba^+(^2\Pi_{1/2})$ linear exciplex to the various D states have also been calculated and fall in the region of 14 000–16 000 cm^{-1}. However, no experimental emission spectrum has been reported in this region of the spectrum.[10]

V. EXCIPLEX DYNAMICS

The experiments reveal a large yield of small Ba^+He_n exciplexes. In agreement with this result the static calculations find that the formation of linear exciplex is energetically favorable. To address the role of complexes in the dynamical evolution of the system we have investigated the complex formation within the TDDFT framework. As before, we arbitrarily start from the turning point configuration of ground state Ba^+ 223 ps after the ionization of the neutral Ba atom. But instead of taking as initial vector state $|\lambda\rangle$ an eigenstate of $\mathcal{H}$, we choose, as indicated in Sec. IV, a vector state corresponding to an exciplex configuration. The justification for this choice being that such a distribution will be probed by helium density fluctuations. As shown in the movies related to Fig. 13 (Multimedia view), we find that during the first picoseconds following the excitation the helium density adjusts to form a linear exciplex. This exciplex is tightly bound to the droplet and remains almost stationary while density waves travel through the helium droplet. Analogous to our observations for the bubble configurations discussed above we find that the exciplex is not ejected during the further evolution of the systems.

Inspection of the potential energy curves for the exciplexes in Fig. 8 reveals that at the exciplex $^2P_{1/2}$ equilibrium distance the energy of the ground state configuration is strongly increased. Consequently, upon radiative relaxation to the ground state this large amount of energy will be released into the droplet. To determine whether this could lead to the desolvation of Ba^+, we have followed the dynamics of the system after de-excitation. The results can be seen in the movies related to Fig. 13 (Multimedia view), where we show the formation of the linear exciplex when the cation is

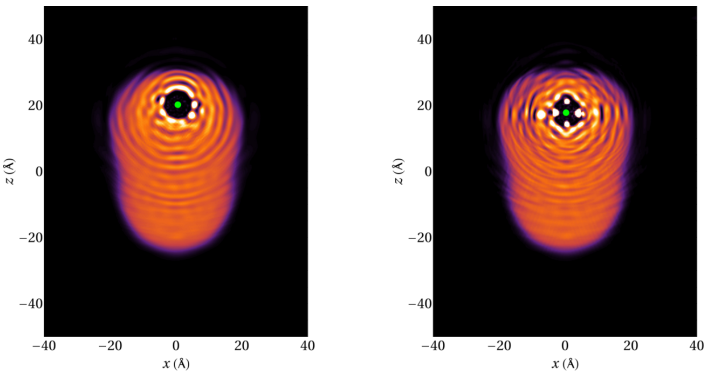

FIG. 13. 2D He densities 5 ps after de-excitation from the $P_{1/2}$ linear exciplex configuration to the $^2S_{1/2}$ (left) and $D_{3/2}$ states (right). (Multimedia view) [URL: http://dx.doi.org/10.1063/1.4942850.1][URL: http://dx.doi.org/10.1063/1.4942850.2]

about to reach the turning point at 223 ps and its subsequent evolution after being de-excited to the $^2S_{1/2}$ and $^2D_{3/2}$ states. To distinguish the formation and de-excitation stages, we have represented the cation with different colors, yellow for the former and green for the latter process. Inspection of the movies related to Fig. 13 (Multimedia view) reveals a fast formation of the exciplex as discussed above. After 5 ps the system is de-excited to either the $^2S_{1/2}$ or the $^2D_{3/2}$ state. In both cases, the helium quickly rearranges around the Ba^+ due to the change in interaction potential. As expected, relaxation to the $^2S_{1/2}$ ground state leads to the formation of a bubble configuration. In contrast, relaxation to the $^2D_{3/2}$ state leads to the formation of a non-linear exciplex. The transitional motion of the Ba^+ is found to depend strongly on the electronic state. After relaxation to the $^2D_{3/2}$ state the Ba^+ remains almost stationary, while following relaxation to the $^2S_{1/2}$ state the ion is accelerated towards the surface of the droplet. However, before the Ba^+ can escape from the droplet it is accelerated back towards the center of the droplet. Based on these results we conclude that radiative relaxation of Ba^+ $^2P_{1/2}$ does not lead to desolvation of the cation.

VI. DISCUSSION AND OUTLOOK

We have carried out a combined experimental and theoretical investigation of the dynamics of Ba^+ cations in helium droplets photoexcited to the 6p ^2P manifold. An analysis of the experimental results has been carried out within a full dynamical, three dimensional approach that combines a time-dependent DFT description of the helium with a classical dynamics description of the impurity. This theoretical approach has been successfully employed in the past to describe a wide variety of experimentally observed dynamical processes.[32–37] In the present study it successfully reproduces the experimental emission spectrum of the Ba^+ cation.[10] The calculated spectrum depends critically on the helium configurations around the excited ^2P Ba^+ impurity. The good agreement with experiment implies that our DFT approach correctly describes the static and dynamic formation of Ba^+He_n exciplexes as well. In spite of these achievements, the method does not yield the desolvation of excited Ba^+ ions found in the experiments. This raises the question as to what causes this discrepancy.

A first issue to discuss in this context is the interpretation of the experimental data. The suggestion that Ba^+ cations are ejected from the helium droplets is based on time-of-flight mass spectra which reveal an increase in the number of Ba^+ ions and Ba^+He_n exciplexes accompanied by a reduction of signal corresponding to ion-containing helium droplets. However, the signal-to-noise ratio of the mass spectra on which this conclusion is based is rather low due to the presence of a large background in the mass range corresponding to the ion doped droplets. As a result it becomes difficult to determine whether the ion-doped droplet signal is depleted, which would indicate ejection of the ion, or shifted to lower mass which would be compatible with a (partial) evaporation of the droplet. Furthermore, it has not been possible to determine the state distribution of the Ba^+ cations, which could provide another indication on the desolvation process. However, the fact that emission spectra of Ba^+ have been recorded in bulk helium indicates that non-radiative relaxation is not very efficient.[10] Although without additional information about the lifetime non-radiative relaxation cannot be completely ruled out, this result suggests that the excited Ba^+ cations are ejected from the droplets.

Experiments on Ag excited in helium droplets have revealed that the ejected atoms have a well-defined speed distribution, indicative of a critical Landau velocity.[19] In contrast, the speed distributions of the Ba^+ ions and Ba^+He_n exciplexes are best described by Maxwell-Boltzmann distributions. Such distributions suggest the presence of a thermally driven process, like evaporation. However, the temperatures corresponding to the observed speed distributions are found to be independent of droplet size and largest for excitation of the lowest energy state, $^2P_{1/2}$, see Fig. 3. This seems to contradict a simple thermally driven evaporative model. Hence, the experimental data are not conclusive regarding the desolvation mechanism of excited Ba^+ cations.

Concerning the theoretical description, one of the key ingredients is the interaction potentials between the Ba^+ cation and the helium. The potentials are calculated using the diatomics-in-molecule approach based on the Ba^+–He pair potentials. These have been computed at a high level of theory using large basis sets and have been corrected for basis set superposition errors. Comparison of the potentials with those using less accurate methods and smaller basis sets reveals only minor differences. We therefore expect that the potentials used are sufficiently accurate to correctly describe the dynamics of the excited system.

Since we use the diatomics-in-molecule approach for the interaction potentials, many-body interactions are not fully included. While neglecting such interactions is justified for weakly interacting neutral atoms, it is not obvious that this approach is justified for ionic species since the charge readily polarizes the surrounding helium. In order to estimate the effect of many-body interactions for the Ba^+–He_N system, we have explored three-body effects in the ground state of the Ba^+–He_2 complex. Computations have been performed at the CCSD(T) level of theory, adopting for barium and helium the same pseudopotential and basis set selected for the Ba^+–He ground state. No set of bond functions has been added, since test computations proved that their role in recovering three-body effects is negligible. The counterpoise correction has been performed using the scheme proposed by Valiron *et al.*[73] We have sampled the attractive and the repulsive regions of the PES in four sets of atomic arrangements: linear He–Ba^+–He and Ba^+–He–He, 90° bent He–Ba^+–He, and isosceles triangle with He-He as the basis. The general outcome of these computations is that three-body effects are very small (i.e., below 0.5 K) as far as the attractive part of the Ba^+–He_2 PES is considered, while they become significant at the repulsive region of the PES. However, this region is hardly sampled during the dynamical simulations.

Even though three-body effects are almost negligible with respect to the overall two-body contribution in the attractive region of the potential, theoretical computations performed on the Na^+–He_N[74] and Pb^+–He_N and Pb^{2+}–He_N[75] systems

indicate that they play a relevant role in the determination of the solvation structure of relatively small clusters. It was furthermore found that the charge-induced dipole interaction term in the cation-helium interaction pair potential tends to overestimate the binding energy of larger clusters. To address this effect we have repeated some simulations using diatomics-in-molecule potentials in which we have drastically decreased the value of this term in the *ab initio* Ba^+–He pair potentials. Even with this reduced attractive interaction we have found no evidence that the Ba^+ cation is ejected during the dynamics.

In addition to the potentials also the choice of the helium density functional plays an important role. The functional used in the present calculations has been constructed to be able to handle structured helium configurations such as those surrounding fairly attractive impurities like cations. The calculations yield very structured helium configurations corresponding to exciplexes, although the density is somewhat overestimated. Based on the good agreement between the calculated and experimentally observed absorption and emission spectra, however, we deem it unlikely that the choice of density functional is at the origin of the failure to reproduce the experimental results on the desolvation of excited Ba^+ ions.

In view of the above considerations regarding the accuracy of the calculations, it appears highly unlikely that excitation of a Ba^+ cations leads to its direct ejection from the helium droplet, either as bare ion or as a Ba^+He_n exciplex. The possibility that the cations are ejected from the droplets following radiative relaxation to the ^2D or ground state can be ruled out by the same arguments. This leaves non-radiative relaxation of the excited cations to the ^2D or the ^2S ground state as a possible explanation for the desolvation of the ions. Inspection of the Ba^+–He pair potentials and the Ba^+He_n exciplex potentials, Figs. 4 and 8, respectively, reveals that these states do not cross the ^2P states at energies accessible in the experiment. One therefore does not expect non-radiative relaxation to be an efficient process. Based on the same arguments one does not expect the relaxation from the $^2P_{3/2}$ to the $^2P_{1/2}$ state to be an efficient process. However, the emission spectra recorded for Ba^+ in bulk helium provide conclusive evidence that excitation of the $^2P_{3/2}$ is followed by a fast relaxation to the $^2P_{1/2}$ state. This could signify that non-adiabatic transitions which are not accounted for within the current theoretical model play a more important role than anticipated in the relaxation of excited atoms in helium droplets. Whether such transitions are important in the desolvation dynamics of excited Ba^+ cannot be answered for now and are worth a separate study.

To conclude, the present study indicates that elucidating the desolvation mechanism of excited Ba^+ ions will require additional experimental data, for example, on the state distribution of the desolvated Ba^+ cations, and an improved theoretical framework that, for example, includes non-adiabatic transitions between electronic states.[76]

ACKNOWLEDGMENTS

We would like to thank Francesco Ancilotto, Nadine Halberstadt, and Peter Moroshkin for useful discussions. This work has been performed under Grant Nos. FIS2014-52285-C2-1-P from DGI, Spain, 2014SGR401 from Generalitat de Catalunya, and 200021-146598 and 200020-162434 from the Swiss National Science Foundation. A.L. has been supported by the ME (Spain) FPI program, Grant No. BES-2012-057439. M.B. thanks the Université Fédérale Toulouse Midi-Pyrénées for financial support during the completion of this work throughout the "Chaires d'Attractivité 2014" Programme IMDYNHE.

APPENDIX: EXCITATION OF THE ^2D MANIFOLD

In this appendix we generalize the expressions of Subsection III C when the cation is excited to the ^2D manifold and give the essential details how the absorption spectrum has been calculated. To take advantage of the fast-Fourier techniques, we work in Cartesian coordinates. Our method is equivalent to that of Ref. 46 in which the PESs are expressed as a function of the spherical coordinates angles.

1. Pairwise sum approximation

The pair-interaction between an atom in a s-state and an atom in a d-state can be expressed in the basis $(|d_{xy}\rangle, |d_{yz}\rangle, |d_{z^2}\rangle, |d_{zx}\rangle, |d_{x^2-y^2}\rangle)$ as

$$\begin{aligned} U(r) &= \begin{pmatrix} V_\Delta(r) & 0 & 0 & 0 & 0 \\ 0 & V_\Pi(r) & 0 & 0 & 0 \\ 0 & 0 & V_\Sigma(r) & 0 & 0 \\ 0 & 0 & 0 & V_\Pi(r) & 0 \\ 0 & 0 & 0 & 0 & V_\Delta(r) \end{pmatrix} \\ &\equiv V_\Delta(r)\{|d_{x^2-y^2}\rangle\langle d_{x^2-y^2}| + |d_{xy}\rangle\langle d_{xy}|\} \\ &\quad + V_\Pi(r)\{|d_{yz}\rangle\langle d_{yz}| + |d_{zx}\rangle\langle d_{zx}|\} + V_\Sigma(r)|d_{z^2}\rangle\langle d_{z^2}| \\ &= V_\Delta(r)\mathbf{I} + \{V_\Pi(r) - V_\Delta(r)\}\{|d_{yz}\rangle\langle d_{yz}| + |d_{zx}\rangle\langle d_{zx}|\} \\ &\quad + \{V_\Sigma - V_\Delta(r)\}|d_{z^2}\rangle\langle d_{z^2}|, \end{aligned} \tag{A1}$$

where $V_\Delta(r)$, $V_\Pi(r)$, and $V_\Sigma(r)$ are the Ba^+–He pair potentials[41] and r is the distance between the cation and the He atom. For a system of N helium atoms, the total potential is approximated by the pairwise sum

$$\begin{aligned} U = \sum_{n=1}^{N} &\{V_\Delta(r_n)\mathbf{I} + [V_\Pi(r_n) - V_\Delta(r_n)]\, M_\Pi \\ &+ [V_\Sigma(r_n) - V_\Delta(r_n)]\, M_\Sigma\}, \end{aligned} \tag{A2}$$

where r_n is the distance between the nth helium atom and the impurity and

$$\begin{aligned} M_\Sigma &= \mathcal{R}_n |d_{z^2}\rangle\langle d_{z^2}| \mathcal{R}_n^{-1}, \\ M_\Pi &= \mathcal{R}_n \{|d_{yz}\rangle\langle d_{yz}| + |d_{zx}\rangle\langle d_{zx}|\} \mathcal{R}_n^{-1}, \end{aligned} \tag{A3}$$

being $\mathcal{R}_n$ the rotation matrix that transform the unity vector $\hat{\mathbf{z}}$ into $\hat{\mathbf{r}}_n$, i.e., the unity vector in the cation-nth He atom direction. The matrices M_Σ and M_Π are symmetric. We define

$$
\begin{aligned}
d_0 &\equiv (x^2+y^2+z^2)/r^2 = 1,\\
d_1 &\equiv d_{xy} = \sqrt{3}xy/r^2,\\
d_2 &\equiv d_{yz} = \sqrt{3}yz/r^2,\\
d_3 &\equiv d_{z^2} = \frac{1}{2}\left(3z^2-r^2\right)/r^2,\\
d_4 &\equiv d_{zx} = \sqrt{3}zx/r^2,\\
d_5 &\equiv d_{x^2-y^2} = \frac{1}{2}\sqrt{3}\left(x^2-y^2\right)/r^2,
\end{aligned}
\tag{A4}
$$

where to simplify the notation, (x, y, z) are the components of the $\hat{\mathbf{r}}_n$ vector that connects the impurity with the given nth He atom. In terms of the $d's$, the elements of the matrices above can be written as follows:

$$
\begin{aligned}
M_{\Sigma}^{i,j} &= d_i d_j,\\
M_{\Pi}^{1,1} &= \frac{1}{3}\left(4d_5^2+d_4^2+d_2^2\right),\\
M_{\Pi}^{1,2} &= -\frac{4}{3}d_1d_2+\frac{1}{\sqrt{3}}d_4d_0,\\
M_{\Pi}^{1,3} &= -\frac{2}{\sqrt{3}}d_2d_4,\\
M_{\Pi}^{1,4} &= -\frac{4}{3}d_1d_4+\frac{1}{\sqrt{3}}d_2d_0,\\
M_{\Pi}^{1,5} &= -\frac{4}{3}d_1d_5,\\
M_{\Pi}^{2,2} &= \frac{1}{3}\left(d_1^2+d_4^2\right)+\left(d_3+\frac{1}{\sqrt{3}}d_5\right)^2,\\
M_{\Pi}^{2,3} &= \frac{1}{\sqrt{3}}d_1d_4-d_2\left(d_3+\frac{1}{\sqrt{3}}d_5\right),\\
M_{\Pi}^{2,4} &= -\frac{4}{3}d_2d_4+\frac{1}{\sqrt{3}}d_1d_0,\\
M_{\Pi}^{2,5} &= -d_1d_4-\frac{1}{\sqrt{3}}d_2\left(d_3+\frac{1}{\sqrt{3}}d_5\right),\\
M_{\Pi}^{3,3} &= d_4^2+d_2^2,\\
M_{\Pi}^{3,4} &= \frac{1}{\sqrt{3}}d_1d_2-d_4\left(d_3-\frac{1}{\sqrt{3}}d_5\right),\\
M_{\Pi}^{3,5} &= \frac{1}{\sqrt{3}}\left(-d_4^2+d_2^2\right),\\
M_{\Pi}^{4,4} &= \frac{1}{3}\left(d_1^2+d_2^2\right)+\left(d_3-\frac{1}{\sqrt{3}}d_5\right)^2,\\
M_{\Pi}^{4,5} &= d_1d_2+\frac{1}{\sqrt{3}}d_4\left(d_3-\frac{1}{\sqrt{3}}d_5\right),\\
M_{\Pi}^{5,5} &= \frac{1}{3}\left(4d_1^2+d_4^2+d_2^2\right).
\end{aligned}
\tag{A5}
$$

The pairwise sum for U is transformed into a DFT expression by the substitution $\sum_n \to \int d\mathbf{r}'\rho(\mathbf{r}')$.[61]

2. Spin-orbit coupling

The SO interaction is semiempirically included assuming that the spin-orbit coupling is independent of the He-Ba^+ distance;[77] its strength is fixed to reproduce the spin-orbit splitting of bare Ba^+ in the 5d ^{2}D states, namely, 800.96 cm^{-1}.[62]

For the sake of completeness and future reference, we give the SO interaction in the basis used here, i.e., $|d_{xy},1/2\rangle$, $|d_{xy},-1/2\rangle$, $|d_{yz},1/2\rangle$, $|d_{yz},-1/2\rangle$, $|d_{z^2},1/2\rangle$, $|d_{z^2},-1/2\rangle$, $|d_{xz},1/2\rangle$, $|d_{xz},-1/2\rangle$, $|d_{x^2-y^2},1/2\rangle$, $|d_{x^2-y^2},-1/2\rangle$, where the spin component $s =\uparrow (m_s = 1/2)$, $\downarrow (m_s = -1/2)$ is explicitly noted. We have $V_{SO} = \frac{1}{2}A_{\ell s}M_{SO}$ with $A_{\ell s}$ being 2/5 of the mentioned SO splitting and M_{SO} is the 10×10 matrix

$$
\begin{pmatrix}
0 & 0 & 0 & 1 & 0 & 0 & 0 & -i & 2i & 0\\
0 & 0 & -1 & 0 & 0 & 0 & -i & 0 & 0 & -2i\\
0 & -1 & 0 & 0 & 0 & -i\sqrt{3} & i & 0 & 0 & -i\\
1 & 0 & 0 & 0 & -i\sqrt{3} & 0 & 0 & -i & -i & 0\\
0 & 0 & 0 & i\sqrt{3} & 0 & 0 & 0 & -\sqrt{3} & 0 & 0\\
0 & 0 & i\sqrt{3} & 0 & 0 & 0 & \sqrt{3} & 0 & 0 & 0\\
0 & i & -i & 0 & 0 & \sqrt{3} & 0 & 0 & 0 & -1\\
i & 0 & 0 & i & -\sqrt{3} & 0 & 0 & 0 & 1 & 0\\
-2i & 0 & 0 & i & 0 & 0 & 0 & 1 & 0 & 0\\
0 & 2i & i & 0 & 0 & 0 & -1 & 0 & 0 & 0
\end{pmatrix}.
$$

The electronic state Hamiltonian Eq. (8) is written as $\mathcal{H} = U + V_{SO}$ (the interaction U, Eq. (A1), is diagonal in spin and transformed into a 10×10 matrix to carry out the sum). As for ^{2}P states, diagonalization of $\mathcal{H}$ yields the five independent $V_\lambda(\mathbf{r})$ potentials for the ^{2}D manifold, each of them two-fold degenerate due to Kramer's theorem.[78,79] In the basis indicated above, the expression for the elements of the 10×10 matrix $\mathcal{V}(r)$ is

$$
\begin{aligned}
\mathcal{V}^{ijss'}(\mathbf{r}) = \Big\{&V_\Delta(\mathbf{r})\delta_{i,j} + \left[V_\Pi(\mathbf{r}) - V_\Delta(\mathbf{r})\right]M_\Pi^{ij}\\
&+ \left[V_\Sigma(\mathbf{r}) - V_\Delta(\mathbf{r})\right]M_\Sigma^{ij}\Big\}\,\delta_{s,s'}.
\end{aligned}
\tag{A6}
$$

3. ^{2}P→^{2}S and ^{2}P→^{2}D radiative transitions

Since the cation is described classically and the electron orbitals are not explicitly considered, the emission spectrum is calculated by a semiclassical approximation of the vibrational Franck-Condon factors of an instantaneous transition from a given relaxed ^{2}P state.[61]

The emission to the ^{2}S state is obtained as the vertical transition of the cation from a relaxed state characterized by a helium density $\rho_\lambda^{^2P}(\mathbf{r})$ associated with the $V_\lambda^{^2P}$ potential, namely,

$$
\Delta\omega_{^2S} = \int d\mathbf{r}\,\rho_\lambda^{^2P}(\mathbf{r})\left[V_\lambda^{^2P}(\mathbf{r}) - V_X(\mathbf{r})\right].
\tag{A7}
$$

The emission to the ^{2}D states is similarly obtained

$$
\Delta\omega_{^2D} = \int d\mathbf{r}\,\rho_\lambda^{^2P}(\mathbf{r})\left[V_\lambda^{^2P}(\mathbf{r}) - V^{^2D}(\mathbf{r})\right].
\tag{A8}
$$

Expressions (A7) and (A8) give the atomic shift for the emission to the ^{2}S or ^{2}D state, i.e., the peak position for a given configuration $\rho_\lambda^{^2P}(\mathbf{r})$ referenced to the emission energy of the free cation. The complete spectrum is obtained by the DF sampling method[80] that samples the DF density with the number of atoms in it, passing from a continuous to a discrete calculation of the transitions bearing a large similarity with the sampling method used within quantum Monte Carlo to obtain the spectrum,[78,81] there with walkers, here with "classical" atoms.

[1]R. L. Williams, Can. J. Phys. **35**, 134 (1957).
[2]D. R. Allum, P. V. E. McClintock, A. Phillips, and R. M. Bowley, Philos. Trans. R. Soc., A **284**, 179 (1977).
[3]V. Grau, M. Barranco, R. Mayol, and M. Pi, Phys. Rev. B **73**, 064502 (2006).
[4]H. J. Maris, J. Phys. Soc. Jpn. **77**, 111008 (2008).
[5]J. Poitrenaud and F. I. B. Williams, Phys. Rev. Lett. **32**, 1213 (1974).
[6]K. R. Atkins, Phys. Rev. **116**, 1339 (1959).
[7]B. Tabbert, H. Günther, and G. zu Putlitz, J. Low Temp. Phys. **109**, 653 (1997).
[8]M. W. Cole and R. A. Bachman, Phys. Rev. B **15**, 1388 (1977).
[9]B. Tabbert, M. Beau, H. Günther, W. Haussler, C. Honninger, K. Meyer, B. Plagemann, and G. zu Putlitz, Z. Phys. B **97**, 425 (1995).
[10]H. J. Reyher, H. Bauer, C. Huber, R. Mayer, A. Schafer, and A. Winnacker, Phys. Lett. A **115**, 238 (1986).
[11]H. Bauer, M. Beau, B. Friedl, C. Marchand, K. Miltner, and H. J. Reyher, Phys. Lett. A **146**, 134 (1990).
[12]A. Scheidemann, J. P. Toennies, and J. A. Northby, Phys. Rev. Lett. **64**, 1899 (1990).
[13]J. P. Toennies and A. F. Vilesov, Angew. Chem., Int. Ed. **43**, 2622 (2004).
[14]M. Y. Choi, G. E. Douberly, T. M. Falconer, W. K. Lewis, C. M. Lindsay, J. M. Merritt, P. L. Stiles, and R. E. Miller, Int. Rev. Phys. Chem. **25**, 15 (2006).
[15]F. Stienkemeier and K. K. Lehmann, J. Phys. B: At., Mol. Opt. Phys. **39**, R127 (2006).
[16]M. Hartmann, R. E. Miller, J. P. Toennies, and A. Vilesov, Phys. Rev. Lett. **75**, 1566 (1995).
[17]M. Hartmann, F. Mielke, J. P. Toennies, A. F. Vilesov, and G. Benedek, Phys. Rev. Lett. **76**, 4560 (1996).
[18]S. Grebenev, J. P. Toennies, and A. F. Vilesov, Science **279**, 2083 (1998).
[19]N. B. Brauer, S. Smolarek, E. Loginov, D. Mateo, A. Hernando, M. Pi, M. Barranco, W. J. Buma, and M. Drabbels, Phys. Rev. Lett. **111**, 153002 (2013).
[20]P. Claas, S. O. Mende, and F. Stienkemeier, Rev. Sci. Instrum. **74**, 4071 (2003).
[21]F. Bierau, P. Kupser, G. Meijer, and G. von Helden, Phys. Rev. Lett. **105**, 133402 (2010).
[22]L. Chen, J. Zhang, W. M. Freund, and W. Kong, J. Chem. Phys. **143**, 044310 (2015).
[23]X. H. Zhang and M. Drabbels, J. Phys. Chem. Lett. **5**, 3100 (2014).
[24]S. Smolarek, N. B. Brauer, W. J. Buma, and M. Drabbels, J. Am. Chem. Soc. **132**, 14086 (2010).
[25]X. H. Zhang, N. B. Brauer, G. Berden, A. M. Rijs, and M. Drabbels, J. Chem. Phys. **136**, 044305 (2012).
[26]A. I. G. Florez, D. S. Ahn, S. Gewinner, W. Schollkopf, and G. von Helden, Phys. Chem. Chem. Phys. **17**, 21902 (2015).
[27]J. M. Merritt, G. E. Douberly, and R. E. Miller, J. Chem. Phys. **121**, 1309 (2004).
[28]N. B. Brauer, S. Smolarek, X. H. Zhang, W. J. Buma, and M. Drabbels, J. Phys. Chem. Lett. **2**, 1563 (2011).
[29]F. Filsinger, D. S. Ahn, G. Meijer, and G. von Helden, Phys. Chem. Chem. Phys. **14**, 13370 (2012).
[30]X. Zhang and M. Drabbels, J. Chem. Phys. **137**, 051102 (2012).
[31]M. Barranco, R. Guardiola, E. S. Hernández, R. Mayol, J. Navarro, and M. Pi, J. Low Temp. Phys. **142**, 1 (2006).
[32]A. Leal, D. Mateo, A. Hernando, M. Pi, and M. Barranco, Phys. Chem. Chem. Phys. **16**, 23206 (2014).
[33]A. Leal, D. Mateo, A. Hernando, M. Pi, M. Barranco, A. Ponti, F. Cargnoni, and M. Drabbels, Phys. Rev. B **90**, 224518 (2014).
[34]D. Mateo, A. Leal, A. Hernando, M. Barranco, M. Pi, F. Cargnoni, M. Mella, X. Zhang, and M. Drabbels, J. Chem. Phys. **140**, 131101 (2014).
[35]A. Hernando, M. Barranco, M. Pi, E. Loginov, M. Langlet, and M. Drabbels, Phys. Chem. Chem. Phys. **14**, 3996 (2012).
[36]D. Mateo, A. Hernando, M. Barranco, E. Loginov, M. Drabbels, and M. Pi, Phys. Chem. Chem. Phys. **15**, 18388 (2013).
[37]J. von Vangerow, A. Stieg, F. Stienkemeier, M. Mudrich, A. Leal, D. Mateo, A. Hernando, M. Barranco, and M. Pi, J. Phys. Chem. A **118**, 6604 (2014).
[38]A. Braun and M. Drabbels, J. Chem. Phys. **127**, 114303 (2007).
[39]E. Loginov and M. Drabbels, J. Phys. Chem. A **111**, 7504 (2007).
[40]M. Lewerenz, B. Schilling, and J. P. Toennies, Chem. Phys. Lett. **206**, 381 (1993).
[41]M. Mella and F. Cargnoni, J. Phys. Chem. A **118**, 6473 (2014).
[42]I. S. Lim, H. Stoll, and P. Schwerdtfeger, J. Chem. Phys. **124**, 034107 (2006).
[43]F. Weigend and A. Baldes, J. Chem. Phys. **133**, 174102 (2010).
[44]F. Cargnoni and M. Mella, J. Phys. Chem. A **115**, 7141 (2011).
[45]M. W. Schmidt, K. K. Baldridge, J. A. Boatz, S. T. Elbert, M. S. Gordon, J. H. Jensen, S. Koseki, N. Matsunaga, K. A. Nguyen, S. Su, T. L. Windus, M. Dupuis, and J. A. Montgomery, J. Comput. Chem. **14**, 1347 (1993).
[46]F. Cargnoni, A. Ponti, and M. Mella, Phys. Chem. Chem. Phys. **15**, 18410 (2013).
[47]F. Stienkemeier, F. Meier, and H. O. Lutz, Eur. Phys. J. D **9**, 313 (1999).
[48]E. Loginov and M. Drabbels, J. Chem. Phys. **136**, 154302 (2012).
[49]A. Hernando, R. Mayol, M. Pi, M. Barranco, F. Ancilotto, O. Bünermann, and F. Stienkemeier, J. Phys. Chem. A **111**, 7303 (2007).
[50]F. Ancilotto, E. Cheng, M. W. Cole, and F. Toigo, Z. Phys. D **98**, 323 (1995).
[51]C. C. Lovallo and M. Klobukowski, J. Chem. Phys. **120**, 246 (2004).
[52]F. Dalfovo, A. Lastri, L. Pricaupenko, S. Stringari, and J. Treiner, Phys. Rev. B **52**, 1193 (1995).
[53]F. Ancilotto, M. Barranco, F. Caupin, R. Mayol, and M. Pi, Phys. Rev. B **72**, 214522 (2005).
[54]M. Frigo and S. G. Johnson, Proc. IEEE **93**, 216 (2005).
[55]A. Hernando, M. Barranco, R. Mayol, M. Pi, and F. Ancilotto, Phys. Rev. B **78**, 184515 (2008).
[56]M. Guilleumas, F. Garcias, M. Barranco, M. Pi, and E. Suraud, Z. Phys. D **26**, 385 (1993).
[57]L. Giacomazzi, F. Toigo, and F. Ancilotto, Phys. Rev. B **67**, 104501 (2003).
[58]L. Lehtovaara, T. Kiljunen, and J. Eloranta, J. Comput. Phys. **194**, 78 (2004).
[59]M. Weissbluth, *Atoms and Molecules* (Academic Press, New York, 1980).
[60]F. O. Ellison, J. Am. Chem. Soc. **85**, 3540 (1963).
[61]A. Hernando, M. Barranco, R. Mayol, M. Pi, and M. Krośnicki, Phys. Rev. B **77**, 024513 (2008).
[62]A. Kramida, Y. Ralchenko, and J. Reader, NIST ASD Team, NIST Atomic Spectra Database, version 5.0, National Institute of Standards and Technology, Gaithersburg, MD, 2012, available at: http://physics.nist.gov/asd.
[63]A. Ralston and H. S. Wilf, *Mathematical Methods for Digital Computers* (John Wiley and Sons, New York, 1960).
[64]D. Mateo, D. Jin, M. Barranco, and M. Pi, J. Chem. Phys. **134**, 044507 (2011).
[65]A. Pifrader, O. Allard, G. Auböck, C. Callegari, W. E. Ernst, R. Hubert, and F. Ancilotto, J. Chem. Phys. **133**, 164502 (2010).
[66]Y. Fukuyama, Y. Mortiwaki, and Y. Matsuo, Phys. Rev. A **69**, 042505 (2004).
[67]F. Ancilotto, P. B. Lerner, and M. W. Cole, J. Low Temp. Phys. **101**, 1123 (1995).
[68]D. Nettels, A. Hofer, P. Moroshkin, R. Müller-Siebert, S. Ulzega, and A. Weis, Phys. Rev. Lett. **94**, 063001 (2005).
[69]M. Zbiri and C. Daul, Phys. Lett. A **341**, 170 (2005).
[70]P. Moroshkin, A. Hofer, and A. Weis, Phys. Rep. **469**, 1 (2008).
[71]A. Hofer, P. Moroshkin, D. Nettels, S. Ulzega, and A. Weis, Phys. Rev. A **74**, 032509 (2006).
[72]R. A. Aziz and A. R. Janzen, Phys. Rev. Lett. **74**, 1586 (1995).
[73]P. Valiron and I. Mayer, Chem. Phys. Lett. **275**, 46 (1997).
[74]N. Issaoui, K. Abdessalem, H. Ghalla, S. J. Yaghmour, F. Calvo, and B. Ouija, J. Chem. Phys. **141**, 174316 (2014).
[75]P. Slavíček and M. Lewerenz, Phys. Chem. Chem. Phys. **12**, 1152 (2010).
[76]E. Loginov, A. Hernando, J. A. Beswick, N. Halberstadt, and M. Drabbels, J. Phys. Chem. A **119**, 6033 (2015).
[77]J. L. Persson, Q. Hui, Z. J. Jakubek, M. Nakamura, and M. Takami, Phys. Rev. Lett. **76**, 1501 (1996).
[78]A. Nakayama and K. Yamashita, J. Chem. Phys. **114**, 780 (2001).
[79]P. H. E. Meier and E. Bauer, *Group Theory* (North-Holland, Amsterdam, 1962).
[80]D. Mateo, A. Hernando, M. Barranco, R. Mayol, and M. Pi, Phys. Rev. B **83**, 174505 (2011).
[81]J. Navarro, D. Mateo, M. Barranco, and A. Sarsa, J. Chem. Phys. **136**, 054301 (2012).

Chapter 3

Excitation and ionization of alkali atoms

3.1 Desorption dynamics of heavy alkali metal atoms (Rb, Cs)

Resumen (Spanish)

En esta sección presentamos un estudio teórico y experimental sobre el proceso de eyección de átomos de cesio y rubidio desde de la superficie de nanogotas de helio tras la excitación de estos a los estados $6s$ y $7s$, respectivamente. Los cálculos revelan una respuesta compleja de la gota de helio a la perturbación producida por la excitación de las impurezas de Rb and Cs. En el proceso se han encontrado deformaciones locales de las nanogotas así como diferentes tipos de ondas de densidad que viajan a través de la gota a diferentes velocidades supersónicas.

La relación entre energía cinética y energía de excitación de la impureza calculada usando la DFT coincide notablemente con la determinada experimentalmente; dicha relación es la que se espera para una reacción de fotodisociación provocada por una interacción altamente repulsiva.

THE JOURNAL OF PHYSICAL CHEMISTRY A

Article

pubs.acs.org/JPCA

Desorption Dynamics of Heavy Alkali Metal Atoms (Rb, Cs) Off the Surface of Helium Nanodroplets

J. von Vangerow,[†] A. Sieg,[†] F. Stienkemeier,[†] M. Mudrich,*[,†] A. Leal,[‡] D. Mateo,[‡,§] A. Hernando,[∥] M. Barranco,[‡] and M. Pi[‡]

[†]Physikalisches Institut, Universität Freiburg, 79104 Freiburg, Germany

[‡]Departament ECM, Facultat de Física and IN[2]UB, Universitat de Barcelona, 08028 Barcelona, Spain

[§]Department of Chemistry and Biochemistry, California State University at Northridge, 18111 Nordhoff Street, Northridge, California 91330, United States

[∥]Laboratoire de Chimie Physique Moléculaire, Swiss Federal Institute of Technology Lausanne (EPFL), 1015 Lausanne, Switzerland

Supporting Information

ABSTRACT: We present a combined ion imaging and density functional theory study of the dynamics of the desorption process of rubidium and cesium atoms off the surface of helium nanodroplets upon excitation of the perturbed 6s and 7s states, respectively. Both experimental and theoretical results are well represented by the pseudodiatomic model for effective masses of the helium droplet in the desorption reaction of $m_{eff}/m_{He} \approx 10$ (Rb) and 13 (Cs). Deviations from this model are found for Rb excited to the 6p state. Photoelectron spectra indicate that the dopant−droplet interaction induces relaxation into low-lying electronic states of the desorbed atoms in the course of the ejection process.

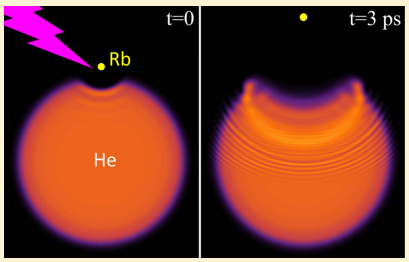

1. INTRODUCTION

Helium nanodroplets are fascinating many-body quantum systems which feature unique properties such as an extremely low internal temperature (0.38 K), nanoscopic superfluidity, and the ability to efficiently cool and aggregate embedded species (dopants). Therefore, He nanodroplets are widely used as nearly ideal spectroscopic matrices for high-resolution spectroscopy of isolated atoms, molecules, and clusters.[1−4]

Although most studies so far pertain to the structure and time-independent spectroscopy of doped He nanodroplets, the dynamics initiated by laser excitation or ionization of either the dopants or the droplets themselves moves into the focus of current research. A limited number of time-resolved experiments has been carried out with pure[5,6] and doped He droplets[7−14] using femtosecond pump−probe techniques. Likewise, theoretical models of pure and doped He nanodroplets have mostly been restricted to static structure and to excitation spectrum calculations.[4,15−18] Only recently, the development of time-dependent density functional theory (TDDFT) methods applicable to microscopic superfluids[19,20] has opened the way to a time-dependent description of doped He droplets in a range of sizes comparable to those used in the experiment.[21−24]

Dopants consisting of alkali (Ak) metal atoms or molecules are particularly interesting due to their weak attractive interaction with He droplets which results in their location in shallow dimple states at the droplet surface.[25−27] Upon electronic excitation, Ak atoms tend to desorb off the He droplets as a consequence of the repulsive interaction caused by the overlap of their extended electronic orbitals with the surrounding He.[28−30] The only known exceptions are Rb and Cs atoms excited to their lowest excited states.[31,32]

The dynamics of the desorption process of excited Ak atoms off the surface of He droplets has been recently studied in detail experimentally using the velocity-map imaging technique applied to Li, Na and Rb atoms, and theoretically using TDDFT for Li and Na.[22,33] The calculated He droplet response following the dopant excitation process from ns to $(n + 1)$s states was found to be quite complex, involving different types of density waves propagating through the droplet while the Ak dopant is ejected within a few picoseconds.[22] In spite of this, the experiments show that the kinetic energy of the desorbed atom depends linearly on the excitation energy of the dopant. This conspicuous result, also reproduced by the TDDFT simulations, gives further support to the pseudodiatomic model which has already been successfully applied to interpreting the absorption spectra as well as the ion velocity distributions.[33−37] According to this model, the dynamics of the excited $AkHe_N$ complex follows that of a dissociating diatomic molecule[38] where He_N plays the role of one single atom in this pseudodiatom. The part of the He droplet that effectively

Special Issue: Franco Gianturco Festschrift

Received: April 3, 2014
Revised: June 9, 2014
Published: June 9, 2014

dx.doi.org/10.1021/jp503308w | J. Phys. Chem. A 2014, 118, 6604−6614

interacts with the Ak atom was found to have an effective mass $m_{eff} \approx 15$ and $m_{eff} \approx 25$ amu for Li and Na, respectively.[22]

In the present work, we extend previous ion imaging and TDDFT studies to the heaviest stable Ak metal atoms Rb and Cs. We again find linear dependences of the ion kinetic energies upon laser photon energy in both experiment and theory. From these we infer the effective mass of the interacting He droplet for the desorption of Rb and Cs excited to the perturbed 6s and 7s states, respectively.

Although most excited Ak atoms interact repulsively with a He nanodroplet as a whole, some excited states experience local attraction with one or a few He atoms. Therefore, as the excited Ak atom is expelled from the droplet surface, a bound AkHe molecule or in some cases small $AkHe_n$, $n = 2, 3$ complexes can form.[7,29,39−42] These so-called "exciplexes" are characterized by having bound vibronic states as long as the complex is electronically excited. Upon spontaneous decay into the electronic ground state the exciplex decomposes. For such excited states of the Ak atom, the desorption dynamics may be expected to deviate from that described by the simple dissociating pseudodiatom model.

In our previous experiment on Rb-doped He droplets excited into the 6pΠ state, the ion kinetic energy distributions indicated that desorption of excited Rb atoms and RbHe exciplexes proceeds along the repulsive pseudodiatomic potential which correlates to the closest-lying excited 6p state of the free Rb atom. However, the photoelectron spectra clearly revealed that a large fraction of the desorbed Rb atoms have electronically relaxed into lower-lying levels. The photoelectron spectra contained components of the 6p state and of lower-lying levels (4d and $5p_{3/2}$).[33]

Previously, droplet-induced relaxation of excited Rb atoms was only observed within the $5p_{3/2,1/2}$ fine-structure doublet.[40] For Rb and Cs injected into bulk superfluid He fast relaxation of the lowest excited $p_{3/2}$ state into the $p_{1/2}$ and probably to the $s_{1/2}$ ground state was found to proceed within ∼30 ps.[43]

For Na-doped He nanodroplets, droplet-induced electronic relaxation was first observed only for higher-lying excitations with principal quantum numbers $n > 6$, where the dopant−droplet interaction induces significant mixing of electronic configurations.[36] In a more recent study, even for the 3d, 5s, and 4d states the authors found indications for droplet-induced decay into lower-lying levels.[44] Interestingly, the presence of the relaxation channels was also visible in the speed distributions of the desorbed atoms, which contained multiple components. High-lying Rydberg states were found to completely relax into levels $n \leq 7$. On the basis of these observations, the authors suggested that droplet-induced relaxation proceeds via level-crossings of the pseudodiatomic potential curves which occur while the local He droplet environment of the excited Na dopant dynamically rearranges. Efficient He droplet-induced electronic relaxation was also observed for barium[45] and for the transition metal atoms silver,[46] chromium[47] and copper,[48] which are submerged in the droplet interior.

Note, however, that the light Ak metals Li and Na were not found to electronically relax by droplet interactions when excited into the lowest excited s states (orbital angular momentum $l = 0$).[22] In contrast, in the present study on Rb and Cs atoms in their lowest excited s states we detect *exclusively* relaxed electronic levels in the photoelectron spectra. We discuss the apparent discrepancy between the ion and electron measurements in terms of the desorption dynamics and electron energetics.

2. EXPERIMENTAL SECTION

The experiments presented here are performed using the same setup as described previously.[33] In short, a continuous beam of He nanodroplets with a mean size ranging from 200 to 17 000 He atoms per droplet is generated by varying the temperature T_0 of a cryogenic nozzle with a diameter of 5 μm.[2,3] An adjacent vacuum chamber contains a vapor cell filled with bulk metallic Rb or Cs heated to 85 and 70 °C, respectively. In the detector chamber further downstream, the He droplet beam intersects a dye laser beam (Sirah Cobra, pulse length 10 ns, pulse energy 10 μJ, repetition rate 1 kHz) at right angles in the center of a velocity map imaging (VMI) spectrometer. The laser is linearly polarized along the direction of the He droplet beam, which is perpendicular to the symmetry axis of the VMI spectrometer. We record single events per image frame for which the coordinates are determined using the centroid method. Velocity-map photoelectron and photoion images are transformed into kinetic energy distributions using standard Abel inversion programs.[49,50]

3. THEORETICAL APPROACH

To model the absorption spectra as well as the dynamic response of the excited doped He droplets, we describe the doped He droplets within the density functional theory (DFT) framework.[4] The basic ingredients of our approach are described in detail in refs 22 and 23. Let us just recall that we have used the Born−Oppenheimer approximation to factorize the electronic and nuclear wave functions, the Franck−Condon approximation which assumes that the atomic nuclei do not change their positions or momenta during the electronic transition, and the diatomics-in-molecules approximation (pseudodiatomic model).[51]

We have first obtained the structure of the Rb−droplet and Cs−droplet complexes in the ground state. Throughout this work we have used the Orsay−Trento (OT) density functional,[52] neglecting the backflow term. The Rb−He and Cs−He ground state pair potentials V_X have been taken from ref 53. Due to the large mass of Rb and Cs compared to that of He, we describe them as classical particles in the dynamics and their effect in the statics is incorporated as an external field acting upon the droplet.[23] Accordingly, the energy of the system is written as

$$E[\rho] = \int \mathrm{d}\mathbf{r}\, \frac{\hbar^2}{2m_{He}} |\nabla \sqrt{\rho(\mathbf{r})}|^2 + \varepsilon_{He}[\rho(\mathbf{r})] + \int \mathrm{d}\mathbf{r}\, \rho(\mathbf{r}) V_X(|\mathbf{r}_{Ak} - \mathbf{r}|) \quad (1)$$

where ε_{He} is the OT potential energy density per unit volume, Ak represents either the Rb or Cs atom, and ρ is the He particle density. Upon variation, one obtains the Euler−Lagrange equation that has to be solved to determine the equilibrium density $\rho_0(\mathbf{r})$ of the droplet and the location of the dopant Rb or Cs atom $\mathbf{r}_{Ak_0}$.[35] Schematically,

$$\frac{\delta}{\delta\rho}\left(\frac{\hbar^2}{2m_{He}} |\nabla \sqrt{\rho}|^2 + \varepsilon_{He}\right) + V_X = \mu \quad (2)$$

where μ is the chemical potential of the He droplet that throughout this paper is made of $N = 1000$ atoms. To explore

dx.doi.org/10.1021/jp503308w | J. Phys. Chem. A 2014, 118, 6604−6614

other locations of the Ak atom around its equilibrium position in the surface dimple, we have minimized the energy submitted to a constraint.[23] This will be useful for determining the mean kinetic energy of the ejected Ak atom as a function of the excess excitation energy.

Equation 2 has been solved in Cartesian coordinates using a spatial grid of 0.4 Å and a 200 × 200 × 250 points mesh. The derivatives have been calculated with 13-point formulas. Extensive use of fast-Fourier techniques has been made to efficiently calculate the energy density and dopant−droplet interaction potentials.[22,23]

The dynamics is triggered by the sudden substitution of the Ak−He ground state pair potential by the excited one. Within TDDFT, we represent the He droplet by a complex effective wave function $\Psi_{He}(\mathbf{r},t)$ such that $\rho(\mathbf{r},t) = |\Psi_{He}(\mathbf{r},t)|^2$. The position of the Ak atom $\mathbf{r}_{Ak}(t)$ obeys Newton's equation. For excitations involving two s states, the evolution equations derived in ref 23 adopt a simple form, namely

$$i\hbar\frac{\partial}{\partial t}\Psi_{He} = \left[-\frac{\hbar^2}{2m_{He}}\nabla^2 + \frac{\delta\varepsilon_{He}}{\delta\rho(\mathbf{r})} + V_{ns}(\mathbf{r}-\mathbf{r}_{Ak})\right]\Psi_{He}$$
$$m_{Ak}\ddot{\mathbf{r}}_{Ak} = -\nabla_{\mathbf{r}_{Ak}}\left[\int d\mathbf{r}\,\rho(\mathbf{r})V_{ns}(\mathbf{r}-\mathbf{r}_{Ak})\right] \quad (3)$$

In the above equations, V_{ns} with $n = 6(7)$ is the 6s(7s) excited Rb(Cs)−He pair potential.[54] The initial configuration to solve eqs 3 is the static dopant−droplet configuration, either at equilibrium or with the dopant sitting in another position around the surface dimple, $\Psi(\mathbf{r},t{=}0) = (\rho_0(\mathbf{r}))^{1/2}$, $\mathbf{r}_{Ak}(t{=}0) = \mathbf{r}_{Ak0}$. The initial velocity of the Ak dopant is set to zero.

Equations 3 have been solved using the same grid as for the static problem and a time step of 0.5 fs. We have used a predictor-corrector method[55] fed by a few time steps obtained by a fourth-order Runge−Kutta algorithm.

PHOTOIONS

In this work we focus on the $ns\Sigma \rightarrow (n+1)s\Sigma$ transitions of the $RbHe_N$ and $CsHe_N$ pseudodiatoms, where $n = 5, 6$ denotes the principal quantum number of the atomic ground states of Rb and Cs, respectively. The excitation scheme is represented in Figure 1 for Rb, where we use the pseudodiatomic potential energy curves computed by Callegari and Ancilotto.[30] The ionic potential is obtained by integration of the Rb^+−He pair potential[56] over the He density distribution corresponding to the Rb ground state configuration, which we assume to be frozen.[35] Because the Ak−He interaction in the excited $(n+1)s\Sigma$ states is purely repulsive, the excited Ak atoms detach from the He droplets as neat atoms. Subsequent ionization by the absorption of a second photon from the same nanosecond laser pulse yields atomic ions which we detect with the VMI spectrometer.

Using these potentials,[30] we have obtained the Rb and Cs absorption spectra by calculating wave functions and Franck−Condon factors for the pseudodiatomic transitions using R. LeRoy's program BCONT 2.2.[57] The results are depicted in Figure 2. We have also calculated the Rb $5s\Sigma \rightarrow 6s\Sigma$ and Cs $6s\Sigma \rightarrow 7s\Sigma$ absorption band contours by employing the atomic-like DFT sampling method described in refs 21 and 58 shown in that figure as blue lines. The vertical dashed lines indicate the atomic transitions.

Both experimental and theoretical absorption spectra are characterized by broad bands that are blue-shifted with respect to the free atomic transitions. The blue shift of the transitions

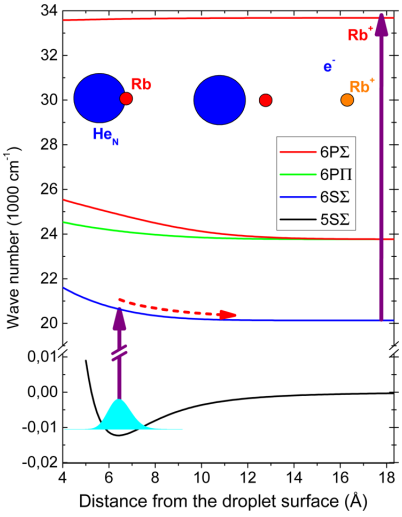

Figure 1. Sketch of the excitation and ionization scheme of Rb attached to He nanodroplets. Upon excitation of the $RbHe_N$ complex to a repulsive pseudodiatomic potential,[30] the Rb atom departs from the droplet surface and is ionized by a second photon from the same laser pulse.

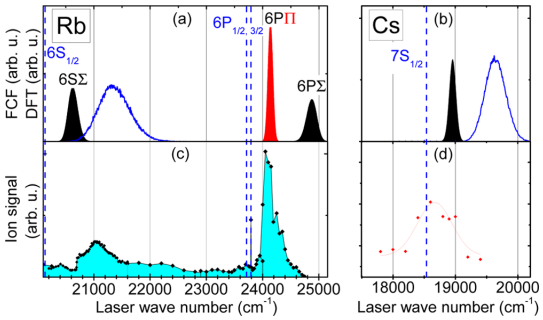

Figure 2. Simulated (a, b) and measured (c, d) photoionization spectra of He nanodroplets doped with Rb and Cs. The filled curves in (a, b) show Franck−Condon calculations based on Rb−He_N and Cs−He_N pseudodiatomic potentials;[30] the blue lines show the Rb $6s\Sigma$ (a) and Cs $7s\Sigma$ (b) absorption profiles obtained from the present atomic-like DFT sampling method.

of Rb attached to He droplets results from the fact that all excited pseudodiatomic potentials are repulsive whereas the ground state is slightly attractive (Figure 1). The widths of the absorption contours reflect the width of the ground state wave function which is mapped onto the excited repulsive potential upon excitation. Although the calculated Franck−Condon profile of the Rb $6p\Pi$ transition and the experimental spectrum is satisfactory, the Franck−Condon profile of the $6s\Sigma$ transition is slightly red-shifted with respect to the experimental contour, whereas the DFT result is blue-shifted (Figure 2a,c). The photoionization spectrum of Cs (Figure 2d) features a maximum in the range ∼18 300−19 000 cm^{-1} associated with the $7s\Sigma$ transition. The corresponding DFT calculation (Figure 2b) yields a peak centered at 19 635 cm^{-1}, which is again significantly blue-shifted. The DFT calculation thus overestimates the atomic shift, being unclear which part of the

dx.doi.org/10.1021/jp503308w | J. Phys. Chem. A 2014, 118, 6604−6614

disagreement has to be attributed to deficiencies of the model and which to inaccuracies of the excited Ak−He pair potentials we are using.[54]

Note that a broad Rb^+ ion signal level, which features a step around 20 700 cm^{-1} is measured around the 6sΣ feature, as previously observed in photoion[33] and laser-induced fluorescence spectra[59] around the 6pΠ transition. This contribution may be due to photoionization of Rb_2 dimers which fragment into Rb^+. In particular, at wavenumbers below 20 700 and above 21 000 cm^{-1} we observe significant Rb_2^+ signals in the time-of-flight mass spectrum which could be due to resonance-enhanced ionization via the $2^3\Sigma_u$ and via the $2^1\Sigma_u$, $2^1\Pi_u$, or $3^3\Pi_g$ states of Rb_2, respectively.[60]

The dynamics of the laser-induced desorption process of Rb and Cs atoms is studied by recording velocity-map ion images. Parts a and b of Figure 3 display the raw and inverted Rb^+ ion images taken upon excitation to the 6sΣ state of the $RbHe_N$ complex at the laser wavenumber $\bar{\nu}$ = 20 800 cm^{-1}. The image features a circular intensity distribution with a pronounced anisotropy of the angular dependence. The intensity maxima are directed along the polarization axis of the laser (yellow arrow), as expected for the parallel 5sΣ → 6sΣ transition.[22,33] The velocity-map ion images of Cs recorded at the 6sΣ → 7sΣ transition around $\bar{\nu}$ = 18 700 cm^{-1} closely resemble those for Rb. In the measurements of Rb excited to the 5pΠ state around $\bar{\nu}$ = 24 100 cm^{-1}, the opposite anisotropy is observed as expected for a perpendicular Σ → Π transition in the frame of the pseudodiatomic model.[33]

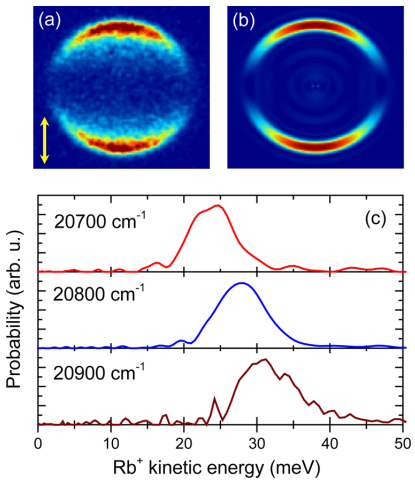

Figure 3. Top: raw (a) and inverse Abel transformed (b) velocity-map Rb^+ ion images recorded when Rb atoms attached to He nanodroplets were excited on the transition 5sΣ → 6sΣ at the laser wavenumber $\bar{\nu}$ = 20 800 cm^{-1}. The laser polarization direction is indicated by the vertical arrow. Bottom: Rb^+ ion kinetic energy distributions inferred from ion images recorded at the indicated laser wavenumbers.

From these images we infer the ion kinetic energy distributions (KED) by applying inverse Abel transformation and angular integration. Typical examples of such KED for excitation around the maximum of the 6sΣ band are depicted in Figure 3. Similarly to the previous measurements with Li and Na,[22] the KED consist of well-resolved maxima of widths ∼70 meV that shift toward higher kinetic energies as the photon energy increases.

Figure 4 presents a compilation of the results of the analysis of the ion images recorded around the Rb 6sΣ band as a function of the laser wavenumber. The total Rb^+ ion counts (black squares in Figure 4a) reproduce the photoionization spectrum (red diamonds) with some systematic deviation at wavenumbers >20 850 cm^{-1} of unknown origin. The mean values of the KED inferred from the images, shown in Figure 4b, nearly linearly increases with laser wavenumber. In addition, Figure 4c shows the variation of the anisotropy parameter β_2 within a 4 sigma range around the KED intensity maximum inferred from the angular distributions $I(\theta)$ by fitting to the general expression for the probability distribution of one-photon transitions $I(\theta) \propto 1 + \beta_2 P_2(\cos\theta)$.[61] For laser wavenumbers close to the maximum of the 6sΣ absorption band (20 700−21 100 cm^{-1}) we obtain β = 1.9(3). Within the experimental error this is consistent with the value β_2 = 2 expected for excitation of an ideal diatomic molecule at a parallel Σ−Σ transition. In this case the angular distribution of dissociation products takes the form $I(\theta) \propto \cos^2\theta$.

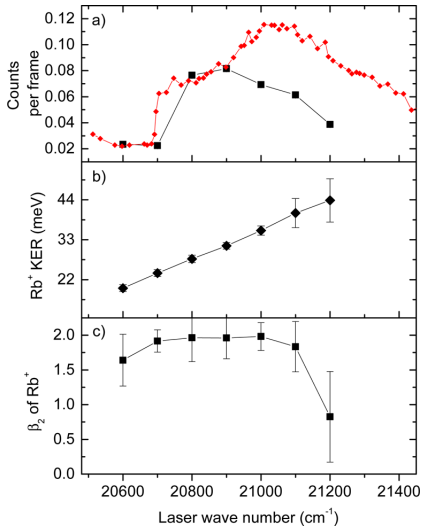

Figure 4. (a) Total Rb^+ ion counts and time-of-flight peak intensity (red), (b) Rb^+ mean kinetic energies, and (c) anisotropy parameters β_2 inferred from ion images recorded at various laser wavelengths around the maximum of the Rb 6sΣ absorption band.

This result nicely confirms the validity of the pseudodiatomic model and the assignment of the spectral band to the parallel 5sΣ → 6sΣ transition. However, in the wings of the absorption peak we find the anisotropy of the angular ion distribution to be significantly reduced. This may be due to the contribution of fragment ions from Rb_2 dimers which are present to a small extent in the droplet beam. Besides, it is conceivable that dynamic deformations of the local He droplet environment during the departure of the Rb atom induce perturbations of the electronic configuration of the excited Rb atom which are not accounted for in the pseudodiatomic picture.

To obtain more detailed insight into this process, we have simulated the ejection of a Rb atom from the nominal 6s state and of a Cs atom from the nominal 7s state using TDDFT

dx.doi.org/10.1021/jp503308w | J. Phys. Chem. A 2014, 118, 6604−6614

calculations. The velocities and positions as a function of time for Rb and Cs ejected from the equilibrium position at the surface dimple are shown in Figure 5. It can be seen that the Cs

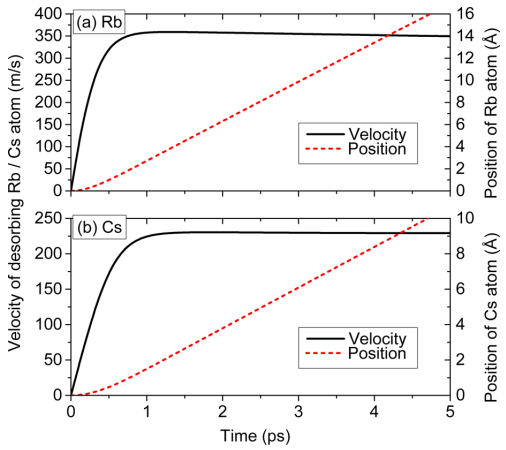

Figure 5. Velocity (solid line, left scale) and displacement from its equilibrium location at the surface dimple (dashed line, right scale) of the desorbing Rb (a) and Cs (b) atoms as a function of time after excitation of the 6sΣ state.

atom reaches an asymptotic velocity of ∼230 m/s after a time evolution of ∼1.25 ps. By this time, the Cs atom is ∼2 Å away from its original equilibrium position at the dimple. The corresponding values for the Rb atom are ∼350 m/s, ∼1 ps, and ∼2.7 Å, respectively. In both cases, the recoil velocity of the He droplet is small, on the order of 7.5 m/s. The different evolution of positions and velocities for Rb and Cs is mainly due to the different masses of the two species. The fact that both curves are smooth and monotonously increasing with time implies that the desorption proceeds impulsively. Thus, although in the first stages of the dynamics surface vibrations and highly nonlinear density waves are excited in the droplet which take a large part of the energy deposited in the system upon photo excitation, the desorption dynamics is rather insensitive to them.

Detailed information about the kinematics of the desorption process can be gained from the kinetic energies of the desorbing dopants as a function of the excess excitation energy (difference between photon energy and internal energy of the free Rb or Cs atom in the 5s and 6s states).[22] The results are shown in Figure 6 and compared to the experimental mean kinetic energies. The calculated points have been obtained by starting the dynamic simulation from different positions of the Ak obtained by a constrained minimization of the total energy of the Ak−He_N complex as indicated in section 3.

For both Rb and Cs dopants, the kinetic energy displays a linear dependence on the excess excitation energy. This dependence indicates that in spite of its apparent complexity, the ejection process is well represented by the pseudodiatomic model.[22,38] Indeed, imposing energy and linear momentum conservation in the instantaneous ejection of the Ak atom from the droplet one obtains

$$E_{kin} = \eta(\hbar\omega - \hbar\omega_0) \quad (4)$$

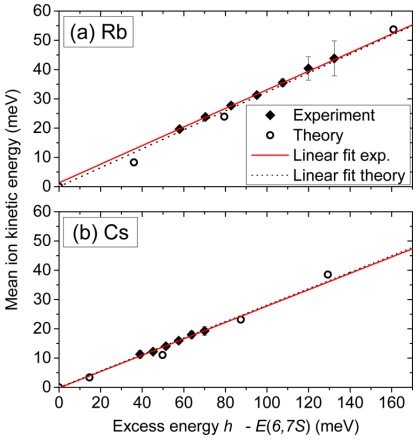

Figure 6. Mean kinetic energies of desorbed Rb (a) and Cs (b) atoms upon excitation to the 6sΣ and 7sΣ states, respectively. Straight lines: linear fits to the theoretical and experimental data.

Here, ω denotes the laser frequency and ω_0 is the atomic transition frequency. Within this model, the value of the slope η is related to the mass m_{eff} of the part of the He droplet that effectively interacts with the Ak atom[22] by

$$\eta = \frac{m_{eff}}{m_{eff} + m_{Ak}} \Rightarrow m_{eff} = \frac{\eta}{1-\eta} m_{Ak} \quad (5)$$

By fitting the experimental and simulation data to the expression eq 4, one obtains a theoretical value $m_{eff} \sim 40.7$ amu (10.2 He atoms) for Rb as compared with the experimental value of 39.6 amu (9.9 He atoms). The corresponding values for Cs are $m_{eff} \sim 52.0$ amu (13.0 He atoms) from theory and 51.6 amu (12.9 He atoms) from experiment. The results for Rb and Cs, together with those obtained for Li and Na in ref 22, are collected in Table 1 and plotted in Figure 7. One observes an increase of m_{eff} with the mass of the Ak atom, as indicated by eq 5, although the prefactor $\eta/(1-\eta)$ has the opposite behavior.

Table 1. Characteristics of the Experimental and Theoretical Kinetic Energy Distributions of the Desorbed Alkali Atoms (Details in Text, All Masses in amu)

Ak	m_{Ak} (exp)	η (exp)	η (th)	m_{eff} (exp)	m_{eff} (th)	$\langle r_e \rangle$ (Å)	m_{eff} (overlap)
Li	6.94	0.687	0.756	15.2	21.5	5.35	17.0
Na	23.0	0.516	0.583	24.6	32.2	5.55	22.1
Rb	85.5	0.327	0.324	41.9	41.0	6.54	41.5
Cs	132.9	0.281	0.273	51.8	50.5	6.78	53.8

The conspicuous dependence of the effective mass of the helium droplet m_{eff} on the Ak dopant mass m_{Ak} is expected to be mainly determined by two effects. On the one hand, the geometric structure of the excited Ak−droplet system is different for each species due to slight variations of the ground state equilibrium configuration[62] (radius of the surface dimple, distance of the Ak atom from the surface) as well as due to a varying radius of the excited Ak atom orbital r_e. On the other hand, the kinematics of the dissociation process induces an Ak mass dependence, irrespective of the differing geometric initial conditions.

dx.doi.org/10.1021/jp503308w | J. Phys. Chem. A 2014, 118, 6604−6614

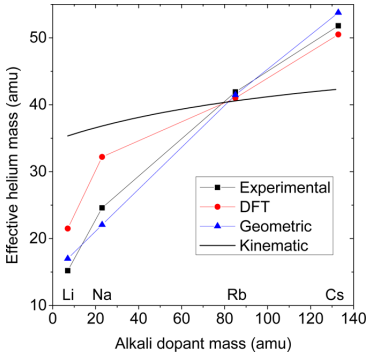

Figure 7. Experimental, theoretical, and estimated values of the effective mass of the He droplet in the desorption process of various alkali species excited to their first excited s states.

The geometric effect is estimated by computing the spatial overlap of the electron orbit of the excited Ak atom with the adjacent He atoms of the dimple. On the basis of the He dimple parameters specified in ref 62 and on values for the mean orbital radius $\langle r_e \rangle$, we calculate the number of He atoms in the overlap volume V_{eff} of the excited Ak orbit and the He dimple surface, $N_{He,eff} = V_{eff}\,\rho_{eff}$. Here, ρ_{eff} is taken as half the bulk value $\rho_{He} = 0.0218$ Å^{-3}, which roughly matches the average He density within the overlap volume due to its location at the dimple surface where the density smoothly falls off.[62] The mean orbital radius is approximated by[44,63]

$$\langle r_e \rangle = \frac{3}{2} a_0 (n - \delta_l)^2 \tag{6}$$

where a_0 is the Bohr radius and δ_l is the quantum defect of the Ak excited state. The corresponding values of $\langle r_e \rangle$ and $m_{eff} = m_{He} N_{He,eff}$ are added to Table 1 and to Figure 7.

The kinematic effect of the varying mass of the desorbing Ak atom is probed by solving the classical equations of motion of the Ak atom being repelled off a linear chain of effective, mutually noninteracting He atoms, each containing the mass of 7 He atoms, which roughly equals the number of He atoms in the first surface layer next to the Ak dopant.[62] The initial spacing between the He "layers" is taken as the average distance between He atoms in the droplets, 3.6 Å.[64] The distance between the Ak atom and the fist He "layer" is held fixed at 5.5 Å and the same Ak−He interaction potential $V_{Ak-He}(d) = 0.2 \exp(-d/3-1)$ (in atomic units) is used for all Ak species. The trajectories of the Ak atoms closely follow those shown in Figure 5 and the trajectories of the He layers show that mostly the first He layer participates in the desorption dynamics. Accordingly, the effective mass of the He droplet (approximated by the linear chain of atoms with the mass of the He layers) only slightly exceeds the mass of the first He layer, 28 amu; see the solid line in Figure 7.

Although the He effective mass in this simple kinematic model matches the experimental and DFT values for Rb, the variation as a function of Ak dopant mass is not sufficiently well reproduced (Figure 7). The simple estimate based on the geometric Ak−He orbital overlap, however, shows a strong variation of the effective mass in surprisingly good agreement with the experimental values. We therefore conclude that the difference in the number of interacting He atoms for the different Ak species is likely related to the difference in the dimple structure and excited electron orbit rather than to the kinematics of the desorption process.

The detailed picture of the dynamics of the He droplet upon excitation of the Ak atom is obtained from the DFT calculations. Figure 8 shows the evolution of the $CsHe_{1000}$

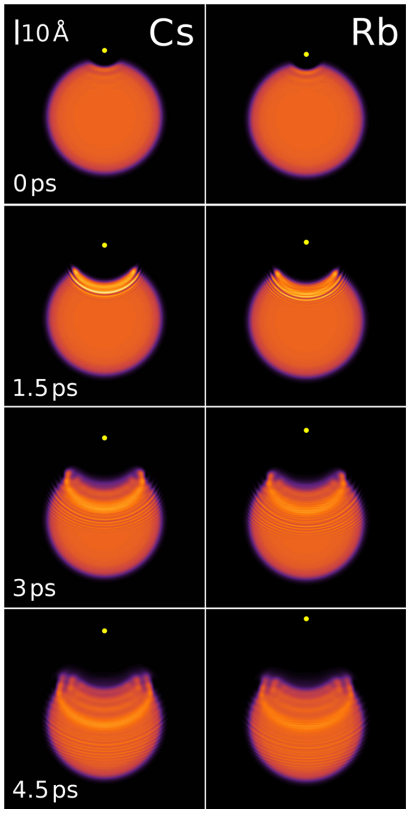

Figure 8. Evolution of the He density distributions of the $CsHe_{1000}$ (left column) and $RbHe_{1000}$ (right column) systems after excitation to their $(n + 1)s\Sigma$ states (multimedia view).

and $RbHe_{1000}$ complexes after the Ak atom has been excited. It can be seen the dramatic changes in the droplet density caused by the excitation and subsequent ejection of the dopant.

Figure 9 shows the evolution of the He cross-sectional density profiles of a He_{1000} droplet doped with a Rb and a Cs atom for the first 5 ps. Initially, the droplet extends along the z symmetry axis from about 0 to 44 Å, and the Ak atom is located in a dimple at the droplet surface (near $z = 0$). Excitation of the Ak atom to the $(n + 1)$s state causes the dimple first to deepen due to the highly repulsive Ak−He interaction in the $(n + 1)s\Sigma$ state. The associated compression of the He droplet lasts up to ~1 ps, as shown in the figure. Following this compression, the He surface bounces back and the dimple starts being filled. The more distant part of the droplet (near $z = 42$ Å) is unperturbed and at rest, indicating that during these first ps the energy deposited in the droplet goes to its internal excitation and not to its center-of-mass motion.

Figures 8 and 9 reveal that the excitation of the Cs and Rb atoms launches highly nonlinear density waves into the droplet.

dx.doi.org/10.1021/jp503308w | J. Phys. Chem. A 2014, 118, 6604−6614

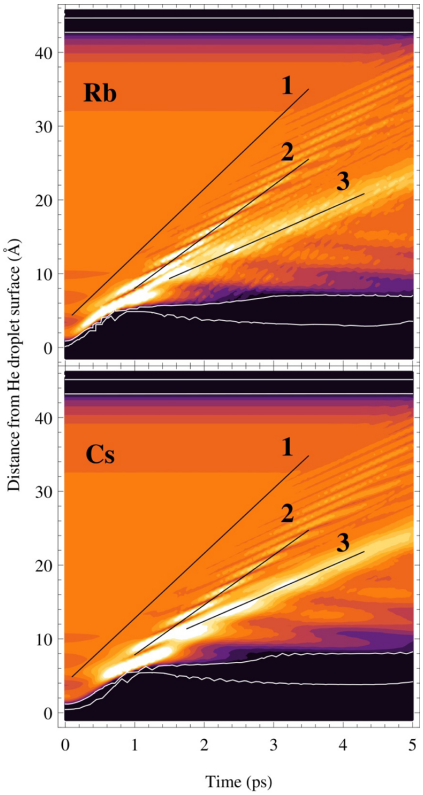

Figure 9. Evolution of the He density profile of the $AkHe_{1000}$ system along the symmetry axis. Three supersonic wave fronts are identified and labeled by 1−3. Equidensity lines corresponding to 0.5 and 0.1 times the He saturation density, 0.0218 $Å^{-3}$, representing the surface region of the droplet, are shown in white.

In the case of Rb, the first perturbation front, labeled as 1, moves at ∼900 m/s. This perturbation generates carrier waves with a phase velocity of ∼430 m/s, modulated by supersonic envelope fronts with growing intensity. The ones with highest intensity, labeled as 2, have a group velocity of ∼700 m/s. Next, a high-intensity wave appears traveling at ∼410 m/s (labeled as 3), which generates secondary waves propagating backward. In the case of Cs, the velocities of the fronts are 880, 675, and 410 m/s, respectively. A similar behavior was found in ref 22 for Na and Li atoms.

As an extension of our previous ion imaging measurements at the Rb 6pΠ band,[33] we analyze here the mean ion kinetic energy as a function of the excess energy. Because in the 6pΠ configuration the Rb−He pair potential along the internuclear axis is attractive,[54] RbHe exciplexes are formed with roughly 40% relative abundance.[33] Therefore, we record ion images for Rb^+ and $RbHe^+$ ions separately and extract the mean ion kinetic energies for each of the two species.

Figure 10 shows that the data points lie on a straight line that surprisingly intercepts the abscissa at a finite value of the excess energy of about −22 meV. Using eq 5, from the slope of the line η one obtains m_{eff} = 46.0 (11.5 He atoms) for Rb, and m_{eff} = 53.2 amu (13.3 He atoms) for RbHe, slightly larger than the corresponding value for the 6sΣ state.

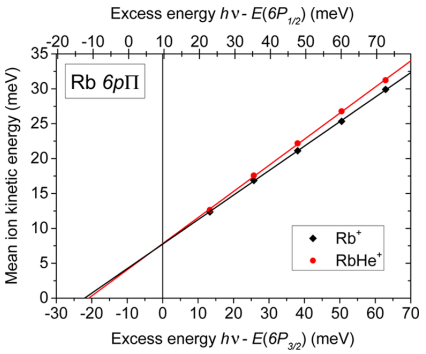

Figure 10. Experimental mean kinetic energies of Rb atoms and of RbHe exciplexes ejected out of He droplets upon excitation of the 6pΠ state of the $RbHe_N$ complex. The lines are linear fits to the data.

The fact that the extrapolation of the 6pΠ experimental data to zero kinetic energy yields a finite energy shift, at variance with the extrapolation of the 6sΣ data, discloses an intrinsic limitation of the method used to analyze the results. The pseudodiatomic approximation, even if appropriate for the description of a direct dissociation via a purely repulsive state, does not account for other effects which are present in the dissociation kinematics of the $(n + 1)$p excitation. In the case of the 6pΠ state of Rb, the dopant−He interaction contains both repulsive and attractive contributions, the latter inducing the formation of exciplexes. It is conceivable that the binding energy of the RbHe exciplex may be converted into additional translational energy upon desorption of RbHe. This interpretation has recently been invoked to rationalize the negative excess energy offset measured for NaHe exciplexes formed upon excitation of Na into the droplet-perturbed 3d state.[44] The binding energy of RbHe in the 6pΠ state amounts to about 8 meV, which does not account for the observed energy shift alone. Additional internal energy may be released into translational motion of the desorbing Rb by droplet-induced relaxation of population from the upper $6p_{3/2}$ into the lower $6p_{1/2}$ spin−orbit state of Rb. In that case, the excess energy axis would be downshifted as represented by the horizontal top scale of Figure 10 provided the droplet effective mass is the same (m_{eff} = 46.0 amu) for this additional acceleration of the Rb atom due to spin−orbit relaxation. However, the atomic spin−orbit splitting (9.6 meV) does not fully account for the observed shift. Only the assumption that both spin−orbit and binding energy of the RbHe exciplex are fully converted into translational energy would explain the energy offset for RbHe. The nearly coinciding kinetic energies of Rb and RbHe may indicate that Rb^+ ions are actually produced by dissociative ionization of RbHe, the latter being the dominant product of the desorption reaction.

Thus, it seems that the pseudodiatomic model no longer strictly applies when the internal degrees of freedom of the constituent atom are involved in the dynamics. Note that for the case of the desorption of sodium (Na) atoms excited to the 3p state deviations from the pseudodiatomic model were also observed.[65] However, in contrast to the Rb case discussed here, a positive value for the abscissa intercept was found. TDDFT studies of Ak atoms ejected from the $(n + 1)$p excited states could help elucidate this open issue, but improved Ak−He pair potentials have to be previously obtained.

PHOTOELECTRONS

Complementary information about the dynamics following laser excitation of Ak atoms attached to He nanodroplets is obtained from imaging photoelectrons. In the experiment, velocity-map photoelectron images are obtained by simply reversing the polarity of the voltages applied to the repeller and extractor electrodes.[33] A typical raw and inverse Abel transformed image recorded at the laser wavenumber 21 400 cm^{-1} is depicted in the upper and lower half of Figure 11a,

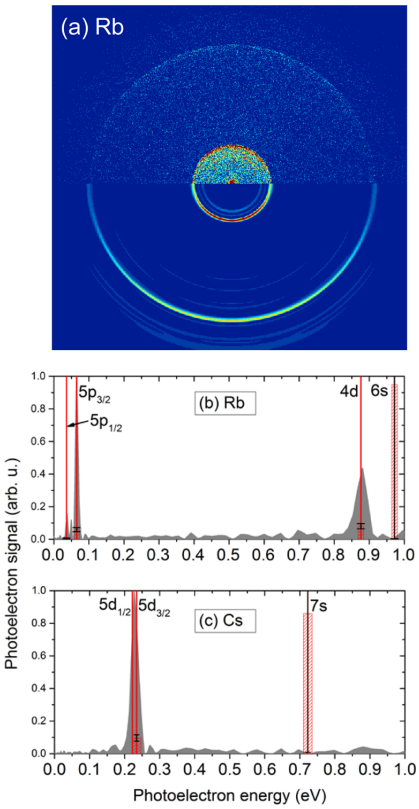

Figure 11. (a) Raw (upper half) and Abel inverted photoelectron image (lower half) of Rb^+ ions recorded with Rb-doped He nanodroplets excited into the 6sΣ state at the laser wavenumber ν = 21 400 cm^{-1}. (b) and (c) Photoelectron spectra of Rb and Cs inferred from images recorded at the laser wavenumbers 21 400 cm^{-1} and 18 700 cm^{-1}, respectively. The vertical bars represent the relative populations in the respective atomic states.

respectively. The image clearly contains three separated ring structures, indicating that ionization occurs out of three Rb atomic orbitals. The faint ring structure between the two inner rings in the lower half of Figure 11a is an artifact of the inverse Abel tranformation caused by the limited statistics. As for the ion images, we again convert the electron images into angular distributions and electron kinetic energy spectra. The latter are shown in Figure 11b for Rb and in Figure 11c for Cs.

Surprisingly, all the photoelectron spectra recorded within the Rb 6sΣ band reveal contributions of the Rb $5p_{1/2}$, $5p_{3/2}$, and 4d atomic levels. No electron signal associated with the 6s state is detected within the noise level, although the 6s state is the dominant atomic component of the originally excited 6sΣ state of the $RbHe_N$ complex.[30] The same holds for Cs excited to the 7sΣ state. Only one peak is present in the spectrum due to ionization out of the Cs 5d state. The 6p states, which are probably populated as in the Rb case, are not detected because of insufficient photon energy for one-photon ionization of the 6p states.

This result is at odds with the previous measurements of Li and Na excited to $(n + 1)$s states and to our previous photoelectron spectra recorded at the Rb 6pΠ band where on resonance the dominant photoelectron signals came from the correlating atomic 6p state. The lower lying 4d and $5p_{3/2, 1/2}$ states became particularly apparent for off-resonant excitation. In the present case, however, the absence of the Rb 6s and Cs 7s photoelectron signals is probably due to the particularly small photoionization cross sections of about 0.01 Mb, which result from Cooper minima close to the laser wavenumbers used in the experiment.[66,67] For comparison, the detected states have photoionization cross sections >10 Mb.[67,68]

In the case of Na attached to He nanodroplets, the appearance of lower-lying atomic states was attributed to the short radiative lifetime of the excited level as compared to the laser pulse length.[36] In the Rb and Cs cases, however, as for the Rb 6pΠ state previously studied,[33] the lifetimes of the free Rb and Cs atoms in the 6s and 7s states (~50 ns[67,69]) by far exceed the laser pulse length (9 ns). Moreover, the appearance of the 4d state of Rb and of the 5d state of Cs cannot be explained by spontaneous radiative decay due to selection rules. Merely the Rb 5p photoelectron signal may contain a contribution from radiative decay. Therefore, we attribute the population of lower-lying electronic states to He droplet-induced relaxation. Whether this relaxation mechanism is predominantly non-radiative or whether the dopant−droplet interaction induces fast radiative decay even at nominally forbidden transitions cannot be determined from these measurements.

The vertical bars in Figure 11b,c depict the relative populations of the detected states as inferred from the peak integrals weighted by the photoionization cross sections. The corresponding values of the undetected Rb 6s and Cs 7s states reflect the noise level and can only be considered as upper bounds. Thus, although the populations of the Rb 6s and Cs 7s states and of the lower lying states (Rb 5s and Cs 6s, 6p) are undetermined, the Rb $5p_{3/2}$ and 4d states are nearly equally populated. When we assume that the Rb 5p level is populated purely by radiative decay, this population corresponds to a fraction of about 13% of the original 6s population whereas the $5p_{1/2}$ state is populated only by 7%.[69] However, the fact that the measured population of the $5p_{1/2}$ state only amounts to about 8% of the $5p_{3/2}$ population indicates that an additional droplet-induced decay process is active. In the case of Cs only the 5d state is detected so no quantitative comparison with other states can be made.

The detection of photoelectrons exclusively out of relaxed states seems to contradict the results from ion imaging which clearly demonstrate that desorption proceeds according to the pseudodiatomic model for a fixed $(n + 1)$sΣ electronic configuration. For Na excited into the droplet-perturbed states 5s and 4d, the presence of relaxation channels was also observed in the speed distributions of the desorbed atoms.[44] A broad, nearly laser wavelength independent component extending out to velocities ~1500 m/s (kinetic energy ~270 meV) was assigned to atoms having undergone relaxation to

the lower 3d level. However, in the present experiments on Rb and Cs in the $(n + 1)$s state, no such broad component of the ion distributions is observed (Figure 3). The range of kinetic energies observed (Figure 6) matches well the values expected for dissociation proceeding along the Rb and Cs $(n + 1)s\Sigma$ potentials, Figure 1.

Furthermore, we have considered the possibility that the photoelectron peaks from relaxed states could be associated with Rb_2^+ and Cs_2^+ dimer ions. However, the relative yield of dimers falls far below the proportion of photoelectrons in relaxed states. Besides, the dependence of the signal intensity of the relaxed electrons on the Rb and Cs vapor pressure in the doping cells clearly indicates that these electrons correlate to Rb^+ and Cs^+ atomic ions. In addition, the possible correlation of these electrons with large ion masses, resulting from unfragmented ion-doped He droplets, was probed by performing dedicated time-of-flight measurements using a different detection unit. The measured proportion of large cluster ions to Rb^+ again stayed well behind that of relaxed electrons to (undetected) electrons out of the Rb 6s state. However, due to the uncertainty in determining the relative detection efficiency for large ions, this possibility cannot strictly be ruled out.

Thus, our observations seem to imply that electronic relaxation occurs with some time delay with respect to the strong repulsive interaction which accelerates the dopant atom away from the droplet surface. He-induced electronic couplings may be facilitated by the formation of a compressed shell of He atoms around the dopant in the course of desorption (t = 0.5−1.5 ps, Figure 8). Theoretical modeling of the coupled electron dynamics of excited dopant−droplet complexes as well as time and mass-resolved ion and electron imaging experiments are needed to resolve this puzzling issue.

For the sake of completeness we present in Figure 12 the results of analyzing a series of photoelectron images taken within the Rb $6s\Sigma$ band. The slight shift to higher wavenumbers of the spectral feature measured by detecting electrons with respect to ions (Figure 12a) likely results from contributions of ionized Rb_2 in the electron measurement.

The relative yields of photoelectrons out of the relaxed states 4d, $5p_{3/2}$, and $5p_{1/2}$ are depicted in Figure 12b. Similarly to our previous measurements around the Rb $6p\Pi$ state, the relative populations of the lowest detected levels increase as the laser is detuned below the droplet resonance. This change in relative populations likely reflects the variation of the monomer to dimer ratio. Changing relaxation rates into the various target electronic states of Rb due to droplet interactions may also contribute.

The anisotropy parameters β_2 and β_4, which characterize the angular distribution of emitted electrons by two-photon ionization,[70] are depicted in Figure 12c,d. The values of β_2 remain nearly constant within the accuracy of the measurement over the excitation spectrum. The β_4 values for the 5p states are roughly consistent with zero for all laser wavenumbers. This indicates vanishing alignment of the electron orbitals as previously found for Rb $6p\Pi$ excitation.[33] However, the 4d orbital appears to retain a certain degree of orbital alignment when exciting on the blue side of the Rb $6s\Sigma$ band. Likely, this is due to faster desorption when exciting further up the repulsive branch of the $Rb-He_N$ potential.

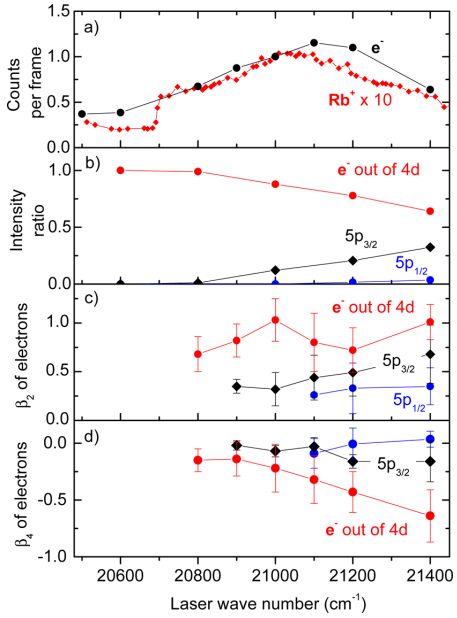

Figure 12. Total photoion signal and photoelectron counts (a), relative abundances of electrons out of different atomic states (b), and anisotropy parameters β_2 (c) and β_4 (d) inferred from electron images recorded a various laser wavelengths around the maximum of the Rb $6s\Sigma$ absorption band.

SUMMARY

We have studied the desorption dynamics of the heavy alkali metal atoms Rb and Cs off the surface of He nanodroplets, initiated by excitation to the perturbed 6s and 7s states, respectively. As for Li and Na adatoms,[22] the calculations reveal a complex response of the He droplet to the impulsive perturbation induced by the excitation of the Rb and Cs adatoms. We find significant local deformations of the droplets and three distinct types of nonlinear density waves that propagate through the droplets at different speeds. Nevertheless, both the measured and theoretically calculated mean kinetic energies of the desorbed atoms, which are in excellent agreement, can be modeled as a simple pseudodiatomic direct photodissociation reaction driven by a highly repulsive interaction. We find values of the effective mass of the He droplet interacting with Rb and Cs of about 10 and 13 He atoms, respectively. Deviations from this simple model are found experimentally for the desorption dynamics of Rb on He droplets excited to the 6p state.

The photoelectron spectra measured upon excitation to the perturbed 6s and 7s states evidence significant electronic relaxation of the desorbed Rb and Cs atoms into lower-lying states, at variance with analogous measurements using the light alkali metal species Li and Na attached to He droplets. Though the ion and electron measurements appear to be contradictory, possible correlations of the observed electrons with other ion signals can largely be ruled out.

This puzzling issue will be further studied by measuring photoelectron spectra with femtosecond time-resolution in pump−probe experiments. Further theoretical work in this direction is also planned.

■ ASSOCIATED CONTENT

Supporting Information

Animated views (mpg files) of the evolution of the helium density distributions upon excitation of rubidium and cesium adatoms are available as Supporting Information. This material is available free of charge via the Internet at http://pubs.acs.org.

■ AUTHOR INFORMATION

Corresponding Author

*M. Mudrich: e-mail, mudrich@physik.uni-freiburg.de.

Notes

The authors declare no competing financial interest.

■ ACKNOWLEDGMENTS

The authors gratefully acknowledge support by DGI, Spain (FEDER), under Grant No. FIS2011-28617-C02-01, by Generalitat de Catalunya (2009SGR1289), and by the Deutsche Forschungsgemeinschaft. A.L. has been supported by the ME (Spain) FPI program, Grant No. BES-2012-057439.

■ REFERENCES

(1) Stienkemeier, F.; Vilesov, A. F. Electronic spectroscopy in He droplets. *J. Chem. Phys.* **2001**, *115*, 10119−10137.

(2) Toennies, J. P.; Vilesov, A. F. Superfluid helium droplets: A uniquely cold nanomatrix for molecules and molecular complexes. *Angew. Chem., Int. Ed.* **2004**, *43*, 2622−2648.

(3) Stienkemeier, F.; Lehmann, K. K. Spectroscopy and dynamics in helium nanodroplets. *J. Phys. B: At. Mol. Opt. Phys.* **2006**, *39*, R127−R166.

(4) Barranco, M.; Guardiola, R.; Hernández, S.; Mayol, R.; Navarro, J.; Pi, M. Helium Nanodroplets: an Overview. *J. Low Temp. Phys.* **2006**, *142*, 1−81.

(5) Kornilov, O.; Bünermann, O.; Haxton, D. J.; Leone, S. R.; Neumark, D. M.; Gessner, O. Femtosecond Photoelectron Imaging of Transient Electronic States and Rydberg Atom Emission from Electronically Excited He Droplets. *J. Phys. Chem. A* **2011**, *115*, 7891−7900.

(6) Bünermann, O.; Kornilov, O.; Haxton, D. J.; Leone, S. R.; Neumark, D. M.; Gessner, O. Ultrafast probing of ejection dynamics of Rydberg atoms and molecular fragments from electronically excited helium nanodroplets. *J. Chem. Phys.* **2012**, *137*, 214302.

(7) Droppelmann, G.; Bünermann, O.; Schulz, C. P.; Stienkemeier, F. Formation Times of RbHe Exciplexes on the Surface of Superfluid versus Normal Fluid Helium Nanodroplets. *Phys. Rev. Lett.* **2004**, *93*, 023402.

(8) Döppner, T.; Fennel, T.; Diederich, T.; Tiggesbäumker, J.; Meiwes-Broer, K. H. Controlling the Coulomb Explosion of Silver Clusters by Femtosecond Dual-Pulse Laser Excitation. *Phys. Rev. Lett.* **2005**, *94*, 013401.

(9) Claas, P.; Droppelmann, G.; Schulz, C. P.; Mudrich, M.; Stienkemeier, F. Wave packet dynamics of potassium dimers attached to helium nanodroplets. *J. Phys. B* **2006**, *39*, S1151.

(10) Przystawik, A.; Göde, S.; Döppner, T.; Tiggesbäumker, J.; Meiwes-Broer, K.-H. Light induced collapse of metastable magnesium complexes formed in helium nanodroplets. *Phys. Rev. A* **2008**, *78*, 021202.

(11) Mudrich, M.; Heister, P.; Hippler, T.; Giese, C.; Dulieu, O.; Stienkemeier, F. Spectroscopy of triplet states of Rb_2 by femtosecond pump-probe photoionization of doped helium nanodroplets. *Phys. Rev. A* **2009**, *80*, 042512.

(12) Pentlehner, D.; Nielsen, J. H.; Slenczka, A.; Mølmer, K.; Stapelfeldt, H. Impulsive Laser Induced Alignment of Molecules Dissolved in Helium Nanodroplets. *Phys. Rev. Lett.* **2013**, *110*, 093002.

(13) Pentlehner, D.; Nielsen, J. H.; Christiansen, L.; Slenczka, A.; Stapelfeldt, H. Laser-induced adiabatic alignment of molecules dissolved in helium nanodroplets. *Phys. Rev. A* **2013**, *87*, 063401.

(14) Göde, S.; Irsig, R.; Tiggesbäumker, J.; Meiwes-Broer, K.-H. Time-resolved studies on the collapse of magnesium atom foam in helium nanodroplets. *New J. Phys.* **2013**, *15*, 015026.

(15) Whaley, K. B. Structure and dynamics of quantum clusters. *Int. Rev. Phys. Chem.* **1994**, *13*, 41−84.

(16) Kwon, Y.; Huang, P.; Patel, M. V.; Blume, D.; Whaley, K. B. Quantum solvation and molecular rotations in superfluid helium clusters. *J. Chem. Phys.* **2000**, *113*, 6469−6501.

(17) Chin, S. A.; Krotscheck, E. Systematics of pure and doped ^{4}He clusters. *Phys. Rev. B* **1995**, *52*, 10405−10428.

(18) Krotscheck, E.; Zillich, R. Dynamics of ^{4}He droplets. *J. Chem. Phys.* **2001**, *115*, 10161−10174.

(19) Giacomazzi, L.; Toigo, F.; Ancilotto, F. Dynamics of liquid ^{4}He in confined geometries from time-dependent density functional calculations. *Phys. Rev. B* **2003**, *67*, 104501.

(20) Lehtovaara, L.; Kiljunen, T.; Eloranta, J. Efficient numerical method for simulating static and dynamic properties of superfluid helium. *J. Comput. Phys.* **2004**, *78*, 194.

(21) Mateo, D.; Jin, D.; Barranco, M.; Pi, M. Excited electron-bubble states in superfluid ^{4}He: A time-dependent density functional approach. *J. Chem. Phys.* **2011**, *134*, 044507.

(22) Hernando, A.; Barranco, M.; Pi, M.; Loginov, E.; Langlet, M.; Drabbels, M. Desorption of alkali atoms from ^{4}He nanodroplets. *Phys. Chem. Chem. Phys.* **2012**, *14*, 3996−4010.

(23) Mateo, D.; Hernando, A.; Barranco, M.; Loginov, E.; Drabbels, M.; Pi, M. Translational dynamics of photoexcited atoms in ^{4}He nanodroplets: the case of silver. *Phys. Chem. Chem. Phys.* **2013**, *15*, 18388−18400.

(24) Mateo, D.; Leal, A.; Hernando, A.; Barranco, M.; Pi, M.; Cargnoni, F.; Mella, M.; Zhang, X.; Drabbels, M. Communication: Nucleation of quantized vortex rings in 4He nanodroplets. *J. Chem. Phys.* **2014**, *140*, 131101.

(25) Dalfovo, F. Atomic and molecular impurities in ^{4}He clusters. *Z. Phys. D* **1994**, *29*, 61−66.

(26) Ancilotto, F.; DeToffol, G.; Toigo, F. Sodium dimers on the surface of liquid ^{4}He. *Phys. Rev. B* **1995**, *52*, 16125−16129.

(27) Stienkemeier, F.; Ernst, W. E.; Higgins, J.; Scoles, G. On the use of liquid helium cluster beams for the preparation and spectroscopy of the triplet states of alkli dimers and other weakly bound complexes. *J. Chem. Phys.* **1995**, *102*, 615−617.

(28) Reho, J.; Higgins, J.; Callegari, C.; Lehmann, K. K.; Scoles, G. Alkali-helium exciplex formation on the surface of helium nanodroplets. I. Dispersed emission spectroscopy. *J. Chem. Phys.* **2000**, *113*, 9686−9693.

(29) Schulz, C. P.; Claas, P.; Stienkemeier, F. Formation of K*He exciplexes on the surface of helium nanodroplets studied in real time. *Phys. Rev. Lett.* **2001**, *87*, 153401.

(30) Callegari, C.; Ancilotto, F. Perturbation Method to Calculate the Interaction Potentials and Electronic Excitation Spectra of Atoms in He Nanodroplets. *J. Phys. Chem. A* **2011**, *115*, 6789−6796.

(31) Auböck, G.; Nagl, J.; Callegari, C.; Ernst, W. E. Electron Spin Pumping of Rb Atoms on He Nanodroplets via Nondestructive Optical Excitation. *Phys. Rev. Lett.* **2008**, *101*, 035301.

(32) Theisen, M.; Lackner, F.; Ernst, W. E. Rb and Cs Oligomers in Different Spin Configurations on Helium Nanodroplets. *J. Phys. Chem. A* **2011**, *115*, 7005−7009.

(33) Fechner, L.; Grüner, B.; Sieg, A.; Callegari, C.; Ancilotto, F.; Stienkemeier, F.; Mudrich, M. Photoionization and imaging spectroscopy of rubidium atoms attached to helium nanodroplets. *Phys. Chem. Chem. Phys.* **2012**, *14*, 3843−3851.

(34) Stienkemeier, F.; Higgins, J.; Callegari, C.; Kanorsky, S. I.; Ernst, W. E.; Scoles, G. Spectroscopy of alkali atoms (Li, Na, K) attached to large helium clusters. *Z. Phys. D* **1996**, *38*, 253−263.

(35) Bünermann, O.; Droppelmann, G.; Hernando, A.; Mayol, R.; Stienkemeier, F. Unraveling the Absorption Spectra of Alkali Metal Atoms Attached to Helium Nanodroplets. *J. Phys. Chem. A* **2007**, *111*, 12684−12694.

(36) Loginov, E.; Callegari, C.; Ancilotto, F.; Drabbels, M. Spectroscopy on Rydberg States of Sodium Atoms on the Surface of Helium Nanodroplets. *J. Phys. Chem. A* **2011**, *115*, 6779−6788.
(37) Lackner, F.; Krois, G.; Theisen, M.; Koch, M.; Ernst, W. E. Spectroscopy of nS, nP, and nD Rydberg series of Cs atoms on helium nanodroplets. *Phys. Chem. Chem. Phys.* **2011**, *13*, 18781−18788.
(38) Busch, G. E.; Wilson, K. R. Triatomic Photofragment Spectra. II. Angular Distributions from NO_2 Photodissociation. *J. Chem. Phys.* **1972**, *56*, 3638−3654.
(39) Reho, J.; Callegari, C.; Higgins, J.; Ernst, W. E.; Lehmann, K. K.; Scoles, G. Spin-orbit effects in the formation of the Na-He excimer on the surface of He clusters. *Faraday Discuss.* **1997**, *108*, 161−174.
(40) Brühl, F. R.; Trasca, R. A.; Ernst, W. E. Rb-He exciplex formation on helium nanodroplets. *J. Chem. Phys.* **2001**, *115*, 10220−10224.
(41) Mudrich, M.; Droppelmann, G.; Claas, P.; Schulz, C.; Stienkemeier, F. Quantum interference spectroscopy of RbHe exciplexes formed on helium nanodroplets. *Phys. Rev. Lett.* **2008**, *100*, 023401.
(42) Giese, C.; Mullins, T.; Grüner, B.; Weidemüller, M.; Stienkemeier, F.; Mudrich, M. Formation and relaxation of RbHe exciplexes on He nanodroplets studied by femtosecond pump and picosecond probe spectroscopy. *J. Chem. Phys.* **2012**, *137*, 244307.
(43) Takahashi, Y.; Sano, K.; Kinoshita, T.; Yabuzaki, T. Spectroscopy of alkali atoms and molecules in superfluid helium. *Phys. Rev. Lett.* **1993**, *71*, 1035−1038.
(44) Loginov, E.; Drabbels, M. Dynamics of Excited Sodium Atoms Attached to Helium Nanodroplets. *J. Phys. Chem. A* **2014**, *118*, 2738−2748.
(45) Loginov, E.; Drabbels, M. Spectroscopy and dynamics of barium-doped helium nanodroplets. *J. Chem. Phys.* **2012**, *136*, 154302.
(46) Loginov, E.; Drabbels, M. Excited State Dynamics of Ag Atoms in Helium Nanodroplets. *J. Phys. Chem. A* **2007**, *111*, 7504−7515.
(47) Kautsch, A.; Koch, M.; Ernst, W. E. Electronic Relaxation after Resonant Laser Excitation of Cr in Superfluid Helium Nanodroplets. *J. Phys. Chem. A* **2013**, *117*, 9621−9625.
(48) Lindebner, F.; Kautsch, A.; Koch, M.; Ernst, W. E. Laser ionization and spectroscopy of Cu in superfluid helium nanodroplets. *Int. J. Mass Spectrom.* **2014**, *365 - 366*, 255−259.
(49) Vrakking, M. J. J. An iterative procedure for the inversion of two-dimensional ion/photoelectron imaging experiments. *Rev. Sci. Instrum.* **2001**, *72*, 4084.
(50) Garcia, G. A.; Nahon, L.; Powis, I. Two-dimensional charged particle image inversion using a polar basis function expansion. *Rev. Sci. Instrum.* **2004**, *75*, 4989−4996.
(51) Ellison, F. O. A Method of Diatomics in Molecules. I. General Theory and Application to H_2O. *J. Am. Chem. Soc.* **1963**, *85*, 3540.
(52) Dalfovo, F.; Lastri, A.; Pricaupenko, L.; Stringari, S.; Treiner, J. Structural and dynamical properties of superfluid helium. *Phys. Rev. B* **1995**, *52*, 1193.
(53) Patil, S. H. Adiabatic potentials for alkali-inert gas systems in the ground state. *J. Chem. Phys.* **1991**, *94*, 8089−8095.
(54) Pascale, J. Use of *l*-dependent preudopotentials in the study of alkali-metal-atom-He systems. The adiabatic molecular potentials. *Phys. Rev. A* **1983**, *28*, 632−644.
(55) Ralston, A.; Wilf, H. S. *Mathematical methods for digital computers*; John Wiley and Sons: New York, 1960.
(56) Koutselos, A. D.; Mason, E. A.; Viehland, L. A. Interaction universality and scaling laws for interaction potentials between closed-shell atoms and ions. *J. Chem. Phys.* **1990**, *93*, 7125−7136.
(57) LeRoy, R. J.; Kraemer, G. T. BCONT 2.2. Computer Program for Calculating Absorption Coefficients, Emission Intensities or (Golden Rule) Predissociation Rates. The source code and manual for this program may be obtained from "Computer Programs link at http://leroy.uwaterloo.ca. University of Waterloo Chemical Physics Research, Report CP-650R^2, 2004.
(58) Mateo, D.; Hernando, A.; Barranco, M.; Mayol, R.; Pi, M. Absorption spectrum of atomic impurities in isotopic mixtures of liquid helium. *Phys. Rev. B* **2011**, *83*, 174505.
(59) Pifrader, A.; Allard, O.; Auböck, G.; Callegari, C.; Ernst, W. E.; Huber, R.; Ancilotto, F. One- and two-photon spectroscopy of highly excited states of alkali-metal atoms on helium nanodroplets. *J. Chem. Phys.* **2010**, *133*, 164502.
(60) Lozeille, J.; Fioretti, A.; Gabbanini, C.; Huang, Y.; Pechkis, H.; Wang, D.; Gould, P.; Eyler, E.; Stwalley, W.; Aymar, M.; Dulieu, O. Detection by two-photon ionization and magnetic trapping of cold Rb_2 triplet state molecules. *Eur. Phys. J. D* **2006**, *39*, 261−269.
(61) Zare, R. N. Photoejection Dynamics. *Mol. Photochem* **1972**, *44*, 1.
(62) Ancilotto, F.; Cheng, E.; Cole, M. W.; Toigo, F. The binding of alkali atoms to the surfaces of liquid helium and hydrogen. *Z. Phys. D* **1995**, *98*, 323−329.
(63) Gallagher, T. *Rydberg Atoms*; Cambridge University Press: Cambridge, U.K., 1994.
(64) Peterka, D. S.; Kim, J. H.; Wang, C. C.; Poisson, L.; Neumark, D. M. Photoionization Dynamics of Pure Helium Droplets. *J. Phys. Chem. A* **2007**, *111*, 7449−7459.
(65) Loginov, E. Photoexcitation and Photoionization Dynamics of Doped Liquid Helium-4 Nanodroplets. Ph.D. thesis, École Polytechnique Fédérale de Lausanne, 2008.
(66) Moskvin, Y. V. Photoionization of atoms and recombination of ions in the vapors of alkali metals. *Opt. Spectrosc.* **1963**, *15*, 316−318.
(67) Lahiri, J.; Manson, S. T. Oscillator-strength distributions for discrete and continuum transitions of excited states of cesium. *Phys. Rev. A* **1986**, *33*, 3151−3165.
(68) Aymar, M.; Robaux, O.; Wane, S. Central-field calculations of photoionisation cross sections of excited states of Rb and Sr^+ and analysis of photoionisation cross sections of excited alkali atoms using quantum defect theory. *J. Phys. B* **1984**, *17*, 993−1007.
(69) Heavens, O. Radiative Transition Probabilities of the Lower Excited States of the Alkai Metals. *J. Opt. Soc. Am.* **1961**, *51*, 1058−1061.
(70) Reid, K. L. Photoelectron angular distributions. *Annu. Rev. Phys. Chem.* **2003**, *54*, 397−424.

3.2 Picosecond solvation dynamics of alkali cations

Resumen (Spanish)

En esta sección se presenta el estudio de la dinámica de átomos neutros de rubidio y cesio tras su fotoionización desde su posición de equilibrio sobre la superficie de una nanogota de $^4He_{1000}$ superfluida, utilizando la TDDFT. Este estudio complementa al presentado para el caso del Ba (Sección 2.1).

Estas dinámicas comienzan con el desplazamiento de las impurezas hacia el interior de la gota debido a la interacción atractiva que existe entre ambos cationes y el helio. Debido a estas fuertes interacciones atractivas, los átomos de helio en la superficie de la nanogota más cercanos a las impurezas son rápidamente atraídos hacia las impurezas, produciendo la formación de estructuras con capas de solvatación de alta densidad —llamadas *snowball*— en torno a los cationes de Rb^+ y Cs^+.

En el caso del rubidio se observa que esta estructura está completamente formada tras los diez primeros picosegundos, produciéndose para tiempos más largos la solvatación de la impureza; mientras que para el caso del cesio, la formación del *snowball* impide que la impureza de hunda hacia el interior de la nanogota, haciendo que el Cs^+ escape de la gota llevando consigo algunas decenas de átomos de helio. Esto es debido a que el apantallamiento producido por esta formación de helio hace que la estructura Cs^+ + *snowball* esté poco ligada a la gota. Estos resultados se deben en parte al tamaño del catión de cesio con respecto al tamaño de la nanogota, como hemos podido comprobar mediante la simulación de este fenómeno usando una superficie helio libre en lugar de una gota, en el que ambos cationes experimentan un hundimiento directo hacia el interior del líquido como cabe esperar debido la fuerte interacción atractiva entre las impurezas y el helio.

Por otro lado, en el caso del Rb^+ se observa la nucleación de vórtices cuantizados a consecuencia de las fuertes deformaciones superficiales producidas por el hundimiento del catión.

PHYSICAL REVIEW B **90**, 224518 (2014)

Picosecond solvation dynamics of alkali cations in superfluid ^{4}He nanodroplets

Antonio Leal,[1] David Mateo,[1,2] Alberto Hernando,[3] Martí Pi,[1] Manuel Barranco,[1] Alessandro Ponti,[4] Fausto Cargnoni,[4] and Marcel Drabbels[5]

[1]*Departament ECM, Facultat de Física, and IN^{2}UB, Universitat de Barcelona, Diagonal 645, 08028 Barcelona, Spain*

[2]*Department of Chemistry and Biochemistry, California State University at Northridge, 18111 Nordhoff St., Northridge, California 91330, USA*

[3]*Laboratory of Theoretical Physical Chemistry, Institut des Sciences et Ingénierie Chimiques, Swiss Federal Institute of Technology Lausanne (EPFL), CH-1015 Lausanne, Switzerland*

[4]*Istituto di Scienze e Tecnologie Molecolari (ISTM), Consiglio Nazionale delle Ricerche, via Golgi 19, 20133 Milano, Italy*

[5]*Laboratoire de Chimie Physique Moléculaire, Swiss Federal Institute of Technology Lausanne (EPFL), CH-1015 Lausanne, Switzerland*

(Received 10 September 2014; revised manuscript received 29 October 2014; published 19 December 2014)

The dynamics following the photoionization of neutral Rb and Cs atoms residing in a dimple at the surface of a superfluid $^4He_{1000}$ nanodroplet has been investigated within time-dependent density functional theory, complementing a previous study on Ba. The calculations reveal that structured high density helium solvation layers form around both the Rb^+ and Cs^+ cation on a picosecond time scale, forming so-called snowballs. In contrast to the Rb^+ ion, Cs^+ is not solvated by the $^4He_{1000}$ droplet but rather desorbs from it as a Cs^+He_n snowball. This outcome is partially related to the large size of Cs^+ cation in relation to the helium droplet as is revealed by calculations performed using a planar helium surface. The large droplet deformations induced by the solvation of the Rb^+ cation is found to lead to efficient nucleation of quantized vortex loops or rings.

DOI: 10.1103/PhysRevB.90.224518 PACS number(s): 36.40.Wa, 32.30.Jc, 67.25.dw, 67.25.dk

I. INTRODUCTION

Ions are often used as probes to investigate the properties of superfluid liquid helium by determining their mobility (see Refs. [1–4], and references therein). Due to electrostriction, the positive ion locally perturbs the superfluid so strongly that in most cases it is surrounded by very inhomogeneous, high density helium solvation layers [2]. The solvation structure, which depends strongly on the ionic species, is a nanoscopic solidlike complex that rigidly moves along with the cation, hence its name "snowball" [5]. Potentially these ionic snowballs can also be used to probe the properties of helium nanodroplets. These droplets are created by condensation of the expanding helium gas and reach a limiting temperature of about 0.37 K [6,7], clearly below the superfluid transition temperature in liquid ^{4}He, $T_\lambda = 2.17$ K. Early Quantum Monte Carlo (QMC) calculations indicated that a very small droplet containing less than 100 atoms already displays features pertaining to the superfluid state of bulk liquid helium [8–11]. This was later confirmed in a cornerstone experiment by Toennies and co-workers on mixed ^{3}He-^{4}He droplets doped with carbonyl sulfide (OCS) [12]. The solvated OCS molecule was found to display a rotationally resolved vibrational spectrum, indicating that it rotates inside the ^{4}He core of the mixed droplet. The minimum number of ^{4}He atoms in the core needed to produce the effect was found to be about 60, in good agreement with the calculations [8].

Another manifestation of superfluidity is the frictionless displacement of impurities inside helium if they move at velocities below the so-called critical Landau velocity v_L. This property is due to the peculiar maxon-roton structure of the superfluid excitation spectrum. Impurities moving inside a superfluid helium droplet would lose their translational energy by exciting elementary excitation until reaching a velocity below v_L. Consequently, if impurities are ejected from the droplet their velocity distribution should display a limiting velocity. This has been recently established for several atomic and molecular impurities in droplets consisting of just 1000 helium atoms [13,14].

The appearance of quantized vortices is yet another manifestation of superfluidity. First experimental indications of the presence of vortices in helium droplets was provided by the surface deposition of large droplets doped with Ag atoms [15]. Upon impact, the helium atoms evaporate while the Ag atoms remain on the surface keeping their "*in situ*" cluster structure, revealing a filamentlike distribution corresponding to the vortex line they were originally attached to inside the droplet. Experiments for other atomic impurities have been recently conducted, where the presence of vortex lines in helium droplets has been exploited to guide the formation of ultrathin nanowires [16–18].

Very recently, in a femtosecond x-ray coherent diffractive imaging experiment the existence of vortex arrays in helium droplets has been confirmed [19]. The diffraction images revealed characteristic Bragg patterns from Xe clusters trapped on the vortex cores present in the helium droplets. These droplets are produced by fragmentation of a cryogenic fluid and consist of $N = 10^8$–10^{11} atoms and are thus true mesoscopic pieces of superfluid helium. Hence, it is not surprising that they host vortex lines, which either preexist in the expanding fluid or are created in the fragmentation process.

A different question is whether vortices nucleate when droplets are created by condensation of an expanding gas which is the method used to produce helium droplets containing several thousand atoms [20]. In principle, these droplets can carry enough energy and angular momentum to create a vortex. Moreover, in experiments with doped droplets the pickup process might lead to vortex nucleation. Once nucleated, pinning to the impurity would stabilize a vortex inside the droplet due to the lack of decay channels that conserve both energy and angular momentum [21,22]. The experimental detection of vortices in helium droplets made of

a few thousand He atoms is, however, a still unsolved issue. It is expected that they could be detected by spectroscopic techniques [23,24] as their presence affects the spectrum of the dopants they contain [25,26]. However, for the systems considered the width of the absorption spectrum is larger than the shift introduced by the presence of the vortex, thereby impeding the possible detection of vortices [27,28].

Ionization of an impurity in a helium droplet leads to a strong perturbation of the system since the created cation interacts more strongly with the helium than its neutral precursor. For an impurity residing at the surface of a helium droplet, such as an alkali atom or heavy alkaline-earth atom, the cation is expected to become fully solvated by the helium, i.e., sink into the helium droplet. Several studies indeed indicate that following the ionization of alkali atoms the created cations remain attached to the droplet [29–32]. These experiments, however, provide no details on the location of the cation. Recently the complete solvation of a cation has been experimentally confirmed for Ba^+. The $6p\ ^2P \leftarrow 6s\ ^2S$ absorption spectrum of the Ba^+ cation was found to be identical to that obtained in bulk liquid He, indicating that the ion becomes indeed solvated by the droplet within the 100 ns time scale of the experiment [33]. The solvation dynamics of the Ba^+ has also been addressed theoretically within time-dependent density functional theory (TDDFT) for the $Ba@He_{1000}$ system [28]. It was found that due to the relatively strong ion-helium interaction, the velocity of the Ba^+ cation during the solvation process temporarily exceeds v_L, leading to the nucleation of a quantized ring vortex. The calculated $6p\ ^2P \leftarrow 6s\ ^2S$ absorption spectrum of Ba^+ revealed a clear time dependence due to the solvation of the ion but was not noticeably affected by the presence of the ring vortex [28].

Here we report TDDFT calculations on the solvation dynamics of Rb^+ and Cs^+ cations produced by ionization of the neutral precursor initially located at the surface of a $^4He_{1000}$ droplet. The work on these systems is motivated by recent experiments which reveal that upon ionization extended snowball distributions up to $Rb^+@^4He_{41}$ and $Cs^+@^4He_{41}$ are formed [34], showing distinct intensity steps at masses corresponding to $Rb^+@^4He_{14}$ and $Cs^+@^4He_{16}$. These steps have been identified as the filling of the first solvation shell around the cation, somewhat defining the snowball. In addition, these two systems complement our work on Ba^+ [28]. Since compared to Ba^+, the interaction of an alkali cation with helium is much stronger, the results will provide additional insight into the snowball formation and the nucleation of vortices in small helium droplets.

II. THEORETICAL APPROACH

A. He-dopant pair potentials

One of the key ingredients for the simulations presented in this study are the potential energy curves (PEC) between helium atoms and neutral or charged dopants. The Rb-He and Cs-He ground state pair potentials have been taken from Ref. [35]. These potentials are based on perturbative calculations but agree well with recent *ab initio* computations for Rb-He [36–38] and Cs-He [38] carried out at the CCSD(T) level of theory adopting extended basis sets.

For Rb^+ and Cs^+ cations, the available potentials date back to 1990 [39], and have been essentially obtained by inversion of experimental data. To determine them we performed computations at the CCSD(T) level of theory, as implemented in the MOLPRO 2010 computational code [40]. The core electrons of the metal atoms have been described with the dhf pseudopotential [41], and for the valence electrons we selected the QZVP Gaussians basis set [42]. The aug-cc-pV5Z basis [43] has been adopted for helium, and a $3s3p2d$ set of bond functions [44] has been placed midway between the two nuclei. The interaction energy has been determined in the range from 2 to 12 Å at 33 (38) internuclear distances in the case of Rb^+-He (Cs^+-He), using the standard counterpoise technique proposed by Boys and Bernardi [45]. The spatial grids finely sample (i.e., with 0.1 Å steps) the regions of the repulsive wall and the attractive well of the potentials, while sparser grids are selected for the long-range tail. We also conducted test computations on Rb^+-He at the CCSD(T) level of theory, either adopting the Def2 pseudopotential [46] on the metal atom, and the larger QZVPP basis set [42]. The changes in the computed interaction energy are very small, and do not play a relevant role in the simulation of the dynamics of $Rb^+@^4He_N$ aggregates.

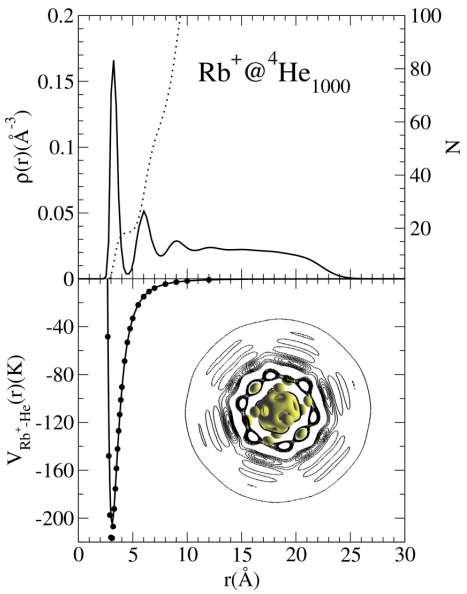

FIG. 1. (Color online) Top panel: Solid line, spherically averaged helium density profile of the $Rb^+@^4He_{1000}$ complex, left scale. Dotted line, number of ^4He atoms as a function of distance to the cation, right scale. Bottom panel: Solid line, Rb^+-He pair potential of Ref. [39]; dots, pair potential calculated in this work. Next to them, the nonaveraged helium density around the cation is shown by means of surfaces of constant density $\rho = 0.08$ Å^{-3}. Ten isodensity contours in a plane passing through the center of the complex are shown in the 0.04–0.0218 Å^{-3} range.

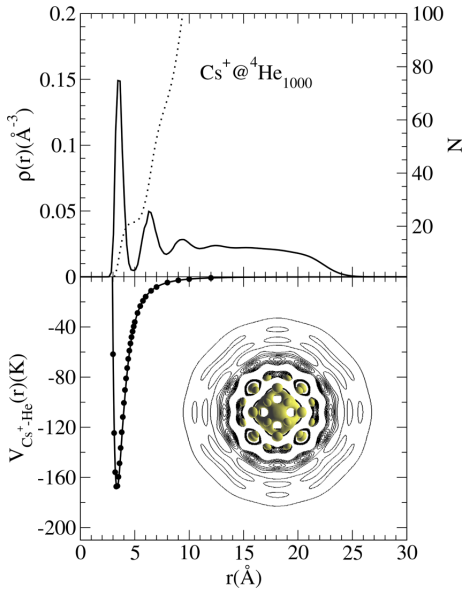

FIG. 2. (Color online) Top panel: Solid line, spherically averaged helium density profile of the $Cs^+@^4He_{1000}$ complex, left scale. Dotted line, number of ^{4}He atoms as a function of distance to the cation, right scale. Bottom panel: Solid line, Cs^+-He pair potential of Ref. [39]; dots, pair potential calculated in this work. Next to them, the nonaveraged helium density around the cation is shown by means of surfaces of constant density $\rho = 0.08$ Å^{-3}. Ten isodensity contours in a plane passing through the center of the complex are shown in the 0.04–0.0218 Å^{-3} range.

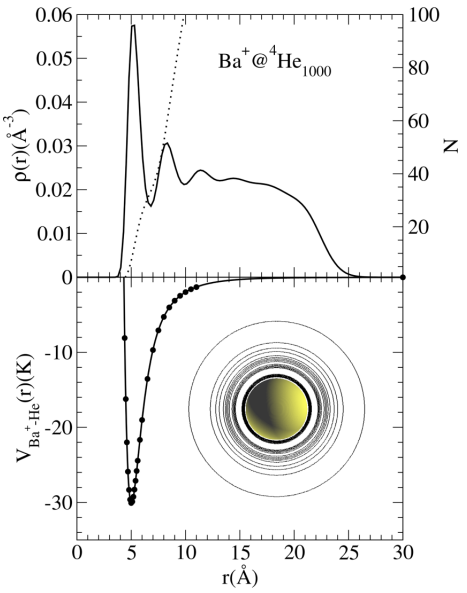

FIG. 3. (Color online) Top panel: Solid line, helium density profile of the $Ba^+@^4He_{1000}$ complex, left scale. Dotted line, number of ^{4}He atoms as a function of distance to the cation, right scale. Bottom panel: Dots, Ba^+-He pair potential [28]. Solid line, fit to the pair potential used in this work that includes a r^{-4} term appropriate for cation-atom potentials. Next to it, the helium density around the cation is shown by means of a surface of density $\rho = 0.05$ Å^{-3}. Ten isodensity contours in a plane passing through the center of the complex are shown in the 0.04–0.0218 Å^{-3} range.

Figures 1 and 2 show the CCSD(T) pair potentials, whose features are consistent with the ionic radii of the two cations: As one moves from Rb^+ to Cs^+ (i.e., increases the size of the charged species) the potential well shifts to larger internuclear distances and its depth decreases. Interestingly, in the two PEC the internuclear distance at the minimum potential energy is quite close to the sum of the ionic radius of the cation and the van der Waals radius of helium (3.06 and 3.21 Å for Rb^+-He and Cs^+-He, respectively). This suggests that in both systems electronic repulsion takes place as soon as the electronic clouds of the cation and helium overlap.

As can be seen in Fig. 2, in the case of Cs^+-He there are no significant differences between our PEC and that proposed by Koutselos *et al.* [39]. We obtain a minimum interaction energy of −169 K at the internuclear distance of 3.35 Å, to be compared with their value of −169 K at 3.47 Å. In the case of Rb^+-He the gross features of both potentials are also similar, but the attractive well calculated at the CCSD(T) level (−218 K) is 5% deeper (−204 K) [39]. The internuclear distance at the minimum is 3.05 Å for both potentials. For this reason, we carried out simulations using both PECs in the case of Rb^+. The results turned out to be very similar and consequently in the following we only discuss those obtained with the CCSD(T) potential. For completeness, we also show in Fig. 3 the He-Ba^+ pair potential [28]. The potential is much less attractive (−30.1 K) as compared to the Rb^+-He and Cs^+-He potentials, and the attractive well is located at larger internuclear distances (5.0 Å) due to the presence of an electron in the 6*s* orbital of barium.

B. DFT for bosons

We address the static and dynamic properties of doped helium droplets within density functional theory (DFT) [47]. In its static version, this approach has been successfully applied to the study of many problems in bulk liquid helium and droplets (see Ref. [48], and references therein). The development of TDDFT methods applicable to microscopic superfluids [49,50] has opened the way to a real-time description of doped droplets in a size range of experimental interest [14,28,51]. Besides DFT, we have used the Born-Oppenheimer approximation to factorize the electronic and nuclear wave functions, the Franck-Condon approximation which assumes that the atomic nuclei do not change their positions or momenta during the electronic transition, and the diatomics-in-molecules approximation [52].

We have considered a droplet made of $N = 1000$ helium atoms and have first obtained the structure of the neutral alkali-droplet complex in the ground state. Due to the large mass of Rb and Cs atoms compared to that of He, we describe them as classical particles in the dynamics while their effect on the statics is incorporated as an external field acting upon

the droplet [14,53]. Accordingly, the energy of the system is written as

$$E[\rho] = \int d\mathbf{r} \left\{ \frac{\hbar^2}{2m_{\mathrm{He}}} |\nabla \sqrt{\rho(\mathbf{r})}|^2 + \mathcal{E}_{\mathrm{He}}[\rho(\mathbf{r})] \right\} + \int d\mathbf{r}\, \rho(\mathbf{r})\, V_X(|\mathbf{r}_{\mathrm{Ak}} - \mathbf{r}|), \quad (1)$$

where $\mathcal{E}_{\mathrm{He}}$ is the potential energy density per unit volume, Ak represents either the Rb or Cs atom, $\rho(\mathbf{r})$ is the He particle density at point $\mathbf{r}$, and $\mathbf{r}_{\mathrm{Ak}}$ is the impurity location.

As indicated, the Rb-He and Cs-He ground state pair potentials V_X have been taken from Ref. [35]. The DF used in the present work [54] is a modified version of the Orsay-Trento functional [47] able to handle very structured helium configurations as those expected to appear around fairly attractive impurities as cations. Examples of such configurations for several alkali and alkaline-earth ion snowballs obtained by static DFT calculations can be found in Refs. [4,55,28].

Upon variation of Eq. (1) one obtains the Euler-Lagrange equation that is solved to determine the equilibrium density $\rho_0(\mathbf{r})$ of the droplet and the location of the dopant atom $\mathbf{r}_{\mathrm{Ak}_0}$ [56]. Schematically,

$$\frac{\delta}{\delta\rho}\left(\frac{\hbar^2}{2m_{\mathrm{He}}} \left|\nabla\sqrt{\rho}\right|^2 + \mathcal{E}_{\mathrm{He}} \right) + V_X = \mu, \quad (2)$$

where μ is the chemical potential of the He droplet.

Equation (2) has been solved in Cartesian coordinates using a spatial grid of 0.4 Å and a 200×200×250 point mesh. The derivatives have been calculated with 13-point formulas. Extensive use of fast-Fourier techniques [57] has been made to efficiently calculate the energy density and mean field potential [14,51]. The calculations indicate that the alkali atoms are located on the surface of the droplets. A two-dimensional plot of the resulting helium dimple structure for Rb and Cs can be found in Fig. 3 of Ref. [56].

The dynamics is triggered by the sudden substitution of the Ak-He ground state pair potential V_X by that corresponding to Ak^+-He, V_X^+. Since the resulting $Ak^+@^4He_{1000}$ configuration is not at equilibrium, the system evolves in time. Within TDDFT, we represent the He droplet by a complex effective wave function $\Psi_{\mathrm{He}}(\mathbf{r},t)$ such that $\rho(\mathbf{r},t) = |\Psi_{\mathrm{He}}(\mathbf{r},t)|^2$. The position of the Ak^+ cation $\mathbf{r}_{Ak^+}(t)$ obeys the Newton equation. Consequently,

$$i\hbar\frac{\partial}{\partial t}\Psi_{\mathrm{He}} = \left[-\frac{\hbar^2}{2m_{\mathrm{He}}}\nabla^2 + \frac{\delta\mathcal{E}_{\mathrm{He}}}{\delta\rho(\mathbf{r})} + V_X^+(|\mathbf{r} - \mathbf{r}_{Ak^+}|) \right]\Psi_{\mathrm{He}},$$

$$m_{Ak^+}\ddot{\mathbf{r}}_{Ak^+} = -\nabla_{\mathbf{r}_{Ak^+}} \left[\int d\mathbf{r}\, \rho(\mathbf{r}) V_X^+(|\mathbf{r} - \mathbf{r}_{Ak^+}|) \right] = -\int d\mathbf{r}[\nabla\rho(\mathbf{r})] V_X^+(|\mathbf{r} - \mathbf{r}_{Ak^+}|). \quad (3)$$

The initial condition to solve Eqs. (3) is the equilibrium droplet-neutral Ak configuration, $\Psi(\mathbf{r}, t=0) = \sqrt{\rho_0(\mathbf{r})}$, $\mathbf{r}_{Ak^+}(t=0) = \mathbf{r}_{\mathrm{Ak}_0}$. The initial velocity of the Ak^+ cation is set to zero. Equations (3) have been solved using the same grid as for the static problem and a time step of 0.5 fs. We have used for both a predictor-corrector method fed by a few time steps obtained by a fourth-order Runge-Kutta algorithm [58].

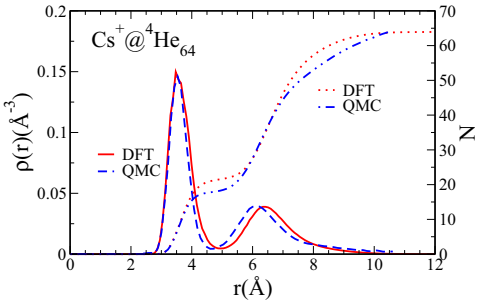

FIG. 4. (Color online) Comparison between the spherically averaged DFT density profile (solid line) and QMC density profile [3] (dashed line) for the $Cs^+@^4He_{64}$ complex, left scale. Also shown is the number of ^{4}He atoms as a function of distance to the cation, right scale.

III. RESULTS

A. Statics

It has been experimentally determined that alkali atoms reside at the surface of ^{4}He droplets [56,59], a result that is reproduced by DFT calculations [56]. At variance, Rb^+ and Cs^+ cations are fully solvated and develop snowball structures [3]. The calculated equilibrium configuration of $Rb^+@^4He_{1000}$ and $Cs^+@^4He_{1000}$ are shown in Figs. 1 and 2, respectively. In both cases, a highly structured helium density appears around the cation, in agreement with variational and QMC calculations [3,60]. The spherically averaged helium number density shown in Figs. 1 and 2 as a function of distance to the cation reveals a clear shell structure. By integrating this density over the radial coordinate the number of helium atoms in the solvation shells can be determined. Using this procedure the first solvation shell is found to host 19.2 (21.4) atoms for Rb^+ (Cs^+). These values are somewhat larger than those found experimentally [32,34] and by QMC calculations [3]. Figure 3 shows the equilibrium configuration of $Ba^+@^4He_{1000}$. In contrast to Rb^+ and Cs^+, the Ba^+ ion is found to be surrounded by a smooth and unstructured helium density, in agreement with QMC calculations [61]. This difference is a direct consequence of the much weaker interaction of the Ba^+ ion with the helium, *vide supra*.

For the sake of comparison, we show in Fig. 4 the spherically averaged DFT density profile and QMC density profile corresponding to the $Cs^+@^4He_{64}$ droplet [3]. It can be seen that the minor discrepancy mainly appears in the second solvation shell. This seems to be a very general trend [4,55], likely reflecting that the occupancy of the first solvation shell is essentially determined by the impurity-droplet interaction and is less sensitive to the theoretical approach used to describe the system.

Using these helium densities we have calculated the zero electron kinetic energy (ZEKE) spectrum for Rb, Cs, and Ba. Besides being interesting by itself [62], the ZEKE spectrum probes the structure of the surface dimple state of the dopant atom and the accuracy of the He-cation ground state pair potential. Since the impurities are described classically and the electron orbitals are not explicitly included, the ZEKE

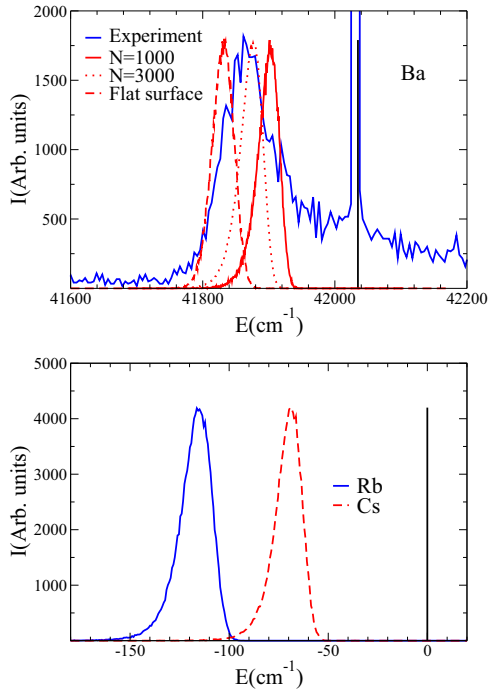

FIG. 5. (Color online) Top panel: ZEKE spectrum for Ba in arbitrary units. Dashed line, experimental result for a $N = 2700$ droplet [62]. Calculated spectra: solid line, $^4He_{1000}$ droplet; squares, $^4He_{3000}$ droplet; dotted line, helium flat surface. The ionization energy of the Ba atom is 42 034.91 cm^{-1} (vertical line) [65]. Bottom panel: Calculated ZEKE spectrum in arbitrary units for Rb (solid line) and Cs (dashed line) in a $N = 1000$ droplet. In both cases, the spectrum refers to the ionization energy (vertical line), 33 690.81 cm^{-1} for Rb and 31 406.47 cm^{-1} for Cs, respectively [65].

spectrum is calculated from the semiclassical approximation of the vibrational Franck-Condon factors of an instantaneous transition from the neutral ground state to the ionic state. This is written as the vertical transition of the atom from the ground state well potential to that of the Ak^+-He well for the same helium configuration:

$$\Delta\omega = \int d\mathbf{r}\, \rho_0(\mathbf{r})\, [V_X^+(|\mathbf{r}_{Ak_0} - \mathbf{r}|) - V_X(|\mathbf{r}_{Ak_0} - \mathbf{r}|)]. \quad (4)$$

The above expression gives the peak position for a given configuration referenced to the ionization energy of a free atom. The complete spectrum is obtained by DF sampling of the helium density [63].

For the case of barium, the Ba-He and Ba^+-He pair potentials have been taken from Refs. [64,28], respectively. The ZEKE spectrum of $Ba^+@^4He_{1000}$, referenced to the ionization energy of Ba, 42 034.91 cm^{-1} [65], is shown in Fig. 5. The experimental spectrum corresponding to a $\bar{N} = 2700$ droplet [62], which is also shown in this figure, has a long tail towards high energies. This tail has been attributed to the presence of autoionizing states in the continuum and consequently should not be considered when comparing to the calculations. The calculated ZEKE spectrum for the $N = 1000$ droplet clearly reveals a smaller shift from the atomic ionization threshold than the experimental spectrum. This apparent disagreement between theory and experiment is likely a finite-size (curvature) effect [66]. To confirm this conjecture we have calculated ZEKE spectra for a $N = 3000$ droplet and also for a flat helium surface (see Sec. III B). The corresponding results which are shown in the top panel of the figure reveal a much better agreement with experiment.

The ZEKE spectra of Rb and Cs presented in Fig. 5 have been calculated using the Ak-He pair potentials available in the literature [35] and the ionic potentials calculated in present work. For these two species, no experimental information is available. A comparison reveals that the helium induced shift is significantly larger for Rb than for Cs. This can be attributed to a stronger Rb^+-He interaction (see Figs. 1 and 2) and the deeper dimple structure for Rb compared to Cs [56]. The calculated shifts are significantly larger than the ionization thresholds that have been determined by extrapolation of the Rydberg series for these systems [67,68], or measured directly via two-step ionization [31]. This difference can be attributed to the fact that experiment and theory do not probe the same ionization threshold. In our calculations we determine the ionization threshold for the direct ionization of the system. In the aforementioned experiments the system is first excited to an intermediate state from which the higher excited states are probed. Following excitation to this intermediate state the system relaxes as the helium rearranges around the excited atom. Consequently, in the experiments the ionization threshold is measured not for the ground state helium configuration but rather for that corresponding to an excited atom. This is thought to be the main reason for the difference between the experimental and theoretical results. This assumption is supported by the ZEKE spectra recorded for ground state and excited Ba atoms on helium droplets [62]. Here the reduction of the ionization threshold for the excited atom was about half of that found for the ground state configuration. A similar difference in the ionization shift is seen here for the Rb and Cs atoms when comparing the experimental and theoretical data. In addition, the calculated shifts match very well the experimentally observed shift for ground state Na atoms on helium droplets [30,69]. In view of this we conclude that the initial position of the impurities as well as their interaction with the helium are accurately described in the present calculations.

B. Dynamics

The static calculations have shown that the equilibrium configuration of the cation-droplet system corresponds to a fully solvated impurity residing in the bulk of the droplet. Based on our work on Ba, it is expected that upon creation of an alkali cation at the surface of a helium droplet the ion becomes fully solvated on a time scale on the order of 10 ps [28]. Figure 6 shows snapshots of the dynamical evolution of the $Rb^+@^4He_{1000}$ system. Inspection of the multimedia material [70], as well as integration of the helium density inside the first solvation shell around the impurity as a function of time, reveals that a snowball structure fully develops in about 20 ps. Notice that the formation of the snowball breaks the axial

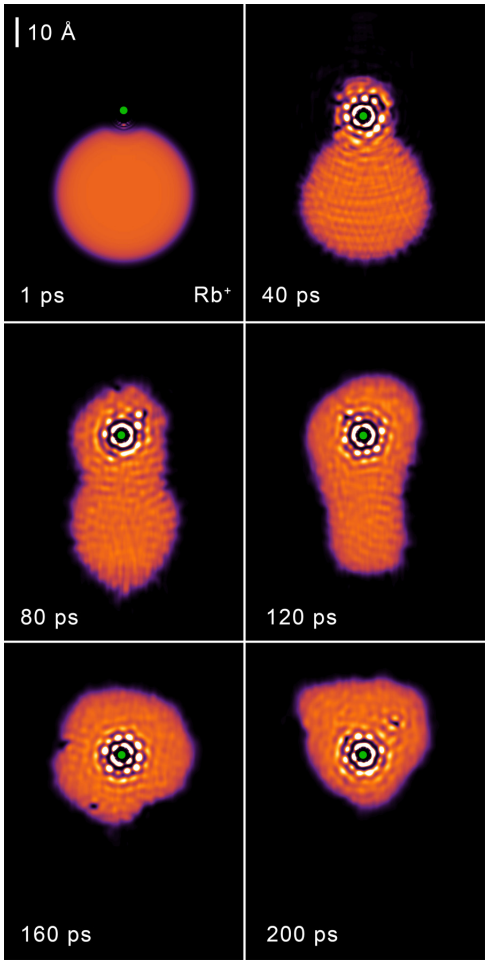

FIG. 6. (Color online) Dynamic evolution of the $Rb^+@^4He_{1000}$ complex when the neutral Rb is suddenly ionized. The corresponding time is indicated in each frame. The dark spots in the $t = 160$ and 200 ps frames are the cross section of nucleated vortex loops (see Fig. 12).

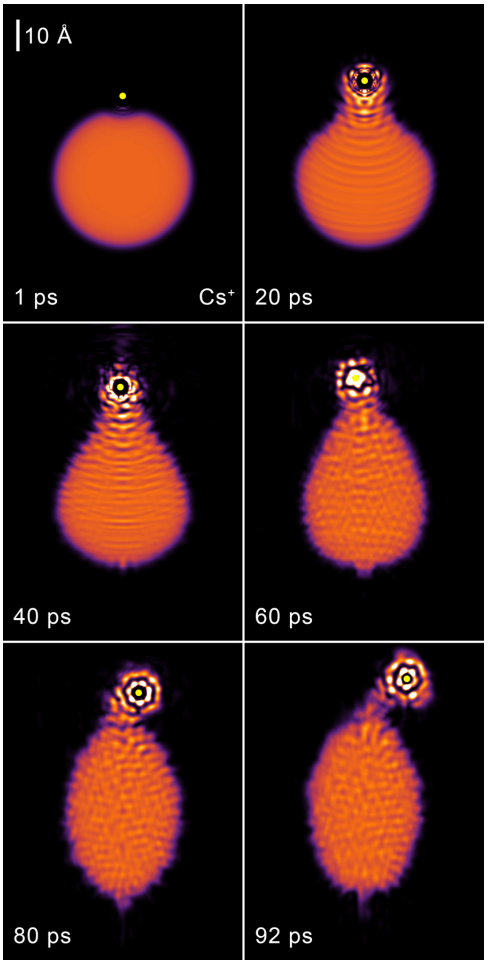

FIG. 7. (Color online) Dynamic evolution of the $Cs^+@^4He_{1000}$ complex when the neutral Cs is suddenly ionized. The corresponding time is indicated in each frame.

symmetry of the system, much like density fluctuations tend to do. This strongly affects the subsequent dynamics of the snowball structure and leads to a loss of the axial symmetry of the droplet. After the formation of the Rb^+ snowball, the whole structure becomes solvated by helium on a 100 ps time scale. During the entire dynamics the Rb^+ ion remains almost stationary while the helium rearranges around the ion. We have found the same behavior and time scales when using the He-Rb^+ pair potential of Ref. [39], even though this interaction potential is less attractive than the one we have calculated here. If one compares the result for Rb^+ with the dynamics of the Ba^+ cation whose interaction with the helium is much weaker [28], one finds noticeable differences between the way these ions become solvated. Whereas the Rb^+ ion remains almost stationary as the helium rearranges, the Ba^+ was found to sink into the helium droplet and to perform a nearly undamped oscillatory motion inside the droplet. The initial position of the cation, i.e., the depth of the dimple structure, as well as the interaction strength thus clearly have a strong effect on the dynamical evolution of the system.

Since the Cs^+-He and Rb^+-He interaction potentials as well as the initial helium dimple structures are quite similar, at least when compared to barium, one expects very similar dynamics for these two alkali ions. Inspection of Fig. 7, which shows the dynamical evolution of the $Cs^+@^4He_{1000}$ system, reveals that like for Rb^+ a solvation shell develops around the Cs^+. The time scale of 30 ps is somewhat longer than for Rb^+, which can be attributed to the slightly weaker interaction of the Cs^+ with the helium and the larger distance between the cation and the droplet. Quite unexpectedly, we find that the Cs^+ cation does not become fully solvated by the helium. Rather it desorbs from the droplet as a snowball containing about 75 helium atoms after $t \gtrsim 90$ ps (see Fig. 8). Thus although

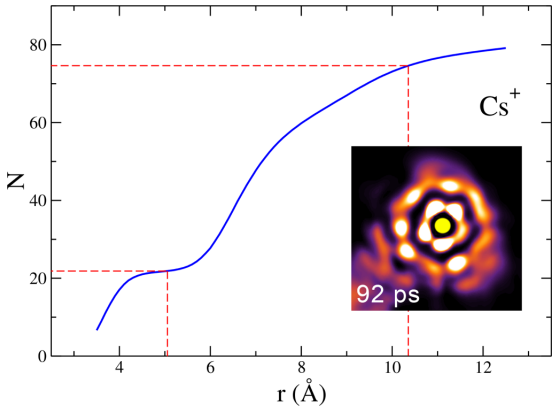

FIG. 8. (Color online) Helium atoms dynamically carried away around Cs^+ at $t = 92$ ps. The shorter horizontal dashed line indicates the number of He atoms in the first solvation shell, and the other line indicates the the total number of He atoms in the ejected, charged nanocluster. The inset shows the appearing snowball from which the distance r is defined.

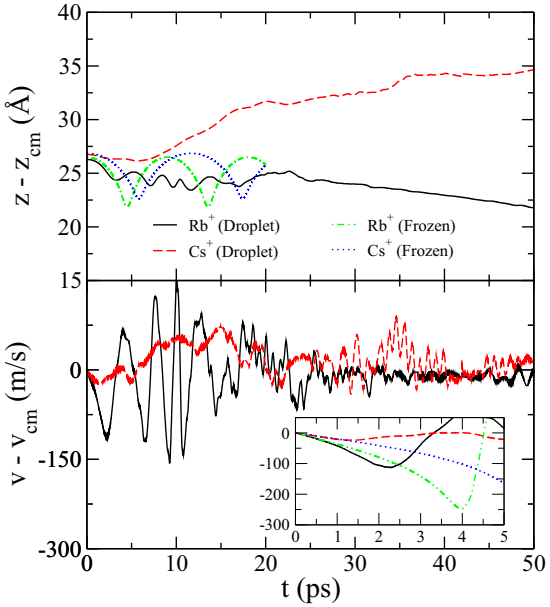

FIG. 9. (Color online) Position and speed of the alkali cation with respect to the helium center of mass as a function of time for the full calculations and for that carried out using the frozen helium density corresponding to the initial conditions. The inset shows the evolution during the first 5 ps.

the interaction strength of Rb^+ and Cs^+ with helium are very similar, the outcome is dramatically different.

We would like to stress that the conspicuous breaking of the axial symmetry in the case of Rb^+ and Cs^+ is not a numerical artifact but the result of the spontaneous symmetry breaking caused by the appearance of the highly structured snowball around the cation. Some details of the subsequent dynamic evolution might depend on the actual conditions of numerical procedure we have used to solve the TDDFT equations such as time and space steps, for instance, that have been chosen by a compromise between accuracy and computational feasibility. Although we cannot disregard that the appearance of these effects are eased by some unavoidable numerical inaccuracies when handling densities as those displayed in Figs. 1 and 2, the effect is rooted on a solid physical ground.

To gain insight into the solvation dynamics we have plotted in Fig. 9 the relative position and velocity of the cation with respect to the center of mass of the droplet. Inspection of this figure reveals that the outcome is already determined during the first few picoseconds of the dynamics. For both systems, the ion starts moving towards the center of the droplet upon its creation. In the case of Ba^+, the velocity of the ion was found to increase rather smoothly with time during the initial phase of the solvation [28]. This is quite different for Rb^+ and Cs^+; after their initial acceleration towards the droplet center, these ions are slowed down and start to move in the opposite direction (see also multimedia material corresponding to Figs. 6, 7, and 9). In the case of Rb^+, the ion reaches a maximum velocity of 112 m/s before it is slowed down and changes its direction after 3.3 ps. During this time the ion has traveled 1.9 Å and penetrated into the droplet. As time goes on the ion accelerates away from the droplet, slows down again, and eventually changes direction anew. This process repeats itself with a period of approximately 3 ps for about 25 ps after which the ion remains almost stationary and becomes solvated by the helium droplet. The Cs^+ ion performs a somewhat similar motion but with a very different outcome. At the start of the evolution the Cs^+ ion is accelerated towards the droplet center but only reaches a speed of 24 m/s before it slows down again. When it comes to a standstill after 3.3 ps it has moved only 0.42 Å and is still at the surface of the droplet. From 5.5 ps onwards the Cs^+ moves away from the droplet from which it eventually desorbs after $t \gtrsim 90$ ps.

As the outcome of the dynamics appears to be determined during the first few picoseconds it raises the question as to what is the origin for the different behavior during the initial phase. Obviously the initial position of the ion will affect the outcome. Upon creation the Ba^+ ion is located in a rather deep dimple while the alkali ions are located considerably further away from the droplet surface, as reflected by the distance between the ion and the helium droplet center of mass which amounts to 25.5, 26.5, and 26.9 Å for Ba^+, Rb^+, and Cs^+, respectively. Consequently, one expects that the Ba^+ ion becomes most easily solvated. The difference in the dynamics of Rb^+ and Cs^+ is not that easily accounted for. Analysis of the ions' motion reveals that the evolution of both systems during the first picosecond is determined by the cation-droplet interaction potential corresponding to the initial condition. This signifies that deformation of the droplet is not important up to this time. Calculations performed using a frozen helium distribution reveal that if the ions were to evolve according to the initial potential they would perform an oscillatory motion with a period of 9 and 11.5 ps for Rb^+ and Cs^+, respectively (see Fig. 9). The fact that a quite different motion is observed at longer times has to be attributed to a

change in the helium density. This change occurs after 1–2 ps as can be seen from the inset of Fig. 9, which compares the velocity of the ions found in the simulations and calculated using the frozen helium density approximation. Analysis of the helium densities suggests that the helium atoms located in the surface region close to the cation are involved. The light helium atoms are expected to be quickly accelerated towards the heavy cation due to the strong Ak^+-He interaction. The helium atoms rushing into the ion will slow it down, or even change its direction. Eventually these helium atoms will bind to the cation to form a snowball structure. At this point the interaction of the cation with the rest of the droplet becomes significantly weakened due to the screening of the ionic charge by the surrounding helium atoms. Depending on the velocity of the snowball and the strength of its interaction with the rest of the droplet it might or might not become solvated.

Thus, solvation, snowball formation, and desorption are dynamical processes that are not simply determined by the energy balance. They are affected by other properties as well, like the size of the helium droplet. As discussed above, the Cs^+ cation does not become solvated by a $^4He_{1000}$ droplet. As the ionic radius is fairly large compared to that of the helium droplet, curvature effects might contribute to a weakening of the ion-droplet effective interaction. Unfortunately, addressing the dynamics of doped droplets with a number of helium atoms significantly larger than $N = 1000$ is computationally very demanding. Preliminary results for $Cs^+@^4He_{2000}$ seem to indicate that in this case the Cs^+ cation becomes solvated by the helium. To establish the behavior for even larger systems we have carried out a series of simulations in which an impurity on a planar helium surface is suddenly ionized. This system has no curvature limitations, and locally mimics a very large droplet. To prevent the spurious bouncing back of the density waves at the walls of the simulation cell an absorbing potential has been added at its boundaries [71]. Figure 10 shows snapshots of the simulation of a Cs atom on a planar helium surface that is suddenly ionized [70]. At variance with the results for the $N = 1000$ droplet, the Cs^+ cation becomes solvated. This difference can be traced back to the initial phase of the evolution. In Fig. 11 the acceleration of the Cs ion during the initial phase of the evolution is plotted. The results for the droplet and the planar surface are very similar during the first few picoseconds, except that the magnitude of the acceleration is slightly larger for the planar surface. As a result, the ion travels further into helium before it is decelerated. This affects the later dynamics and eventually leads to the solvation of the ion. The small difference in the initial acceleration is directly related to the difference in the initial interaction potential. This in turn is fully determined by the helium density distribution resulting from the interaction of the neutral atom with the helium.

The dynamical processes found in this study are closely related to those occurring when ionizing pure helium droplets. As first observed by Gspann, electron impact ionization of He clusters leads to the formation of charged nanoclusters with sizes similar as found for Cs^+ [72]. In those experiments an impinging electron ionizes a helium atom. When this happens at the droplet surface, the situation is rather similar to that in our simulations. The explanation proposed by Gspann for the formation of what he called minicluster ions is essentially the one we have found in our simulations, i.e., the positive

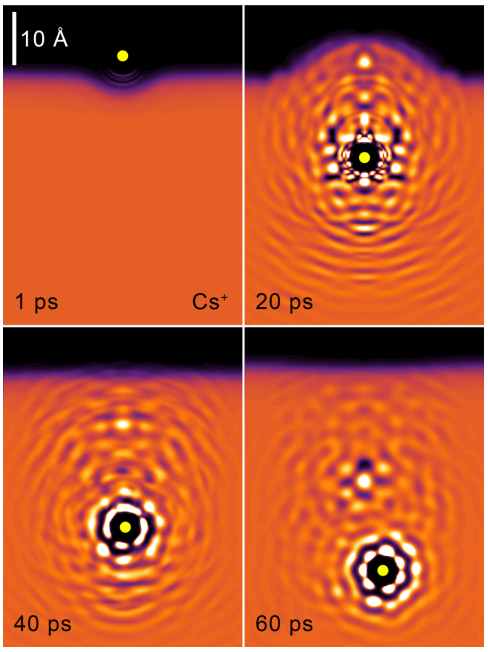

FIG. 10. (Color online) Dynamic evolution of the Cs^+ cation after sudden ionization of the neutral Cs atom sitting in a dimple on a planar helium surface. The corresponding time is indicated in each frame.

charge leads to the formation of a snowball due to the electrostrictive polarization of the surrounding helium. This charged nanocluster may be subsequently expelled from the parent droplet helped by the energy acquired by the ion in the course of the snowball formation.

As indicated in the Introduction, the solvation of Ba^+ is accompanied by the nucleation of a quantized ring vortex.

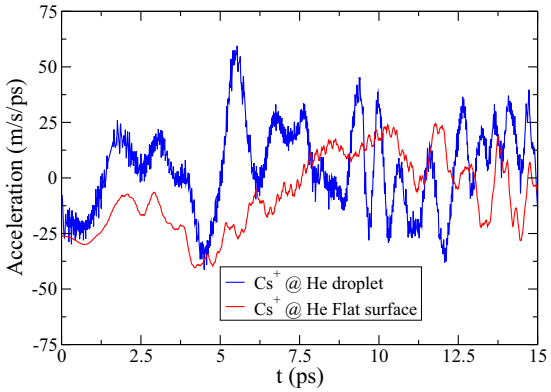

FIG. 11. (Color online) Acceleration experienced by a Cs^+ cation during the initial phase of the solvation after its creation on a $N = 1000$ helium droplet and a flat helium surface.

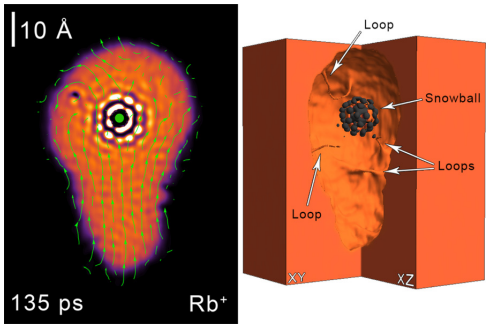

FIG. 12. (Color online) Right: Three-dimensional view of the Rb^+-droplet complex at $t = 135$ ps showing the appearance of several vortex loops attached to the droplet surface and the snowball around the cation. Left: The corresponding circulation lines on the x-z plane cutting a vortex loop.

The same is expected for the solvation of the Rb^+ and Cs^+ cations. In our work on barium we have shown that the speed of the cation has to exceed the critical Landau velocity for a few picoseconds so that the vortex ring has time to nucleate [28]. This condition is not fulfilled in the present simulations, neither for Rb^+ nor for Cs^+ (see Fig. 9). This is most likely related to the same processes leading to the desorption of the Cs^+. During the initial phase of the dynamics when the ion moves towards the droplets it is quickly slowed down by the nearby helium atoms rushing in to form a snowball. Once the snowball has formed the cation-droplet interaction is efficiently screened, thereby limiting the maximum achievable velocity.

Interestingly, we find that in spite of the low velocity of the Rb^+, vortices are nucleated. These result from the large distortions of the droplet surface caused by the solvation of Rb^+ which acts as nucleation seeds. In contrast to the results of our previous work, no vortex rings are formed but quantized vortex loops whose ends are both attached to the droplet surface [73,74]. One such configuration is displayed in Fig. 12 [70]. The rather distorted vortex loops found here bear some geometric similarity to the equilibrium configurations of the curved vortices described in Refs. [22,75]. While these simulations do not reveal the nucleation of vortex rings this does not imply that these cannot form. As a matter of fact, the simulation using the Koutselos Rb^+-He pair potentials reveals the nucleation of a quantized vortex ring induced by the droplet deformation. This signifies that vortex nucleation by droplet deformations is a very common process and that the exact shape of these vortices is determined by the finer details of the system. Finally, we mention that we have not seen any ring vortex nucleated in the helium free surface geometry for any of the cations of this study. Most likely, this is related to the very different surface distortions and density waves propagating through the free surface as compared to a droplet.

IV. SUMMARY

We have investigated by means of TDDFT the solvation dynamics of Rb^+ and Cs^+ formed at the surface of He_{1000} droplets. The solvation dynamics initially proceeds by the motion of the cation towards the droplet center due to the attractive interaction between the cation and the helium. Due to the large interaction strength, helium atoms in the surface region are quickly accelerated towards the ion forming a so-called snowball, i.e., a solidlike helium solvation structure. In the case of Rb^+ this process is complete after 10 ps. At longer times the snowball becomes solvated by the helium droplet which rearranges itself around the stationary ion. The large density fluctuations induced by the Rb^+ solvation process lead to the nucleation of quantized vortices. Depending on the details of the system, these can be either loop or ring vortices. In the case of Cs^+, the initial phase of the snowball formation prevents the ion from penetrating the helium droplet. The snowball therefore forms at the surface of the droplet in about 30 ps. Due to the effective shielding of the Cs^+ charge by its surrounding helium atom, it is only very weakly bound to the droplet. As a result, the Cs^+ snowball desorbs after 90 ps from the droplet due to helium density fluctuations.

The simulations reveal that the final outcome of the dynamics is strongly determined by the initial phase of the evolution. In the case of the alkalis investigated here, the snowball formation initiated by the strong interaction of the cation with helium hinders a direct solvation of the ion as was observed for Ba^+ which has a much weaker interaction with the helium [28]. The initial phase of the solvation process depends not only critically on the interaction strength between the ion and the helium, but also on the initial helium configuration. In particular, there is a clear droplet-size dependence especially apparent in the case of Cs, as simulations of Cs^+ on a flat helium surface have revealed. This reconciles the outcome of our calculations, carried out for a fairly small droplet, with the well established experimental fact that upon *in situ* ionization of the neutral species, Ba, Rb, and Cs cations remain attached to helium droplets made of several thousand atoms [29–32]. It should be noted, however, that in these experiments the alkalis have been ionized via an intermediate state.

Concluding, the solvation of surface located ions in helium droplets is not solely determined by the energy balance but depends strongly on the finer details of the system under study. As a result, the outcome can be very different for what appear to be very similar systems.

ACKNOWLEDGMENTS

We would like to thank Massimo Mella and Frank Stienkemeier for useful discussions. This work has been performed under Grant No. FIS2011-28617-C02-01 from DGI, Spain (FEDER), Grant No. 2014SGR401 from Generalitat de Catalunya, and Grant No. 200021-146598 from the Swiss National Science Foundation. A.L. has been supported by the ME (Spain) FPI program, Grant No. BES-2012-057439.

[1] B. Tabbert, H. Günter, and G. zu Putlitz, J. Low Temp. Phys. **109**, 653 (1997).

[2] M. Foerste, H. Guenther, O. Riediger, J. Wiebe, and G. zu Putliz, Z. Phys. B: Condens. Matter **104**, 317 (1997).

[3] M. Rossi, M. Verona, D. E. Galli, and L. Reatto, Phys. Rev. B **69**, 212510 (2004).
[4] S. L. Fiedler, D. Mateo, T. Aleksanyan, and J. Eloranta, Phys. Rev. B **86**, 144522 (2012).
[5] K. R. Atkins, Phys. Rev. **116**, 1339 (1959).
[6] M. Hartmann, R. E. Miller, J. P. Toennies, and A. Vilesov, Phys. Rev. Lett. **75**, 1566 (1995).
[7] D. M. Brink and S. Stringari, Z. Phys. D **15**, 257 (1990).
[8] P. Sindzingre, M. L. Klein, and D. M. Ceperley, Phys. Rev. Lett. **63**, 1601 (1989).
[9] M. V. Rama Krishna and K. B. Whaley, Phys. Rev. Lett. **64**, 1126 (1990).
[10] S. A. Chin and E. Krotscheck, Phys. Rev. B **45**, 852 (1992).
[11] E. Krotscheck and R. Zillich, J. Chem. Phys. **115**, 10161 (2001).
[12] S. Grebenev, J. P. Toennies, and A. Vilesov, Science **279**, 2083 (1998).
[13] N. B. Brauer, S. Smolarek, E. Loginov, D. Mateo, A. Hernando, M. Pi, M. Barranco, W. J. Buma, and M. Drabbels, Phys. Rev. Lett. **111**, 153002 (2013).
[14] D. Mateo, A. Hernando, M. Barranco, E. Loginov, M. Drabbels, and M. Pi, Phys. Chem. Chem. Phys. **15**, 18388 (2013).
[15] L. F. Gomez, E. Loginov, and A. F. Vilesov, Phys. Rev. Lett. **108**, 155302 (2012).
[16] D. Spence, E. Latimer, C. Feng, A. Boatwright, A. M. Ellis, and S. Yang, Phys. Chem. Chem. Phys. **16**, 6903 (2014).
[17] E. Latimer, D. Spence, C. Feng, A. Boatwright, A. M. Ellis, and S. Yang, Nano Lett. **14**, 2902 (2014).
[18] Ph. Thaler, A. Volk, F. Lackner, J. Steurer, D. Knez, W. Grogger, F. Hofer, and W. E. Ernst, Phys. Rev. B **90**, 155442 (2014).
[19] L. F. Gomez *et al.*, Science **345**, 906 (2014).
[20] J. P. Toennies and A. F. Vilesov, Angew. Chem., Int. Ed. **43**, 2622 (2004).
[21] F. Dalfovo, R. Mayol, M. Pi, and M. Barranco, Phys. Rev. Lett. **85**, 1028 (2000).
[22] K. K. Lehmann and R. Schmied, Phys. Rev. B **68**, 224520 (2003).
[23] F. Stienkemeier and K. K. Lehmann, J. Phys. B **39**, R127 (2006).
[24] M. Y. Choi, G. E. Douberly, T. M. Falconer, W. K. Lewis, C. M. Lindsay, J. M. Merritt, P. L. Stiles, and R. E. Miller, Int. Rev. Phys. Chem. **25**, 15 (2006).
[25] J. D. Close, F. Federmann, K. Hoffmann, and N. Quaas, J. Low Temp. Phys. **111**, 661 (1998).
[26] F. Ancilotto, M. Barranco, and M. Pi, Phys. Rev. Lett. **91**, 105302 (2003).
[27] A. Hernando, M. Barranco, R. Mayol, M. Pi, and M. Krosnicki, Phys. Rev. B **77**, 024513 (2008).
[28] D. Mateo, A. Leal, A. Hernando, M. Barranco, M. Pi, F. Cargnoni, M. Mella, X. Zhang, and M. Drabbels, J. Chem. Phys. **140**, 131101 (2014).
[29] M. Theisen, F. Lackner, and W. E. Ernst, Phys. Chem. Chem. Phys. **12**, 14861 (2010).
[30] E. Loginov and M. Drabbels, Phys. Rev. Lett. **106**, 083401 (2011).
[31] M. Theisen, F. Lackner, G. Krois, and W. E. Ernst, J. Phys. Chem. Lett. **2**, 2778 (2011).
[32] M. Theisen, F. Lackner, and W. E. Ernst, J. Chem. Phys. **135**, 074306 (2011).
[33] X. Zhang and M. Drabbels, J. Chem. Phys. **137**, 051102 (2012).
[34] S. Müller, M. Mudrich, and F. Stienkemeier, J. Chem. Phys. **131**, 044319 (2009).
[35] S. H. Patil, J. Chem. Phys. **94**, 8089 (1991).
[36] T. V. Tscherbul, P. Zhang, H. R. Sadeghpour, and A. Dalgarno, Phys. Rev. A **79**, 062707 (2009).
[37] G. Guillon, A. Viel, and J.-M. Launay, J. Chem. Phys. **136**, 174307 (2012).
[38] A. Ponti and F. Cargnoni (unpublished).
[39] A. D. Koutselos, E. A. Mason, and L. A. Viehland, J. Chem. Phys. **93**, 7125 (1990).
[40] H.-J. Werner *et al.*, *MOLPRO, version 2010.1, a package of ab initio programs*, see http://www.molpro.net.
[41] I. S. Lim, P. Schwerdtfeger, B. Metz, and H. Stoll, J. Chem. Phys. **122**, 104103 (2005).
[42] F. Weigend and R. Ahlrichs, Phys. Chem. Chem. Phys. **7**, 3297 (2005).
[43] D. E. Woon and T. H. Dunning, Jr., J. Chem. Phys. **100**, 2975 (1994).
[44] F.-M. Tao, Z. Li, and Y.-K. Pan, Chem. Phys. Lett. **255**, 179 (1996).
[45] S. F. Boys and S. Bernardi, Mol. Phys. **19**, 553 (1970).
[46] T. Leininger, A. Nicklass, W. Kuekhle, H. Stoll, M. Dolg, and A. Bergner, Chem. Phys. Lett. **255**, 274 (1996).
[47] F. Dalfovo, A. Lastri, L. Pricaupenko, S. Stringari, and J. Treiner, Phys. Rev. B **52**, 1193 (1995).
[48] M. Barranco, R. Guardiola, S. Hernández, R. Mayol, J. Navarro, and M. Pi, J. Low Temp. Phys. **142**, 1 (2006).
[49] L. Giacomazzi, F. Toigo, and F. Ancilotto, Phys. Rev. B **67**, 104501 (2003).
[50] L. Lehtovaara, T. Kiljunen, and J. Eloranta, J. Comput. Phys. **194**, 78 (2004).
[51] A. Hernando, M. Barranco, M. Pi, E. Loginov, M. Langlet, and M. Drabbels, Phys. Chem. Chem. Phys. **14**, 3996 (2012).
[52] F. O. Ellison, J. Am. Chem. Soc. **85**, 3540 (1963).
[53] F. Ancilotto, E. Cheng, M. W. Cole, and F. Toigo, Z. Phys. D **98**, 323 (1995).
[54] F. Ancilotto, M. Barranco, F. Caupin, R. Mayol, and M. Pi, Phys. Rev. B **72**, 214522 (2005).
[55] F. Ancilotto, M. Pi, R. Mayol, M. Barranco, and K. K. Lehmann, J. Phys. Chem. A **111**, 12695 (2007).
[56] O. Bünermann, G. Droppelmann, A. Hernando, R. Mayol, and F. Stienkemeier, J. Phys. Chem. A **111**, 12684 (2007).
[57] M. Frigo and S. G. Johnson, Proc. IEEE **93**, 216 (2005).
[58] A. Ralston and H. S. Wilf, *Mathematical Methods for Digital Computers* (Wiley, New York, 1960).
[59] F. Stienkemeier, J. Higgins, C. Callegari, S. I. Kanorsky, W. E. Ernst, and G. Scoles, Z. Phys. D **38**, 253 (1996).
[60] D. E. Galli, D. M. Ceperley, and L. Reatto, J. Phys. Chem. A **115**, 7300 (2011).
[61] S. Paolini, F. Ancilotto, and F. Toigo, J. Chem. Phys. **126**, 124317 (2007).
[62] E. Loginov and M. Drabbels, J. Chem. Phys. **136**, 154302 (2012).
[63] D. Mateo, A. Hernando, M. Barranco, R. Mayol, and M. Pi, Phys. Rev. B **83**, 174505 (2011).
[64] C. C. Lovallo and M. Klobukowski, J. Chem. Phys. **120**, 246 (2004).

[65] A. Kramida, Y. Ralchenko, J. Reader, and NIST ASD Team (2012), NIST Atomic Spectra Database (version 5.0), National Institute of Standards and Technology, Gaithersburg, MD, http://physics.nist.gov/asd.

[66] E. Loginov, D. Rossi, and M. Drabbels, Phys. Rev. Lett. **95**, 163401 (2005).

[67] F. Lackner, G. Krois, M. Theisen, M. Koch, and W. E. Ernst, Phys. Chem. Chem. Phys. **13**, 18781 (2011).

[68] F. Lackner, G. Krois, M. Koch, and W. E. Ernst, J. Phys. Chem. Lett. **3**, 1404 (2012).

[69] E. Loginov and M. Drabbels, J. Phys. Chem. A **118**, 2738 (2014).

[70] See Supplemental Material at http://link.aps.org/supplemental/10.1103/PhysRevB.90.224518 for the continuous movie corresponding to Figs. 6, 7, and 10.

[71] D. Mateo, D. Jin, M. Barranco, and M. Pi, J. Chem. Phys. **134**, 044507 (2011).

[72] J. Gspann, Surf. Sci. **106**, 219 (1981).

[73] C. M. Muirhead, W. F. Vinen, and R. J. Donnelly, Philos. Trans. R. Soc. London, Ser. A **311**, 433 (1984).

[74] R. J. Donnelly, *Quantized Vortices in Helium II*, Cambridge Studies in Low Temperature Physics Vol. 3 (Cambridge University Press, Cambridge, UK, 1991).

[75] G. H. Bauer, R. J. Donnelly, and W. F. Vinen, J. Low Temp. Phys. **98**, 47 (1995).

Chapter 4

Impurity capture

4.1 Capture of heliophobic atoms by ^{4}He nanodroplets: the case of cesium

Resumen (Spanish)

Abordamos el estudio de colisiones de impurezas de cesio —heliofóbicas— contra una nanogota de $^4He_{1000}$ aplicando la Teoría del Funcional de la Densidad para diferentes energías de colisión y parámetros de impacto.

Para colisiones frontales —parámetro de impacto igual a cero— hemos encontrado una variada fenomenología. Para la mayor energía utilizada, Cs a 200 m/s, la impureza traspasa completamente la nanogota de un extremo a otro tras depositar en ella una cierta cantidad de energía cinética. A medida que la energía cinética inicial de la impureza disminuye, se puede observar que primero la impureza rebota contra el helio —para velocidades en torno a 100 m/s— y finalmente es capturada por la gota —velocidad de impacto de unos 50 m/s—.

También hemos estudiado el caso de las colisiones periféricas, en las cuales se deposita tanto energía cinética como momento angular en la gota. Esto nos ha permitido observar el flujo irrotacional del helio en el interior de la gota y la nucleación de vórtices anulares a consecuencia de las grandes deformaciones superficiales que se producen en la nanogota. En este caso, para energías y parámetros de impacto pequeños se produce la captura de la impureza, que queda sobre la superficie de la gota orbitando al rededor del centro de masas de la misma.

La fenomenología que se desprende de los cálculos TDDFT es compatible con lo observado experimentalmente, solo que en un rango de energías menor.

PCCP

PAPER

View Article Online
View Journal | View Issue

Cite this: *Phys. Chem. Chem. Phys.*, 2014, **16**, 23206

Received 25th July 2014,
Accepted 9th September 2014

DOI: 10.1039/c4cp03297g

www.rsc.org/pccp

Capture of heliophobic atoms by ^{4}He nanodroplets: the case of cesium†

Antonio Leal,*[a] David Mateo,[b] Alberto Hernando,[c] Martí Pi[a] and Manuel Barranco[a]

Within Density Functional Theory (DFT), we address the capture of a Cs atom by a superfluid helium nanodroplet using models of different complexity. In the simplest model, the Cs-droplet potential is obtained in two extreme approximations, namely the sudden approximation in which one assumes that the density of the droplet is not relaxed as Cs approaches it, and the adiabatic approximation in which one assumes that it does. Next, a more complex approach in which the collision is described within a time-dependent DFT approach is employed. Depending on the energy and impact parameter of the impinging Cs atom, a rich variety of dynamical phenomena appears that is discussed in some detail.

I. Introduction

Liquid helium drops formed in free jet expansions of helium gas readily capture atoms and molecules in standard experimental conditions. It was unclear at the beginning whether this was possible or not, since early experiments were interpreted as if ^{4}He droplets were transparent to the dopants.[1] Experiments carried out later on demonstrated that this is not the case, as first shown for Ne atoms captured by ^{4}He drops.[2]

This ability of helium droplets has had a huge impact on the development of the physics and chemistry of helium droplets. Indeed, the isolation of atoms and molecules in ultracold helium droplets made of 10^3–10^8 atoms has allowed to carry out high resolution spectroscopic studies of the dopant and to study chemical reactions at very low temperatures of the order of 0.4 K. Most of the work done in this area has been reviewed in a series of papers, see *e.g.* ref. 3–11 and references therein.

While many studies on the spectroscopy of impurities attached to helium droplets have been carried out, only a few studies have addressed the capture of dopants by helium droplets. For the present purposes, let us just mention two joint experimental and theoretical works aiming at determining the density profiles of large ^{4}He and ^{3}He droplets from the scattering of Ar and Kr atoms off helium droplets,[12,13] and the microscopic approach to the scattering of ^{3}He and ^{4}He atoms from inhomogeneous quantum liquids of ref. 14, 15 and references therein.

Very recently, the simulation of dynamic processes involving atomic impurities in helium droplets has been undertaken within time-dependent Density Functional Theory (TDDFT). Thus far, TDDFT seems to be the only workable method for the description of real-time process in helium droplets whose size is large enough to allow for a sensible comparison with the current experiments. The method has been applied to the desorption of alkali atoms[16,17] and to the translational dynamics of atoms and cations in the bulk of the droplets.[18–20]

In this work we address the capture of simple atoms by superfluid ^{4}He droplets taking as a study case a heliophobic species, namely a Cs atom impinging on a droplet made of $N = 1000$ helium atoms. It is well known that alkali atoms do not solvate inside ^{4}He droplets but reside in barely bound dimple states at their surface.[21] Studies on Cs are particularly interesting since once captured it is known to stay on the droplet surface even upon photo-excitation.[22] We leave for a forthcoming study the case of a heliophilic species as Xe, for which experiments similar to these of ref. 12 and 13 can be carried out.[23]

We first use a rather simple model borrowed from nuclear physics that was employed in the past to describe heavy ion collisions. It allows to obtain the absorption cross section of the Cs atom using as main ingredients the Cs–He pair potential and the droplet density obtained within Density Functional Theory (DFT). Next, a full TDDFT calculation is carried out at several energies and impact parameters. Depending on these physical inputs, we have found that the Cs atom can get stuck to the droplet, orbit around it, bounce back or pass across the droplet. Interestingly, we have found that the capillary waves produced at the droplet surface during the collision process may act as nucleation seeds of quantized ring vortices. This mechanism, similar to that found in Bose–Einstein condensates

[a] *Departament ECM, Facultat de Física, and IN^{2}UB, Universitat de Barcelona, Diagonal 645, 08028 Barcelona, Spain. E-mail: aleal@ecm.ub.edu*
[b] *Department of Chemistry and Biochemistry, California State University at Northridge, 18111 Nordhoff Street, Northridge, California 91330, USA*
[c] *Laboratory of Theoretical Physical Chemistry, Institut des Sciences et Ingénierie Chimiques, Swiss Federal Institute of Technology Lausanne (EPFL), CH-1015 Lausanne, Switzerland*

† Electronic supplementary information (ESI) available. See DOI: 10.1039/c4cp03297g

View Article Online

Paper PCCP

in confined cold gases,[24] is different from the one by which fast-moving impurities in the superfluid[25] or in the bulk of helium droplets[20] nucleate vortices when the dopant velocity exceeds the Landau critical velocity.

This paper is organized as follows. In Section II we describe a simple method to calculate the absorption cross section and the results obtained in two extreme approximations. In Section III we briefly present the method we use to describe the Cs-droplet collision within the TDDFT approach as well as the results obtained with it. Finally, a summary is presented in Section IV.

II. A simple model for impurity sticking

Inspired in the nucleon–nucleus collision phenomenology, a liquid drop plus optical model was used in the past to address elastic, inelastic and absorptive scattering of ^{4}He atoms from ^{4}He droplets.[26] It is possible to obtain the cross section for the capture of a Cs atom by a helium droplet using a well-established phenomenological model also borrowed from nuclear physics.[27] The cross section for the capture is written as[28]

$$\sigma(E) = \frac{\pi}{\kappa^2}\sum_{\ell=0}^{\infty}(2\ell+1)T_\ell \qquad (1)$$

with

$$\kappa = \sqrt{\frac{2\mu E}{\hbar^2}}, \qquad (2)$$

where μ is the reduced mass of the system and E is the available energy in the center-of-mass framework. T_ℓ is the ℓ-th transmission coefficient leading to the capture of Cs in the ℓth-channel, where ℓ is the droplet-impurity relative angular momentum in $\hbar$ units in that channel.

For a large helium droplet *at rest*, since its mass is much larger than the Cs atom mass, it would be justified to identify the center-of-mass of the droplet + impurity framework, where collision theory is formulated,[29] with the laboratory framework, taking for μ the mass of Cs and for the center-of-mass of the system that of the helium droplet, identifying E with the kinetic energy of Cs in the laboratory and ℓ with the angular momentum of the impinging impurity with respect to the center-of-mass of the droplet. In actual experiments, neither the droplet nor the impurity are at rest. Rather, the impurity atoms in a secondary beam cross the droplet beam at some angle.[12,13] Unless explicitly stated, all the results presented in this work are discussed in the framework in which the helium droplet is at rest before the collision. In this frame, the center-of-mass sensibly coincides with that of the droplet, and the relative angular momentum with the angular momentum of the Cs atom with respect to the center-of-mass of the droplet. Expressing cross sections and other physical observables in one frame or another involves kinematic transformations that depend on the state of motion of the target (droplet) and projectile (Cs)[29] in a particular experiment but are not so relevant for the present purposes.

Provided that the reduced de Broglie wave length of cesium $\lambda\!\!\!^{-}_{\rm Cs} \equiv 1/\kappa \ll$ dimension of the droplet, the system behaves classically and T_ℓ abruptly goes from 0 to 1 in a ℓ-range small compared with the range of ℓ values leading to capture. We have checked that this is the case for a $N = 1000$ atoms droplet and a typical velocity of 100 m s^{-1}. We can thus take $T_\ell = 1$ up to a critical ℓ value $\ell_{\rm cr}$ (sharp cut-off approximation). Hence,

$$\sigma(E) = \frac{\pi}{\kappa^2}\sum_{\ell=0}^{\ell_{\rm cr}}(2\ell+1) = \frac{\pi}{\kappa^2}(\ell_{\rm cr}+1)^2 \qquad (3)$$

In order to determine $\ell_{\rm cr}$, we proceed as follows. Firstly, we obtain the Cs-droplet interaction potential as a function of the distance $\mathbf{R}$ between the center of mass of the droplet and the location of the Cs atom. We have two possibilities: either we relax the helium density $\rho(\mathbf{r})$ for given $\mathbf{R}$ (adiabatic approximation), of we keep $\rho(\mathbf{r})$ spherical (sudden approximation). In both cases, the total interaction potential is obtained by adding to $V(R)$ the centrifugal term, getting for a given ℓ value the effective potential

$$V_\ell(R) = V(R) + \frac{\ell(\ell+1)\hbar^2}{2\mu R^2} \qquad (4)$$

As $V(R)$ has an attractive part and $\ell(\ell+1)\hbar^2/2\mu R^2$ is repulsive and dominant at large distances, $V_\ell(R)$ has some structure. For the cases of interest here, it displays a local minimum ("pocket") followed by a local maximum, *i.e.*, there is a barrier hindering the capture unless the available energy (kinetic energy of Cs) is high enough to overcome it. If it is too large, processes as disintegration of the droplet or Cs passing across it may happen. We discard these possibilities.

After the barrier is overcome, it is assumed that dissipation comes very efficiently into play and the Cs atom is drawn to the minimum of the potential being trapped. For a given E, the largest ℓ leading to the capture of Cs defines $\ell_{\rm cr}$. For $V_{\ell_{\rm cr}}$ the pocket and the barrier collapse and their energy is equal to the impinging Cs energy E. Within this model, the existence of the pocket is instrumental for the capture.

A. Sudden approximation

In terms of the Cs–He pair potential V_X (ref. 30) and the spherically symmetric equilibrium density of the pure ^{4}He$_{1000}$ droplet obtained using the Orsay–Trento (OT) functional[31] we have

$$V(R) = \int d\mathbf{r}\rho(\mathbf{r})V_X(|\mathbf{r}-\mathbf{R}|). \qquad (5)$$

Fig. 1 shows the sudden potential V_ℓ for several ℓ values. Notice the appearance of the pocket and barrier structures up to $\ell = 300$. The figure shows that $\ell_{\rm cr} = 300$ for Cs approaching ^{4}He$_{1000}$ at $v_{\rm Cs} = 100$ m s^{-1} (corresponding to a kinetic energy of 80 K) and impact parameter $b_{\rm cr} = 14.5$ Å; we recall that the impact parameter b is defined as $\ell\hbar = m_{\rm Cs}v_{\rm Cs}b$ and hence $\ell_{\rm cr}\hbar = m_{\rm Cs}v_{\rm Cs}b_{\rm cr}$. The capture cross section is $\sigma = 665$ Å^2. The cross sections calculated in ref. 12 for Ar and Kr atoms are about three times larger and include the elastic contribution to it. If $\ell_{\rm cr} \gg 1$, eqn (3) and the above definition yield $\sigma = \pi b_{\rm cr}^2$. Since the sharp density radius of the droplet $R_0 = r_0N^{1/3}$ (with $r_0 = 2.22$ Å)

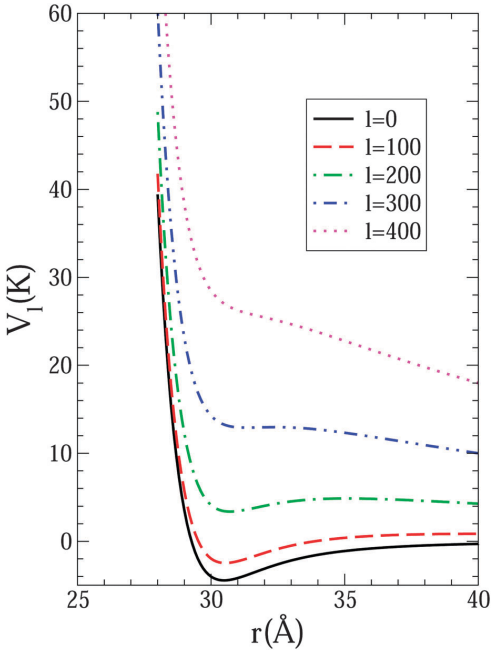

Fig. 1 Sudden potential $V_\ell(r)$ (K) as a function of r (Å) for several ℓ values.

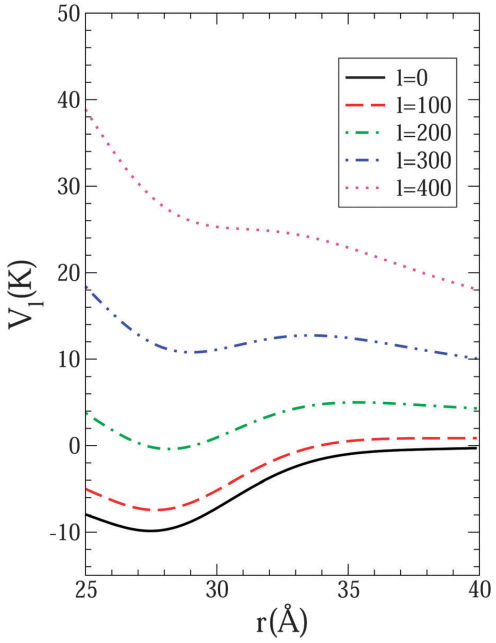

Fig. 2 Adiabatic potential $V_\ell(r)$ (K) as a function of r (Å) for several ℓ values.

is 22.2 Å for $N = 1000$, it appears that the sticking cross section is similar to the geometrical cross section.

B. Adiabatic approximation

In this case one has to minimize the energy of the Cs@^{4}He$_{1000}$ complex keeping the Cs atom a distance R apart from the center of mass of the droplet.[17] Then

$$V(R) = E[\mathrm{Cs@^4He_{1000}}(R)] - E[^4\mathrm{He_{1000}}], \qquad (6)$$

where E[Cs@^{4}He$_{1000}(R)$] is the energy of the Cs-droplet complex and $E[^4\mathrm{He}_{1000}]$ is the energy of the pure droplet, both calculated within DFT.

Fig. 2 shows the adiabatic potential V_ℓ for several ℓ values. The potential for $\ell = 0$ is consistent with that found in a similar calculation by Callegari and Ancilotto,[32] which displays a minimum of about 14 K at a distance of $\sim$33.5 Å (see Fig. 8 of this reference), but for a $N = 2000$ droplet. For this reason, the minimum of their potential is deeper and located at a larger distance.

We have found that $\ell_{cr} = 375$ for Cs approaching ^{4}He$_{1000}$ at 100 m s^{-1} and impact parameter $b_{cr} = 17.9$ Å. The capture cross section is $\sigma = 1012$ Å^2. As in the adiabatic approximation one relaxes the helium density, the critical angular momentum and cross sections are larger than in the sudden approximation since part of the available energy and angular momentum have been deposited into the droplet before the capture of the impurity. Notice that the value of b_{cr} is similar to the radius of the droplet. This means that if dissipation acts efficiently transferring the incoming energy into excited modes of the droplet and/or evaporation of helium atoms, the capture cross section is similar to the geometric cross section of the droplet.

III. Real-time dynamics within TDDFT

The dynamics is triggered by giving to the Cs atom some kinetic energy and angular momentum or, equivalently, some velocity v_{Cs} and impact parameter b (in the framework where the droplet is at rest before the collision). The Cs atom has been initially placed 32 Å away of the center-of-mass of the droplet. Within TDDFT, we represent the He droplet by a complex effective wave function $\Psi_{He}(\mathbf{r},t)$ such that $\rho(\mathbf{r},t) = |\Psi_{He}(\mathbf{r},t)|^2$. The Cs atom is treated classically as its mass is much larger than the He atom mass. Hence, its position $\mathbf{r}_{Cs}(t)$ obeys the Newton equation. We have[17]

$$\begin{aligned} i\hbar\frac{\partial}{\partial t}\Psi_{He} &= \left[-\frac{\hbar^2}{2m_{He}}\nabla^2 + \frac{\delta\mathcal{E}_{He}}{\delta\rho(\mathbf{r})} + V_X(|\mathbf{r}-\mathbf{r}_{Cs}|)\right]\Psi_{He} \\ m_{Cs}\ddot{\mathbf{r}}_{Cs} &= -\nabla_{\mathbf{r}_{Cs}}\left[\int d\mathbf{r}\rho(\mathbf{r})V_X(|\mathbf{r}-\mathbf{r}_{Cs}|)\right] \\ &= -\int d\mathbf{r}[\nabla\rho(\mathbf{r})]V_X(|\mathbf{r}-\mathbf{r}_{Cs}|), \end{aligned} \qquad (7)$$

where $\mathcal{E}_{He}$ is the OT potential energy density per unit volume. Eqn (7) have been discretized in cartesian coordinates using a spatial grid of 0.4 Å. The spatial derivatives have been calculated with 13-point formulas. Fast-Fourier techniques have been

View Article Online
Paper PCCP

employed to efficiently calculate the energy density and mean-field potential.[33] The dynamics has been followed using a predictor–corrector method[34] fed by a few time steps obtained by a fourth-order Runge–Kutta algorithm. A time step of 1 fs has been used. This time step can be compared with the period τ_λ of surface λ-mode oscillations of a spherical helium droplet of radius R_0, atom density ρ_0 and surface tension σ, whose energy within the liquid drop model are given by[35]

$$E_\lambda = \frac{h}{\tau_\lambda} = \sqrt{\frac{\hbar^2\gamma}{\rho_0 m_{\mathrm{He}} R_0{}^3}\lambda(\lambda-1)(\lambda+2)} \qquad (8)$$

Taking the values corresponding to ^{4}He ρ_0 = 0.0218 Å^{-3}, γ = 0.274 K Å^{-2} and $\hbar^2/m_{\mathrm{He}}$ = 12.12 K Å^2 one obtains for the quadruple mode of the N = 1000 droplet E_2 = 0.33 K and hence τ_2 = 1.45 ps. Thus, our time resolution is expected to cover the relevant aspects of the dynamics.

Even within TDDFT, the calculations are very time consuming. On the one hand, the mean field potentials in eqn (7) are cumbersome to obtain in the case of helium as compared to those entering the much simpler time-dependent Gross–Pitaevskii equation for cold gases.[24] On the other hand, the calculation box must be large enough to accommodate a large droplet. We have used a three dimensional grid made of 180 × 180 × 256 points. For these reasons, rather than presenting systematic results we have limited ourselves to the discussion of several cases relevant for the physics of impurity capture.

A. Head-on collisions

We have carried out simulations for Cs atoms impinging on the ^{4}He$_{1000}$ droplet at v_{Cs} = 50, 75, 100, and 200 m s^{-1} and impact parameter b = 0. As the ESI† shows,[36] the Cs atom is captured at 50 m s^{-1}, barely escapes the droplet at 75 m s^{-1}, bounces back at 100 m s^{-1}, and pierces through the droplet at 200 m s^{-1}. Notice that at a given velocity, peripheral $b \neq 0$ collisions cannot lead to Cs capture if the corresponding head-on collision does not, as energy is less efficiently dispersed into the droplet for the former than for the later.

The energy has to be very efficiently transferred into the droplet for the impurity to stick to its surface. The simulation at 100 m s^{-1} shown in Fig. 3, corresponding to a Cs kinetic energy E_{kin} = 80 K, is very illustrative of the difficulties inherent to the simulation of the capture process. The Cs atom bounces back at ~10 m s^{-1} (E_{kin} = 0.8 K), indicating that 99% of the available energy in the entrance channel has been transferred to excited modes of the droplet as ripplons, phonons, maxons, rotons, vortices, … (we have not detected any appreciable atom evaporation off the calculation cell). For Cs to be captured, the droplet has to dissipate that energy plus the binding energy of the impurity to the droplet. Using the OT functional, we have calculated this binding, $E[^4\mathrm{He}_{1000}] - E[\mathrm{Cs}@^4\mathrm{He}_{1000}]$ = 10.5 K. A value of 13.5 K was found by Ancilotto *et al.* for a planar helium surface using a different functional and Xe–He interaction.[37] A larger value should be expected for the planar geometry due to curvature effects, see. *e.g.* ref. 38.

The simulation at 75 m s^{-1} shown in Fig. 4 illustrates that dynamic effects may dramatically alter the potential well that binds the impurity to the droplet surface: a local deformation of the surface around the Cs atom "kicks it out" when the impurity seemed apparently stuck to the droplet. This limiting case defines the velocity at which Cs is captured, which is some 4–5 times smaller than typical thermal velocities in the pickup chamber. As the OT functional properly describes the elementary excitations of liquid helium,[39] one possible source for this disagreement is that the TDDFT approach does not yield enough atom evaporation at low energies. We want to mention however, that TDDFT may yield appreciable evaporation if the energy deposited is large.

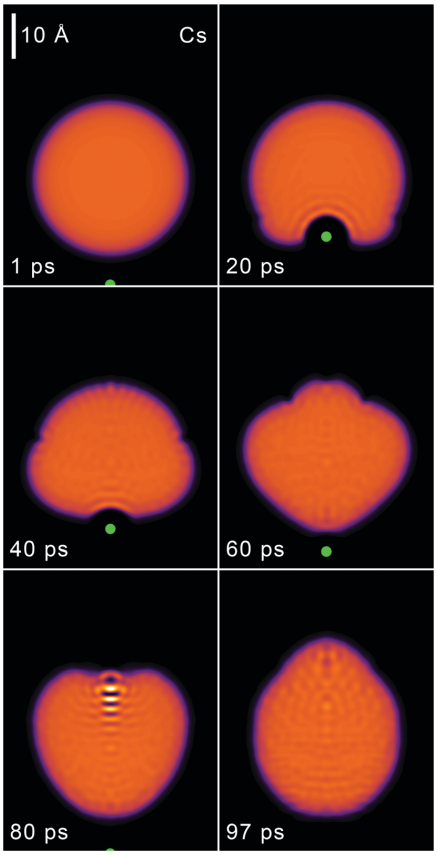

Fig. 3 Dynamic evolution of Cs (big dot) approaching from below the N = 1000 helium droplet at v_{Cs} = 100 m s^{-1} and b = 0, eventually bouncing back. The corresponding time is indicated in each frame.

The simulation at 200 m s^{-1} in Fig. 5 shows that Cs goes across the helium droplet without being captured. It also displays the appearance of a ring vortex nucleated at surface region of the droplet opposite to the collision point. Calculation of the circulation around the vortex core yields a value of unity in units of h/m_{He}, indicating that this ring vortex is quantized, and so are the others discussed in this work.

As it can be seen,[36] the vortex nucleates from the collapse of a surface perturbation created at the point of impact that has

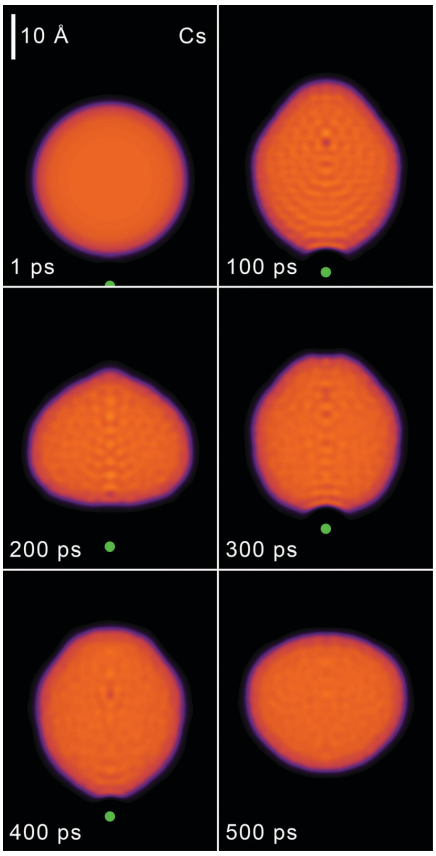

Fig. 4 Dynamic evolution of Cs (big dot) approaching from below the N = 1000 helium droplet at v_{Cs} = 75 m s^{-1} and b = 0, nearly captured by it. The corresponding time is indicated in each frame.

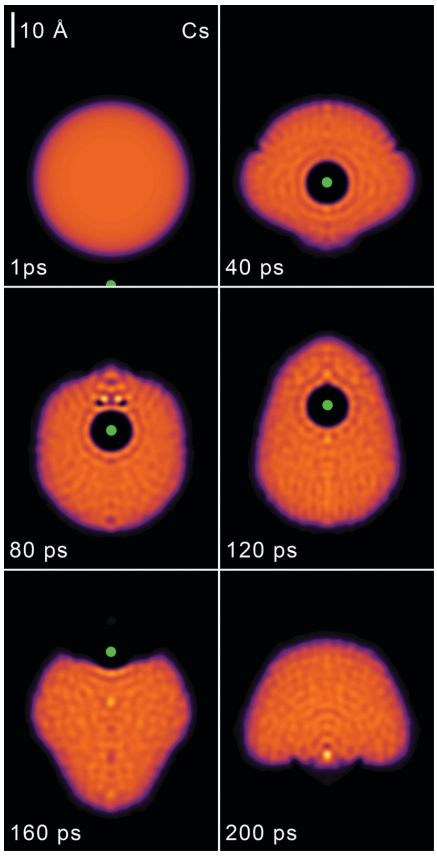

Fig. 5 Dynamic evolution of Cs (big dot) approaching from below the N = 1000 helium droplet at v_{Cs} = 200 m s^{-1} and b = 0, going across it. The corresponding time is indicated in each frame. The two dark spots in the t = 80 ps frame are the cross section of a ring vortex about to collide with the atomic bubble approaching it from below.

traveled from it as a "circular" tidal wave. The vortex energy E_{ring} can be estimated by the expression[25]

$$E_{ring} = \frac{2\pi^2\hbar^2}{m_{He}}\rho_0 R\left(\ln\frac{8R}{a} - 1.615\right), \quad (9)$$

with a the vortex core radius, R the ring radius and ρ_0 the helium number density at large distance. Taking the values for the present system, a = 1.0 Å, R = 3.9 Å and ρ_0 = 0.0218 Å^{-3} corresponding to the number density of a pure helium droplet, we obtain an energy of ~17.7 K. We want to indicate that the values of some variables discussed in this section have been obtained from an analysis as accurate as possible of the ESI† that is in a graphic format. For this reason, they cannot be but estimates.

After nucleating at the droplet surface, the ring vortex penetrates into the droplet with a self-induced velocity[25]

$$v_{ring} = \frac{\hbar}{2m_{He}R}\left(\ln\frac{8R}{a} - 0.615\right). \quad (10)$$

Using the previous values, we find v_{ring} ~ 37.6 m s^{-1}. One should have in mind that eqn (9) and (10) are only valid in the limit of $R \gg a$. Fig. 6 displays the ring vortex approaching the Cs bubble a few picosecond before they collide and the vortex is annihilated. Superimposed on the helium density displayed in this figure are the circulation lines. These clearly reveal a circular flow field around the vortex.

The Cs atom eventually detaches from the droplet with a velocity v_{Cs} ~ 64.7 m s^{-1}, having thus deposited into the droplet about a 90% of the energy available in the entrance channel (320 K). Notice that the angular momentum involved in the process is zero; we recall that, at variance with a linear vortex or a vortex loop,[25] a ring vortex carries no net angular momentum.

A ring vortex is also nucleated in the Cs-droplet collision at 100 m s^{-1}. In this case, it is immediately washed out by the incoming density waves.[36] For smaller velocities (50 m s^{-1} and 75 m s^{-1}), the velocity of the impurity in the droplet does not

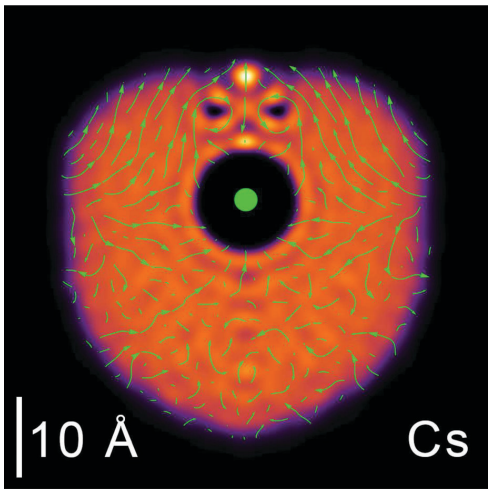

Fig. 6 Helium density at t = 75 ps showing a ring vortex approaching the Cs bubble from above. The circulation lines are represented in green. The situation corresponds to the head-on collision at v_{Cs} = 200 m s^{-1}.

exceed the Landau critical velocity and vortices are not nucleated. We notice that the simulation at 50 m s^{-1} shows the capture of the Cs atom by the droplet.[36]

B. Peripheral collisions and angular momentum deposition

We have carried out a simulation at v_{Cs} = 100 m s^{-1} with an impact parameter b = 11 Å, *i.e.*, about half the value of the sharp density radius of the droplet.[36] In this case, some angular momentum is also deposited into the droplet. After the collision, the Cs atom emerges at $v_{Cs} \sim$ 15.3 m s^{-1}, having transferred to the droplet a 98% of the available energy. The angular momentum in the entrance channel is $L = m_{Cs}v_{Cs}b = 230\hbar$. Part of it is taken away by the outgoing Cs atom ($\sim 114\hbar$); the angular momentum deposited into excited modes of the droplet is $\sim 105\hbar$, and the remaining $11\hbar$ are taken by the droplet as a whole in the recoil of its center-of-mass, some 6.6 Å during the 225 ps we have followed this collision (average velocity $\sim$3 m s^{-1}).

How angular momentum can be deposited into a helium droplet that cannot be set into rotation because it is superfluid and its velocity field is irrotational is an interesting issue.[24,40,41] One possibility is by nucleating vortex lines that start and end at the droplet surface.[42–44] In particular, a linear vortex along the diameter of a droplet with N atoms carries $N\hbar$ angular momentum. If there are no vortices in the droplet, the superfluid droplet may store angular momentum into surface waves, while the flow inside the droplet is still irrotational.

Fig. 7 and the ESI† corresponding to the v_{Cs} = 50 m s^{-1}, b = 11 Å collision seem to display a dimple at the droplet surface that "rigidly" rotates as the droplet does, dragging along the Cs atom. This is quite not so: the dimple travels on the droplet surface along with the impurity, without this meaning that the bulk of the droplet rotates, which is prevented by the irrotational character of the superfluid flow. We have calculated the flow

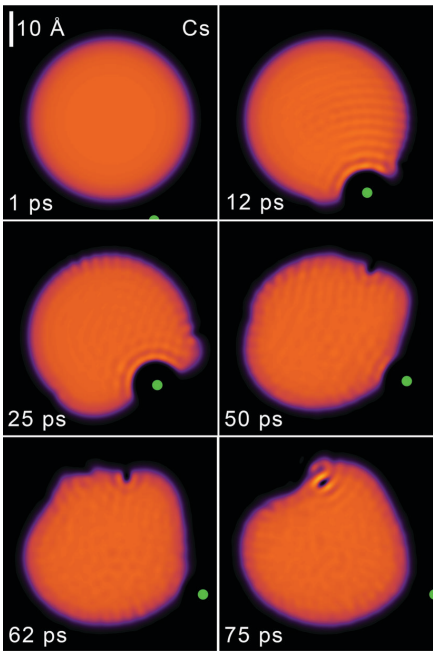

Fig. 7 Dynamic evolution of Cs (big dot) approaching from below the N = 1000 helium droplet at v_{Cs} = 100 m s^{-1} and b = 11 Å. The corresponding time is indicated in each frame.

pattern at t = 385 ps and show it in Fig. 8. It can be seen that the flow pattern in the laboratory fixed framework corresponds to an irrotational fluid instead of a rigid rotation. Hence, while the superfluid helium droplet may appear to an observer in the

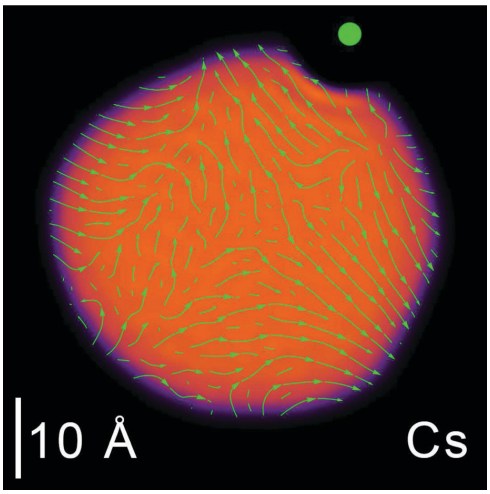

Fig. 8 Particle flow pattern at t = 385 ps corresponding to the v_{Cs} = 50 m s^{-1} and b = 11 Å collision. The big dot represents the Cs atom.

View Article Online
PCCP Paper

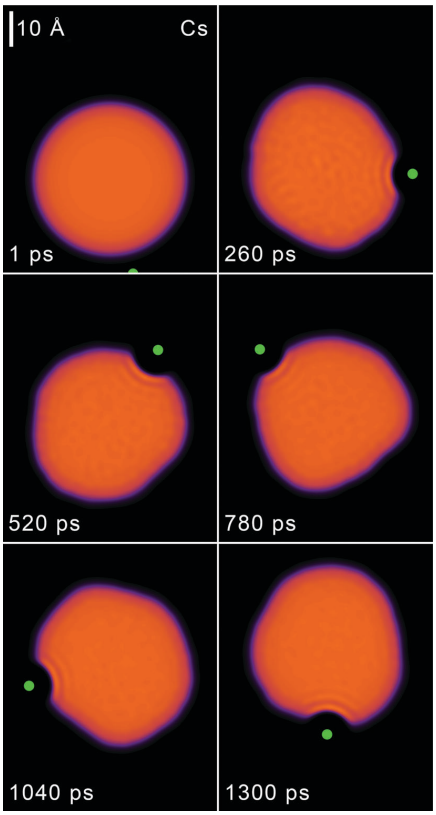

Fig. 9 Dynamic evolution of Cs (big dot) approaching from below the $N = 1000$ helium droplet at $v_{Cs} = 50$ m s^{-1} and $b = 9$ Å. The corresponding time is indicated in each frame.

laboratory as a deformed droplet rigidly rotating, Fig. 8 clearly shows that it does not. Similar patterns can be found *e.g.* in ref. 40 and 41. The angular momentum available in the collision is thus deposited into capillary waves traveling on the droplet surface, partly is taken away by promptly emitted helium atoms, and some remains in the impurity.

Decreasing the impact parameter to $b = 9$ Å, the Cs atom orbits around the core of the droplet.[36] This is one of the possibilities for the scattering of a particle by an attractive potential. Fig. 9 displays the collision at $v_{Cs} = 50$ m s^{-1} and impact parameter $b = 9$ Å. Notice that in this case the dynamics has been followed for more than 1.3 ns. The results at 50 m s^{-1} indicate that the critical impact parameter at this energy is $b_{cr} \sim 10$ Å and hence $\ell_{cr} = 94$. Eqn (3) yields a cross section of 260 Å^2 for the capture of Cs by this droplet at 50 m s^{-1}.

IV. Summary and outlook

We have studied the collision of a heliophobic Cs impurity with a ^{4}He$_{1000}$ droplet within TDDFT, obtaining a rich phenomenology depending on the impinging energy and impact parameter of the Cs atom.

For a head-on collision at the higher energy here addressed (Cs at 200 m s^{-1}) the droplet turns out to be "transparent" to the impurity in the sense that it goes across the droplet after having deposited into it a large part of its kinetic energy. Experimental evidence for the transmission of ^{3}He atoms through superfluid ^{4}He droplets was presented in ref. 45, although other possibilities to interpret the experiment were discussed in the same reference. As the kinetic energy decreases one observes that the impurity is first reflected (impinging velocities of 100 m s^{-1} and 75 m s^{-1}) and eventually it is captured by the droplet (impinging velocity of 50 m s^{-1}).

We have also addressed peripheral collisions, in which case not only energy but also angular momentum is deposited into the droplet. This has allowed us to visualize the irrotational flow of the superfluid helium inside the droplet and the nucleation of ring vortices from the large deformations produced at the droplet surface that also appear in head-on collisions. At low energies and small impact parameters the impurity is captured by the droplet, sometimes leading to its orbiting around the center-of-mass of the droplet.

It should be noted that while the theoretical phenomenology is consistent with the experimental findings, it appears at lower energies. Current experiments on Cs atoms involve velocities in the pickup chamber of the order of 400 m s^{-1}, for which our simulations yield droplet transparency. This discrepancy might hint that doping droplets with heliophobic dopants require of multiple collisions with droplets in the beam before they lose enough energy to be captured by one of them. This could be discerned by studying how the signal coming from single dopants attached to droplets scales with dopant density. It might also be a consequence of using in the simulations a mean field approach as TDDFT that, while it incorporates helium atom ejection as a possible energy dissipation mechanism,[20] it likely underestimates it, hindering the sticking of the weakly interacting heliophobic impurity. We recall that, according to our analysis of the Cs-droplet head-on collision at 100 m s^{-1}, the prompt emission of just two helium atoms would take away enough energy allowing for Cs to stick to the droplet surface. The interested reader might also look at ref. 46 for a comparison between the TDDFT and classical Molecular Dynamics methods applied to the collision of a pure ^{4}He$_{300}$ droplet at 200 m s^{-1} with a TiO_2 surface. It can be seen that within TDDFT, the droplet collision yields the ejection of helium atoms ("evaporation") and the spreading of most of the original droplet on the TiO_2 surface, that is wet by helium as most materials at temperatures low enough – the calculation was performed at zero temperature. The classical Molecular Dynamics approach yields the opposite behavior, with the splashing of the droplet out of the surface upon impact.

Ascertaining how well the present formalism works for a simple heliophilic impurity as xenon would help seize the limitations of the TDDFT simulations in this respect before undertaking any substantial improvement of the approach that might incorporate in a workable way efficient helium atom evaporation. We plan to address this issue in a forthcoming paper.

Acknowledgements

We would like to thank Frank Stienkemeier and Marcel Mudrich for useful discussions. This work has been performed under Grants No. FIS2011-28617-C02-01 from DGI, Spain (FEDER) and 2009SGR1289 from Generalitat de Catalunya. AL has been supported by the ME (Spain) FPI program, Grant No. BES-2012-057439.

References

1 J. Gspann, *Physica B+C*, 1981, **108**, 1309.
2 A. Scheidemann, J. P. Toennies and J. A. Northby, *Phys. Rev. Lett.*, 1990, **64**, 1899.
3 J. P. Toennies and A. F. Vilesov, *Angew. Chem., Int. Ed.*, 2004, **43**, 2622.
4 M. Barranco, R. Guardiola, S. Hernández, R. Mayol, J. Navarro and M. Pi, *J. Low Temp. Phys.*, 2006, **142**, 1.
5 K. Szalewicz, *Int. Rev. Phys. Chem.*, 2006, **27**, 273.
6 F. Stienkemeier and K. K. Lehmann, *J. Phys. B: At., Mol. Opt. Phys.*, 2006, **39**, R127.
7 M. Y. Choi, G. E. Douberly, T. M. Falconer, W. K. Lewis, C. M. Lindsay, J. M. Merritt, P. L. Stiles and R. E. Miller, *Int. Rev. Phys. Chem.*, 2006, **25**, 15.
8 J. Tiggesbäumker and F. Stienkemeier, *Phys. Chem. Chem. Phys.*, 2007, **9**, 4748.
9 A. Slenczka and J. P. Toennies, in *Low Temperatures and Cold Molecules*, ed. W. M. Smith, World Sci., Singapore, 2008, p. 345.
10 C. Callegari and W. E. Ernst, *Handbook of High Resolution Spectroscopy*, Wiley, New York, 2011, vol. 3, p. 1551.
11 M. Mudrich and F. Stienkemeier, arXiv:1406.4697v1 [physics-atm-clus] 18 Jun 2014, to be published in the Int. Rev. Phys. Chem.
12 J. Harms, J. P. Toennies and F. Dalfovo, *Phys. Rev. B: Condens. Matter Mater. Phys.*, 1998, **58**, 3341.
13 J. Harms, J. P. Toennies, M. Barranco and M. Pi, *Phys. Rev. B: Condens. Matter Mater. Phys.*, 2001, **63**, 184513.
14 E. Krotscheck and R. E. Zillich, *Eur. Phys. J. D*, 2007, **43**, 113.
15 E. Krotscheck and R. E. Zillich, *Phys. Rev. B: Condens. Matter Mater. Phys.*, 2008, **77**, 094507.
16 A. Hernando, M. Barranco, M. Pi, E. Loginov, M. Langlet and M. Drabbels, *Phys. Chem. Chem. Phys.*, 2012, **14**, 3996.
17 J. von Vangerow, A. Sieg, O. John, A. Leal, D. Mateo, M. Barranco, A. Hernando, M. Pi, F. Stienkemeier and M. Mudrich, *J. Phys. Chem. A*, 2014, **118**, 6604–6614.
18 D. Mateo, A. Hernando, M. Barranco, E. Loginov, M. Drabbels and M. Pi, *Phys. Chem. Chem. Phys.*, 2013, **15**, 18388.
19 N. B. Brauer, S. Smolarek, E. Loginov, D. Mateo, A. Hernando, M. Pi, M. Barranco, W. J. Buma and M. Drabbels, *Phys. Rev. Lett.*, 2013, **111**, 153002.
20 D. Mateo, A. Leal, A. Hernando, M. Barranco, M. Pi, F. Cargnoni, M. Mella, X. Zhang and M. Drabbels, *J. Chem. Phys.*, 2014, **140**, 131101.
21 O. Bünermann, G. Droppelmann, A. Hernando, R. Mayol and F. Stienkemeier, *J. Phys. Chem. A*, 2007, **111**, 12684.
22 M. Theisen, F. Lackner and W. E. Ernst, *J. Chem. Phys.*, 2011, **135**, 074306.
23 M. Lewerenz, B. Schilling and J. P. Toennies, *J. Chem. Phys.*, 1995, **102**, 8191.
24 L. Pitaevskii and S. Stringari, *Bose-Einstein Condensation*, International Series of Monographs on Physics, Clarendon Press, Oxford, 2003, vol. 116.
25 R. J. Donnelly, *Quantized vortices in helium II*, Cambridge Studies in low Temp. Phys., 1991, vol. 3.
26 D. Eichenauer, A. Scheidemann and J. P. Toennies, *Z. Phys. D: At., Mol. Clusters*, 1988, **8**, 295.
27 C. Ngô, *Prog. Part. Nucl. Phys.*, 1986, **16**, 139.
28 S. Gasiorowicz, *Quantum Physics*, John Wiley & Sons, New York, 3rd edn, 2003.
29 C. J. Joachain, *Quantum Collision Theory*, North-Holland, Amsterdam, 1975.
30 S. H. Patil, *J. Chem. Phys.*, 1991, **94**, 8089.
31 F. Dalfovo, A. Lastri, L. Pricaupenko, S. Stringari and J. Treiner, *Phys. Rev. B: Condens. Matter Mater. Phys.*, 1995, **52**, 1193.
32 C. Callegari and F. Ancilotto, *J. Phys. Chem. A*, 2011, **115**, 6789.
33 M. Frigo and S. G. Johnson, *Proc. IEEE*, 2005, **93**, 216.
34 A. Ralston and H. S. Wilf, *Mathematical methods for digital computers*, John Wiley and Sons, New York, 1960.
35 M. Casas and S. Stringari, *J. Low Temp. Phys.*, 1990, **79**, 135.
36 See the ESI† for the continuous movies corresponding to the collisions.
37 F. Ancilotto, E. Cheng, M. W. Cole and F. Toigo, *Z. Phys. B: Condens. Matter*, 1995, **98**, 323.
38 F. Stienkemeier, O. Bünermann, R. Mayol, F. Ancilotto, M. Barranco and M. Pi, *Phys. Rev. B: Condens. Matter Mater. Phys.*, 2004, **70**, 214509.
39 We have neglected the backflow term in the OT functional because it is ill-behaved at low densities.[31] As a consequence, the Landau velocity is overestimated meaning that rotons may be excited in the superfluid but when impurities move at higher velocities.[18]
40 A. Bohr and B. R. Mottelson, *Nuclear Structure*, W.A. Benjamin, Reading, MA, USA, 1975, vol. II, Appendix 6A.
41 G. M. Seidel and H. J. Maris, *Physica B*, 1994, **194–196**, 577.
42 G. H. Bauer, R. J. Donnelly and W. F. Vinen, *J. Low Temp. Phys.*, 1995, **98**, 47.
43 F. Dalfovo, R. Mayol, M. Pi and M. Barranco, *Phys. Rev. Lett.*, 2000, **85**, 1028.
44 K. K. Lehmann and R. Schmied, *Phys. Rev. B: Condens. Matter Mater. Phys.*, 2003, **68**, 224520.
45 J. Harms and J. P. Toennies, *Phys. Rev. Lett.*, 1999, **83**, 344.
46 N. F. Aguirre, D. Mateo, A. O. Mitrushchenkov, M. Pi and M. P. de Lara-Castells, *J. Chem. Phys.*, 2012, **136**, 124703.

Chapter 5

Summary and conclusions

This thesis consists of five papers published in peer-reviewed scientific journals between 2014 and 2016, all of them comprised in the field of low temperature physics and quantum fluids. These works represent a clear step forward in the description of doped helium droplets, as the processes there addressed either had not been addressed before, or had been addressed by methods far less sophisticated than density functional theory.

The first two papers, described in Chapter 2, are about dynamic studies of Ba impurities in $^4He_{1000}$ nanodroplets. It is experimentally known that all alkali atoms (and all alkaline-earth atoms heavier than magnesium) captured by ^{4}He droplets have an equilibrium state in a dimple on the surface of the droplet.

In the first paper (Section 2.1) we have studied the dynamics triggered by ionization of Ba atom at its equilibrium configuration. The spectroscopic studies carried by Prof. Drabbels have shown that this impurity sinks into the droplet upon ionization, as the Ba^+ absorption spectrum at helium nanodroplets coincides with that of the cation in bulk liquid helium. Our DFT studies reproduce these results, as they show how the impurity moves towards the bulk portion of the droplet after being ionized. During this sinking process, a rich variety of phenomena can be observed, *e.g.*, the dynamic formation of a high density solid-like structure surrounding the impurity (known as "snowball") or the nucleation of quantized ring vortices, for which we have estimated their energy and velocity.

The second paper focused on Ba^+ (Section 2.2) continues to study of the same system. In this case the motion of the cation in its ground state is followed inside the droplet for some time, after which Ba^+ is excited to the *6p* manifold. For this

system, the experiments describe an efficient ejection of the likely excited (but not experimentally ascertained) cation out of the droplet, either as a bare Ba^+ cation or in the form of Rb^+-He_n exciplexes mainly with $n = 1, 2$. However, our simulations do not show such desolvation; the cation remains inside of the He droplet in all the cases we have considered after exciting it to the *6p* manifold. Since for Ba^+ the *5d* manifold lies below the *6p*, we have also (unsuccessfully) explored the possible ejection of the cation after deexciting it from the $6p$ state, not only to the ground state but to the $5d$ states as well.

Chapter 3 is composed of two papers focused on heavy alkali atoms (Rb and Cs) dynamics at ^{4}He nanodroplets, which share the initial geometry with barium such that their ground state equilibrium position is in a dimple on the droplet surface.

The first paper (Section 3.1) studies the ejection of alkali atoms from the droplet surface upon excitation to the $6s$ (Rb) and $7s$ (Cs) states. The calculated relationship between the kinetic energy of the excited impurity and the photoexcitation energy that triggers the ejection fully agrees with the experimental one. By analyzing these systems we have found local density deformations as well as different kinds of density waves that propagate inside the droplet at supersonic velocities.

The second paper of this block (Section 3.2) presents a study on Rb^+ and Cs^+ impurities similar to that made for Ba^+ in Section 2.1, analyzing the dynamical evolution of the impurities upon ionization of the neutral species at their equilibrium state. Because the Rb^+-He and Cs^+-He interaction potentials are considerably attractive, we expect the sinking of the impurities inside the droplets, although it does not happen in all cases. For the $^4He_{1000}$ droplet we have observed that Rb^+ remains on the surface for a while and eventually sinks, nucleating vortex loops due to the appearance of density distortions at droplet surface, while Cs^+ escapes from that droplet taking away with it about 70 helium atoms forming a charged minicluster. We have checked that this different behavior is a finite size effect. Indeed, for bigger helium droplets ($^4He_{2000}$) and for the liquid helium free surface we have found for both alkalis a sinking behavior similar to that of Ba^+.

Lastly, Chapter 4 contains one single paper about the capture of heliophobic

impurities by helium nanodroplets. We have studied this topic making cesium impurities collide with the droplet at several impinging velocities and impact parameters, including head-on collisions corresponding to zero impact parameter. By changing the velocity we have observed several phenomena, from the capture of the impurity at the nanodroplet surface at small velocities, to the droplet "transparency" at high velocities (at 200 m/s the impurity pierces the drop from end to end). For collisions with impact parameter different from zero, which deposit a certain amount of angular momentum into the droplets, the study of the superfluid flow shows that the droplet does not rotate like a rigid body, as expected for a superfluid.

5.1 Outlook

While the studies presented in this thesis are a step forward towards a deeper understanding of the dynamic processes involving simple atomic and ionic impurities in ^{4}He nanodroplets, they leave however many questions in the air and a lot of work to be done to improve our understanding of these systems. Let us mention some that are currently underway:

- In spite of our rather detailed analysis, the dynamics of Ba^+ cations in helium nanodroplets leaves unanswered the question why theory and experiment are not in agreement. Is it due to an incomplete interpretation of the experimental data? Is it perhaps because the method employed to compute the interaction potentials does not take into account some important, undisclosed contribution? A deeper study of these points and considering other possible desorption mechanisms as the existence of non-radiative transitions might help answer this question.

- In the case of Rb and Cs impurities, the group of Prof. Dr. F. Stienkemeier (University of Freiburg) is currently carrying pump-probe experiments in which the excited alkali is subsequently ionized. Depending on the time delay between both processes, the cation may go away or bounce back to the helium droplet. TDDFT is especially suited to address this problem.

- For the capture process of the dopant, we have focused on an heliophobic impurity like cesium. What would happen when the impurity is heliophilic?

How the presence of vortices may affect the capture? This is especially relevant, as a recent experiment on vortex arrays in large helium droplets uses very heliophilic xenon atoms as dopants to obtain x-ray diffraction images in order to visualize the vortex array [18].

Appendix A

List of publications

2013

- *The structure of mixed ^{3}He-^{4}He droplets doped with OCS: A density functional approach.*
  A. Leal, D. Mateo, M. Pi, M. Barranco and J. Navarro. J. Chem. Phys. **139**, 174308 (2013)

2014

- *Communication: Nucleation of quantized vortex rings in ^{4}He nanodroplets.*
  D. Mateo, A. Leal, A. Hernando, M. Barranco, M. Pi, F. Cargnoni, M. Mella, X. Zhang and M. Drabbels. J. Chem. Phys. **140**, 131101 (2014)

- *Desorption dynamics of heavy alkali metal atoms (Rb, Cs) off the surface of helium nanodroplets.*
  J. von Vangerow, A. Sieg, F. Stienkemeier, M. Mudrich, A. Leal, D. Mateo, A. Hernando, M. Barranco and M. Pi. J. Phys. Chem. A **118**, 6604 (2014)

- *Capture of heliophobic atoms by ^{4}He nanodroplets: the case of cesium.*
  A. Leal, D. Mateo, A. Hernando, M. Pi and M. Barranco. Phys. Chem. Chem. Phys. **16**, 23206 (2014)

- *Picosecond solvation dynamics of alkali cations in superfluid ^{4}He nanodroplets.*
  A. Leal, D. Mateo, A. Hernando, M. Pi, M. Barranco, A. Ponti, F. Cargnoni, M. Drabbels. Phys. Rev. B **90**, 224518 (2014)

2016

- *Dynamics of photoexcited Ba^+ cations in ^4He nanodroplets.*
  A. Leal, X. Zhang, M. Barranco, F. Cargnoni, A. Hernando, D. Mateo, M. Mella, M. Drabbels and M. Pi. J. Chem. Phys. **144**, 094302 (2016)

Bibliography

[1] F. Stienkemeier, F. Meier and H. O. Lutz, *Spectroscopy of barium attached to superfluid helium clusters*. Eur. Phys. J. D **9**, 313 (1999)

[2] E. Loginov and M. Drabbels, *Spectroscopy and dynamics of barium-doped helium nanodroplets*. J. Chem. Phys. **136**, 154302 (2012)

[3] P. Kapitsa, *Viscosity of Liquid Helium below the λ-Point*. Nature **141**, 74 (1938)

[4] J. F. Allen and A. D. Misener, *Flow Phenomena in Liquid Helium II*. Nature **142**, 643-644 (1938)

[5] J. P. Toennies and A. F Vilesov, *Superfluid Helium Droplets: A Uniquely Cold Nanomatrix for Molecules and Molecular Complexes*. Angewandte Chemie International Edition **43**, 2622-2648 (2004)

[6] F. Stienkemeier and K. Lehmann, *Spectroscopy and dynamics in helium nanodroplets*. Journal of Physics B: Atomic, Molecular and Optical Physics **39**, R127 (2006)

[7] M. Barranco, R. Guardiola, S. Hernández, R. Mayol and J. Navarro, *Helium Nanodroplets: An Overview*. Journal of Low Temperature Physics **142**, 1-81 (2006)

[8] J. Tiggesbaumker and F. Stienkemeier, *Formation and properties of metal clusters isolated in helium droplets*. Phys. Chem. Chem. Phys., **9**, 4748-4770 (2007)

[9] M. Y. Choi, G. E. Douberly, T. M. Falconer, W. K. Lewis, C. M. Lindsay, J. M. Merritt, P. L. Stiles and R. E. Miller, *Infrared spectroscopy of helium nanodroplets: novel methods for physics and chemistry*. International Reviews in Physical Chemistry **25**, 15-75 (2006)

[10] K. Szalewicz, *Interplay between theory and experiment in investigations of molecules embedded in superfluid helium nanodroplets*. International Reviews in Physical Chemistry **27**, 273-316 (2008)

[11] C. Callegari and W. E. Ernst, *Helium Droplets as Nanocryostats for Molecular Spectroscopy — from the Vacuum Ultraviolet to the Microwave Regime*. Handbook of High-resolution Spectroscopy, 1551-1594 (2011)

[12] P. Hohenberg and W. Kohn, *Inhomogeneous Electron Gas*. Phys. Rev **136**, B864-B871 (1964)

[13] W. Kohn and L. J. Sham, *Self-Consistent Equations Including Exchange and Correlation Effects*. Phys. Rev. **140**, A1133 (1965)

[14] F. Dalfovo, A. Lastri, L. Pricaupenko, S. Stringari, J. Treiner, *Structural and Dynamical Properties of Superfluid-Helium - A Density-Functional Approach*. Phys. Rev. B **52**, 1193-1209 (1995)

[15] F. Ancilotto, M. Barranco, F. Caupin, R. Mayol and M. Pi, *Freezing of He-4 and its liquid-solid interface from density functional theory*. Phys. Rev. B **72**, 214522 (2005)

[16] D. Mateo, A. Hernando, M. Barranco, E. Loginov, M. Drabbels and M. Pi, *Translational dynamics of photoexcited atoms in He-4 nanodroplets: the case of silver*. Phys. Chem. Chem. Phys. **42**, 18388-18400 (2013)

[17] X. Zhang and M. Drabbels, *Communication: Barium ions and helium nanodroplets: Solvation and desolvation*. J. Chem. Phys. **137**, 051102 (2012)

[18] L. F. Gómez, A. F. Vilesov et al., *Shapes and vorticities of superfluid helium nanodroplets*. Science **345**, Issue 6199, pp. 906-909 (2014)